Crossed-Beam Laser Spectroscopy of Atomic Ruthenium

by

Richard Alexander Powis

A thesis submitted to
The University of Birmingham
for the degree of
DOCTOR OF PHILOSOPHY

School of Physics and Astronomy
The University of Birmingham
February 7, 2013

Abstract

High resolution crossed-beam laser spectroscopy has been used to measure the isotope shifts and hyperfine parameters of nineteen transitions in atomic ruthenium. These results have been used in conjunction with four other existing transition measurements to determine accurate values for the change in mean-square charge radius between the isotopes of ruthenium. The new charge radii measurements exhibit up to an order of magnitude improvement in accuracy compared to the previously published results. These accurate charge radii systematics in ruthenium provide additional data for the interesting $N = 60$ region of the nuclear chart. The transitions measured have been assessed in terms of their suitability for use in future collinear laser spectroscopy measurements of radioactive ruthenium isotopes. One transition in particular, the 349.8942nm $0 \longrightarrow 28571.890\text{cm}^{-1}$ transition, has the potential to be highly efficient.

Acknowledgments

The last four years working upon this thesis have been one of the most interesting and enjoyable periods of my life. I have thoroughly enjoyed living and working around Birmingham and the University and that is largely due to a small group of people who I would now like to acknowledge.

Firstly I would like to thank my supervisor Garry Tungate for all of his help, support and guidance over the last four years. The fact that you were always available for consultation and always optimistic during the times when data was hard to come by was greatly appreciated. I also owe considerable thanks to Dave Forest for sharing his incredible knowledge of the laser and data analysis programs and being always willing to help. Also important were our many morale-boosting trips to the pub.

I must also thank Barry Jackson and Paul Jagpal who have both provided valuable assistance concerning maintaining and modifying the experimental system in Birmingham.

My time in Birmingham would not have been the same without good friends Phil and Arvinder who were always available to share lunch or a pint (and even the odd trip to the Hawthorns). Thanks for all of the fun times and also the discussions concerning the trials and tribulations of completing a Ph. D which helped me through the more frustrating times.

Special thanks must go to my Mom, Dad, Kate, Robert and Barney who have always provided me with their love, support and encouragement over the last four years. My parents have always supported me in whatever I have decided to do in life and I am very grateful.

Finally I must thank my best-friend and partner Helen without whose never-ending help, encouragement and belief I would not have finished this thesis. I am eternally grateful to you for your love and support in accomplishing this dream.

Contents

List of Figures

List of Tables

Chapter 1

Introduction

The year 2011 marked the centenary of Rutherford's discovery of the atomic nucleus. During the last century the nuclear chart has grown to include many thousands of different nuclei of which only a few hundred are stable. Nuclear structure theories can replicate experimental data well where it exists for the stable nuclei and radioactive isotopes near the valley of nuclear stability. However when extending beyond regions of experimental measurements to increasingly unstable nuclei different nuclear theories diverge rapidly indicating that our understanding of the nuclear force remains incomplete. It is clearly important to extend experimental measurements as far from stability as possible to provide guidance points to assist the development of nuclear theory.

One nuclear property which is particularly useful is the nuclear charge distribution. A number of different types of experiment utilise the electromagnetic force to probe the charge distribution of the atomic nucleus. These include electron scattering, muonic atom spectroscopy, K X-ray measurements and laser spectroscopy. Each of these experiments measure different properties of the nuclear charge distribution with varying degrees of accuracy[1]. Combining the results from these experiments together enables accurate model independent values for the mean-square charge radius (MSCR) of the nucleus to be determined[2].

On initial inspection, laser spectroscopy seems an unlikely method for studying small changes in nuclear size due to the relative magnitudes of the nuclear radius and the wavelength of visible light photons. Laser spectroscopy photons typically have a wavelength of $\sim 10^{-7}$m which is several orders of magnitude greater than a typical nuclear radius of $\sim 10^{-15}$m. Clearly this mismatch is far too great for laser spectroscopy to directly

probe the nuclear radius. Instead laser spectroscopy stimulates transitions between the atomic energy levels in order to gain accurate transition energies. The magnitude of each individual atomic energy level is perturbed by small amounts due to the properties of the nucleus (which will be discussed in chapter 2 of this thesis). This leads to small changes in the transition energies for different isotopes. Laser spectroscopy experiments have great enough sensitivity and parts in 10^9 resolution to be able to detect these small shifts in transition energies and therefore provide an indirect method of measuring nuclear properties. Due to the fact that laser spectroscopy is an indirect method for probing the nucleus it is necessary to calibrate the measured data in order to extract the interesting nuclear information. Calibration is achieved by combining laser spectroscopy measurements with those obtained from the alternative experimental methods mentioned above. This combined analysis technique is discussed at length in section 5.4 of this thesis. Due to its high level of sensitivity, laser spectroscopy is the only technique capable of studying the properties of short lived radioactive isotopes and isomers. Laser spectroscopy is therefore an incredibly important tool for expanding nuclear measurements to isotopes further from stability.

An area of the nuclear chart that has been investigated by a significant number of laser spectroscopy experiments in recent years is the $Z \simeq 40$, $N \simeq 60$ region. Figure 1.1 below displays the change in MSCR, $\delta\langle r^2\rangle$, with neutron number N for the elements $36 \leq Z \leq 42$. At the $N = 50$ shell closure $\langle r^2\rangle$ is at a minimum in all element chains indicating very little nuclear deformation. This is true for all shell closures throughout the nuclear chart. As neutrons are added to the nucleus the charge radius increases in an approximately linear manner until $N = 60$. At $N = 60$ a sudden onset of deformation is observed for several elements. The sudden onset is initially observed in rubidium and increases in magnitude with Z until it reaches a maximum in the yttrium chain. The magnitude of this increase in deformation then decreases with Z and becomes washed out by the molybdenum chain. However, it should be noted that whilst the molybdenum chain does not exhibit a sudden onset of deformation at $N = 60$ it does still become significantly deformed by $N = 60$. Instead, the molybdenum chain increases in deformation much more gradually.

Currently no laser spectroscopy experiments have been conducted for the elements immediately above molybdenum in the nuclear chart. Technetium, $Z = 43$, possesses no stable isotopes which presents an experimental challenge as stable isotope measurements

are typically used to calibrate $\delta\langle r^2\rangle$ values for the unstable isotopes. The next element of ascending atomic number is $Z = 44$, ruthenium.

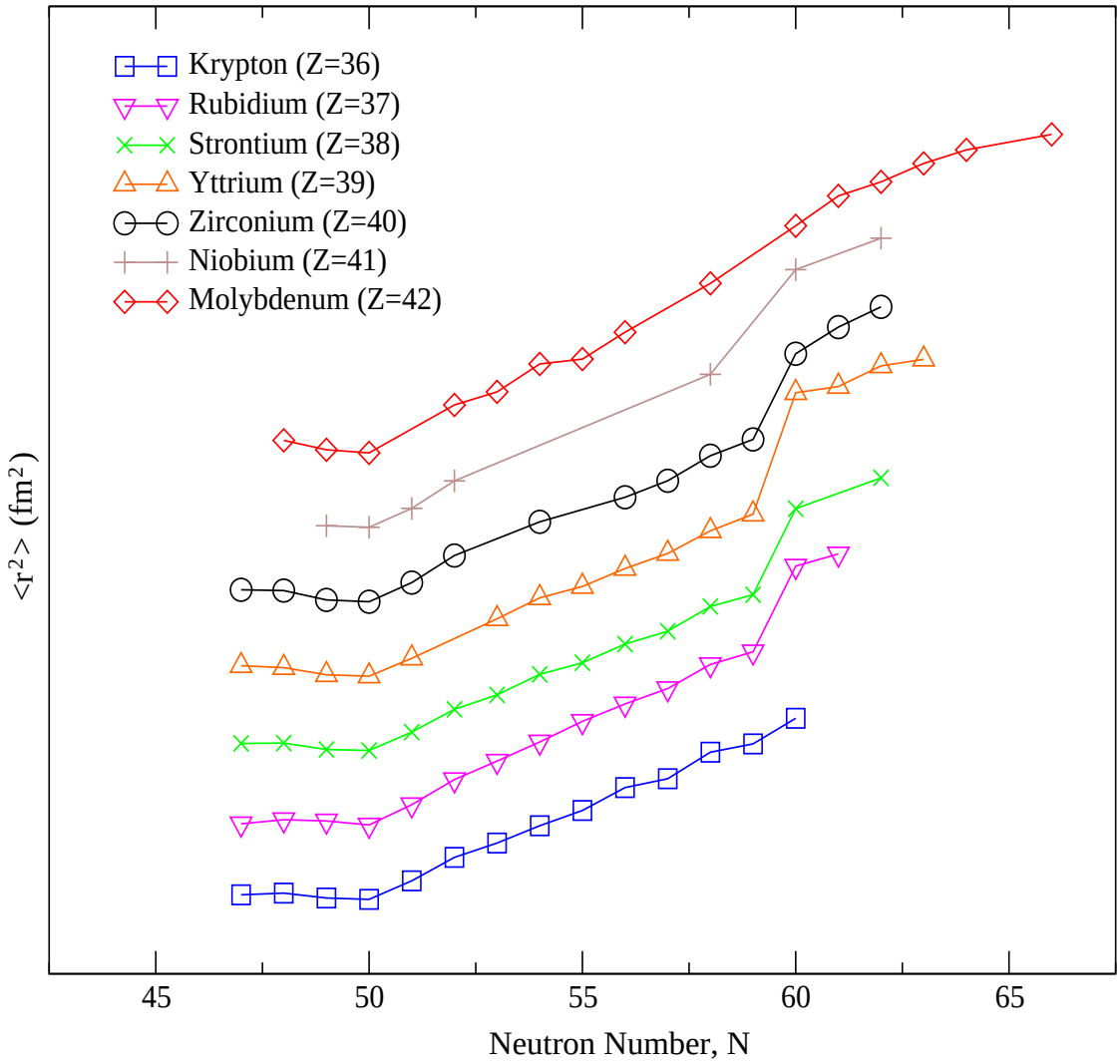

Figure 1.1: Change in mean-square charge radii, $\delta\langle r^2\rangle$ for Kr[3], Rb[4], Sr[5], Y[6], Zr[7], Nb[8] and Mo[9]. Each isotope chain for an element Z has been offset in the y-axis from the previous chain by an arbitrary amount for clarity. Error bars are smaller than the data points.

Ruthenium has seven stable isotopes; ^{96}Ru, ^{98}Ru, ^{99}Ru, ^{100}Ru, ^{101}Ru, ^{102}Ru and ^{104}Ru. Despite being relatively abundant and possessing a large number of stable isotopes surprisingly little experimental nuclear charge distribution data exists for stable ruthenium. A review by Fricke et al[2] reports that only muonic atom spectroscopy data exists for ruthenium and no laser spectroscopy, electron scattering or K X-ray work. Whilst no laser spectroscopy work has been performed for ruthenium a single optical transition has previously been measured using a hollow-cathode experiment[10]. The best set of MSCR data currently available for ruthenium is based upon a combined analysis of the muonic data and the hollow-cathode data performed by Fricke et al[2]. The

accuracy of these MSCR values is limited by the accuracy of the hollow-cathode experiment which is considerably lower than that from a laser spectroscopy experiment.

The main disadvantage of hollow-cathode experiments is the production of emission lines with a significant Doppler width. Laser spectroscopy experiments intersect a laser beam with a beam of atoms in order to dramatically reduce the Doppler broadening of spectral lines relative to a hollow-cathode light source[11]. There are two common laser spectroscopy geometries; crossed-beam spectroscopy, where the laser and atomic beams cross perpendicularly, and collinear laser spectroscopy where the laser and atomic beams are overlapped parallel to each other. For this thesis, crossed-beam laser spectroscopy was used to measure nineteen optical transitions in atomic ruthenium at the University of Birmingham. These measurements complement four other ruthenium transitions measured using the same experimental set-up by E. Cochrane in 1999.

This thesis will catalogue the measurement and analysis of these spectra in order to extract more accurate values for the MSCR of the stable ruthenium isotopes. Chapter 2 discusses the theoretical background to isotope shifts and hyperfine structures which are caused by interactions between the nucleus and the surrounding electron cloud. Chapter 3 gives an outline of high resolution laser spectroscopy techniques. Line broadening mechanisms are discussed and two experimental approaches to reduce this effect are considered. These are the crossed-beam technique, which was used for the data taken in this thesis and the collinear method which would be required in the future to extend the data to include radio-nuclides. A more detailed description of the laser and experimental equipment used to perform crossed-beam laser spectroscopy is discussed in chapter 4. Chapter 5 discusses at length the various analysis techniques required to extract the relevant atomic and nuclear parameters (such as the change in MSCR between isotopes) from the measured atomic spectra. This chapter also lists the various results obtained during this work. Chapter 6 considers the consequences of the work carried out during this thesis for future collinear measurements of the unstable isotopes of ruthenium. Finally, chapter 7 summarises the results obtained from this work.

Chapter 2

Theory

The gross structure of the electronic energy levels of an atom or ion can be calculated using the non-relativistic Schrödinger equation by assuming that the nucleus is infinitely massive and point-like. These calculations yield energy levels separated by the order of eV. Taking account of the interactions between the spin and orbital angular momenta of the electrons refines this model and splits the gross structure levels into the fine structure levels that are spaced by the order of meV. In reality the nucleus is neither infinitely massive nor point-like and accounting for the finite mass and volume of the nucleus causes further perturbations of the fine structure levels of the order of μeV. In atomic laser spectroscopy spectral lines are formed by stimulating transitions, via radiative absorption, between the electronic energy levels of an atom or ion and then observing the subsequent fluorescence. The frequency at which a spectral line occurs is therefore determined by the energy values of the electronic energy levels. The tiny perturbations of these energy levels due to the properties of the nucleus therefore results in small frequency shifts of spectral lines with respect to the infinite mass point-like nucleus model lines. Laser spectroscopy therefore provides an indirect method of measuring nuclear properties. The two nuclear effects which cause measureable perturbations on the electronic energy level structure are the isotope shift and hyperfine splitting.

2.1 Isotope Shift

For a given transition the corresponding spectral line will undergo a small frequency shift for different isotopes of the same element. This effect is known as the isotope shift and is expressed as follows [1],

$$\delta\nu_{IS}^{A,A'} = \nu^{A'} - \nu^{A}, \tag{2.1}$$

where ν^{A} and $\nu^{A'}$ represent the frequency of the transition in isotopes of mass number A and A' respectively (as illustrated in figure 2.1 below). The isotope shift is caused by the change in mass and charge distribution of the nucleus caused as neutrons are added or removed from the nucleus between different isotopes. It is separable into two components,

$$\delta\nu_{IS}^{A,A'} = \delta\nu_{MS}^{A,A'} + \delta\nu_{FS}^{A,A'}, \tag{2.2}$$

known as the mass shift $\delta\nu_{MS}^{A,A'}$ and the field shift $\delta\nu_{FS}^{A,A'}$.

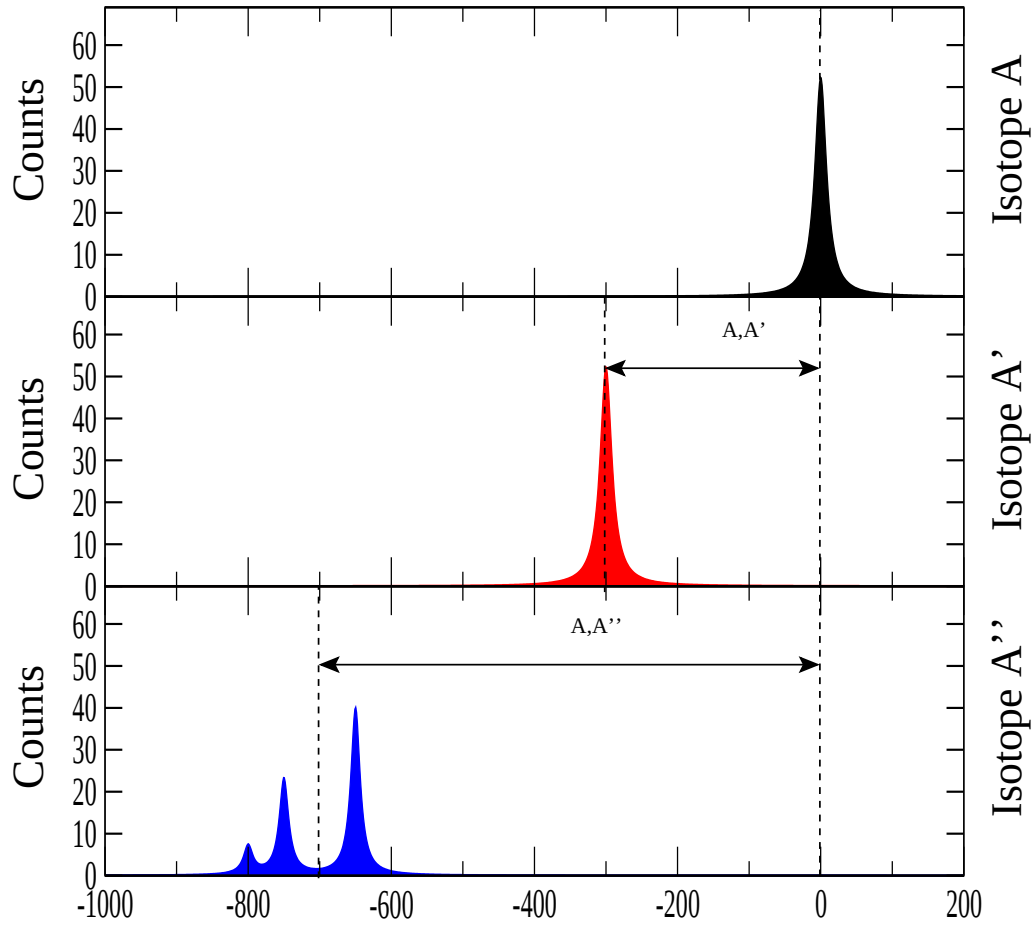

Figure 2.1: Simulated spectra illustrating the isotope shift between isotopes of different mass. The transition centroids are marked with dashed lines.

2.1.1 Mass Shift

The mass shift is a result of the change in mass between two isotopes. The variation in mass leads to a change in the recoil kinetic energy of the nucleus which in turn shifts the electronic energy levels. The total kinetic energy operator of an atom, T, can be calculated as follows,

$$T = \frac{\mathbf{p_n}^2}{2M} + \sum_i \frac{\mathbf{p_i}^2}{2m_e}, \tag{2.3}$$

where $\mathbf{p_n}$ and M are the momentum and mass of the nucleus and $\mathbf{p_i}$ and m_e are the momentum and mass of the ith electron. Conservation of momentum dictates that $\sum_i \mathbf{p_i} = -\mathbf{p_n}$ for a stationary atom. Substituting this relation into equation 2.3 yields the following,

$$\begin{aligned} T &= \frac{(\sum_i \mathbf{p_i})^2}{2M} + \frac{\sum_i \mathbf{p_i}^2}{2m_e} \\ &= \frac{\sum_i \mathbf{p_i}^2}{2M} + \frac{1}{M}\sum_{i>j} \mathbf{p_i}.\mathbf{p_j} + \frac{\sum_i \mathbf{p_i}^2}{2m_e} \\ &= \frac{\sum_i \mathbf{p_i}^2}{2\mu} + \frac{1}{M}\sum_{i>j} \mathbf{p_i}.\mathbf{p_j}, \end{aligned} \tag{2.4}$$

where $\mu = \frac{m_e M}{m_e + M}$ is the reduced mass. The first term in equation 2.4 is known as the normal mass shift whereas the second term is known as the specific mass shift. The normal mass shift is caused by the recoil kinetic energy of the nucleus as it orbits around the centre of mass it shares with the atomic electrons (see figure 2.2). An electronic energy level $E(M)$ for an atom with a nucleus of mass M is shifted with respect to the idealised case of an atom with a nucleus of infinite mass $E(\infty)$ as follows,

$$E(M) = E(\infty)\frac{M}{M + m_e}. \tag{2.5}$$

For an atom with an infinitely heavy nucleus the energy required to excite an electron from a low lying electronic energy level $E_L(\infty)$ to high lying energy level $E_H(\infty)$ can be calculated as follows,

$$E_\infty = h\nu_\infty = E_H(\infty) - E_L(\infty), \tag{2.6}$$

where ν_∞ is the transition frequency. For an atom with a nuclear mass M_1 the excitation energy E_1 can be calculated by substituting equation 2.5 into equation 2.6 as follows,

$$\begin{aligned} E_1 = h\nu_1 &= E_H(\infty)\frac{M_1}{M_1+m_e} - E_L(\infty)\frac{M_1}{M_1+m_e}, \\ &= [E_H(\infty) - E_L(\infty)]\frac{M_1}{M_1+m_e}, \\ &= \frac{M_1}{M_1+m_e}h\nu_\infty. \end{aligned} \tag{2.7}$$

Similarly a second isotope with nuclear mass M_2 has an excitation energy E_2 given by,

$$E_2 = \frac{M_2}{M_2+m_e}h\nu_\infty. \tag{2.8}$$

The different nuclear masses M_1 and M_2 result in the transition energy being different for the two isotopes. The shift in transition energy is calculated to an excellent approximation as follows,

$$\begin{aligned} \delta E^{M_1,M_2} &= \frac{M_2}{M_2+m_e}h\nu_\infty - \frac{M_1}{M_1+m_e}h\nu_\infty, \\ &= \left(\frac{M_2}{M_2+m_e} - \frac{M_1}{M_1+m_e}\right)h\nu_\infty, \\ &\approx \frac{M_2-M_1}{M_1M_2}m_e h\nu_\infty. \end{aligned} \tag{2.9}$$

The shift in transition energy results in a shift in transition frequency known as the normal mass shift (NMS) $\delta\nu_{NMS}^{A_1,A_2}$ which is expressed as,

$$\delta\nu_{NMS}^{A_1,A_2} = \frac{A_2-A_1}{A_1A_2}\frac{m_e}{u}\nu_\infty = N\frac{A_2-A_1}{A_1A_2} \tag{2.10}$$

where A_1 and A_2 are the atomic mass numbers of the isotopes with nuclear masses M_1 and M_2 respectively, u is the atomic mass unit and $N = \frac{m\nu_\infty}{u}$.

The second term in equation 2.4 is known as the specific mass shift (SMS) and is a consequence of correlations between the momenta of the atomic electrons. It is called the SMS because the magnitude of the correlation is dependent upon the specific state properties of the atomic electrons[1]. The SMS is expressed as,

$$\delta\nu_{SMS}^{A_1,A_2} = S\frac{A_2-A_1}{A_1A_2} \tag{2.11}$$

where S is an atomic factor dependent upon the electronic configurations of the transition states. Unlike the NMS (which is defined so that it is always positive) the SMS can be

either positive, so that it enhances the effect of the NMS, or negative so that it partially cancels out the NMS. For the case of a two electron atom, a positive specific mass shift is associated with the case where the electrons' spatial overlap is high and the electrons can be treated as a single particle of mass $2m_e$ orbiting the nucleus (see figure 2.3a below). A negative SMS (see figure 2.3b below) is associated with the case where the electrons orbit on opposite sides of the nucleus and in opposite directions so that their motion cancels out the nuclear motion[1]. The calculation of the SMS requires detailed knowledge of the electron wavefunctions which determine the value of the atomic factor S. This is challenging for multi-electron atoms.

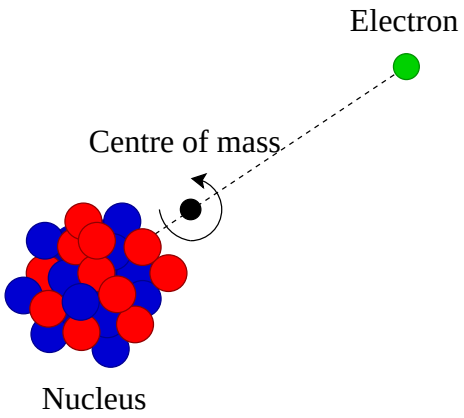

Figure 2.2: The Normal Mass Shift arises from the electron and nucleus of the atom orbiting around a common centre of mass.

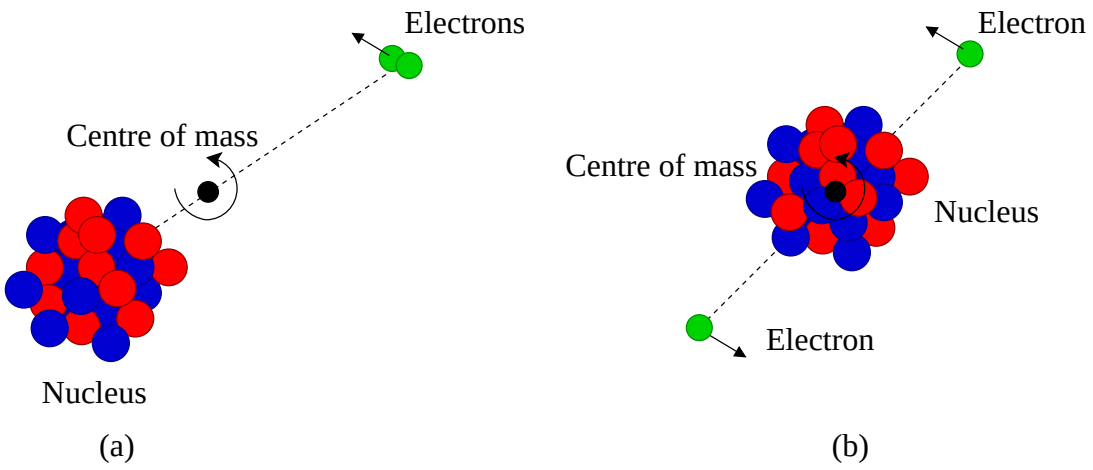

Figure 2.3: The effect of the Specific Mass Shift varies depending upon the configuration of the electrons.a) Two electrons with high spatial overlap. b) Two electrons with opposite momentum vectors.

The total mass shift can be found be adding together equations 2.10 and 2.11 as follows,

$$\delta\nu_{MS}^{A,A'} = \left(\frac{m_e}{u}\nu_0 + S\right)\frac{A' - A}{AA'} = \frac{A' - A}{AA'}M_i, \tag{2.12}$$

where M_i is a factor that contains all of the electronic information for the transition. The mass shift contains no interesting nuclear information as it is dependent only on atomic factors and isotopes' masses. However, the mass shift must be evaluated in order to extract the more valuable field shift from the total isotope shift.

2.1.2 Field Shift

The field shift is caused by the change in nuclear charge density between isotopes as neutrons are added to or removed from the nucleus. A nucleus that has infinite mass and is point-like produces an entirely Coulombic potential (see figure 2.4). If the nucleus has a finite size and mass then the electrostatic potential created by the nucleus deviates from the $1/r$ potential whilst inside the nuclear volume so that it has a finite value at $r = 0$. This effect shifts the electronic states upwards to less bound energies. The minimum of the nuclear potential varies depending upon the size of the nuclear radius so that the potential for a larger nucleus is shallower than that of a smaller nucleus. The field shift is most significant for transitions involving s (and to a lesser extent $p_{\frac{1}{2}}$) electrons which have a high probability of entering the nucleus.

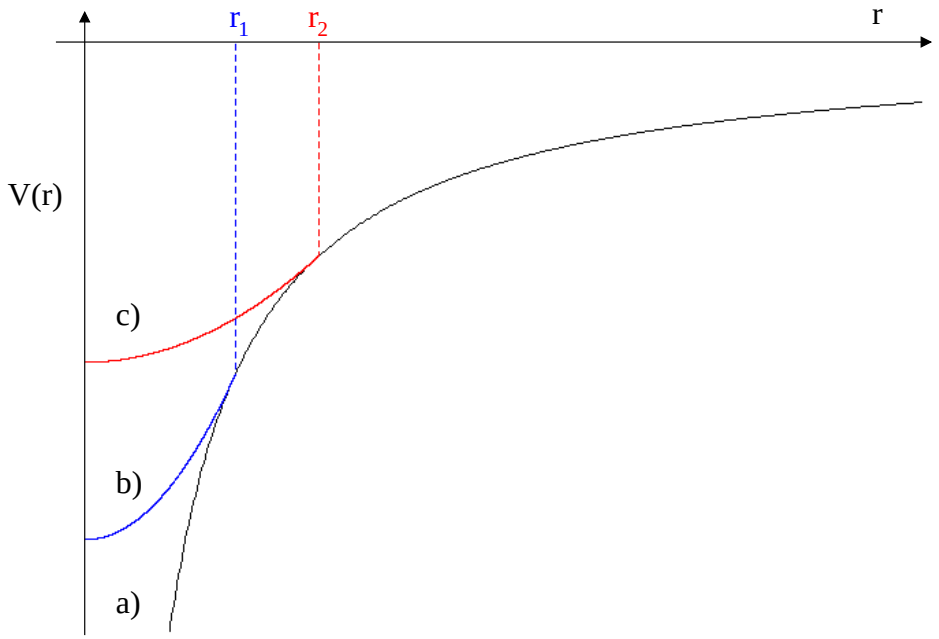

Figure 2.4: The nuclear potentials for: a) a point-like nucleus. b) a nucleus with radius r_1. c) a nucleus with radius r_2.

The magnitude of the field shift can be approximated using non-relativistic first order perturbation theory [12]. Starting from the simple case of a spherically symmetric nucleus with liquid-drop model radius $r_0 = R_0 A^{\frac{1}{3}}$ (where $R_0 = 1.2$fm), the first order contribution to the energy shift is the expectation value of the electrostatic potential energy difference $V(r) - V_0(r)$,

$$\begin{aligned} \Delta E &= \int_0^\infty \psi^*(V(r) - V_0(r))\psi 4\pi r^2 dr, \\ &\approx |\psi(0)|^2 \int_0^{r_0} (V(r) - V_0(r)) 4\pi r^2 dr. \end{aligned} \tag{2.13}$$

where $V_0(r)$ and $V(r)$ represent the electrostatic potential energy for a point like nucleus and a nucleus of radius r_0 respectively. The range of integration is restricted to $0 \leq r \leq r_0$ as $V(r) = V_0(r)$ for $r \geq r_0$. The electron probability density $|\psi(0)|^2$ is assumed to be approximately constant over the nuclear volume allowing it to be taken outside of the integral. The electrostatic potential for a finite uniformly charged spherically symmetric nucleus can be expressed as follows,

$$V(r) = \frac{Ze^2}{4\pi\epsilon_0 r_0}\left(-\frac{3}{2} + \frac{1}{2}\frac{r^2}{r_0^2}\right), 0 \leq r \leq r_0 \tag{2.14}$$

$$V(r) = -\frac{Ze^2}{4\pi\epsilon_0 r}, r \geq r_0. \tag{2.15}$$

Substituting equations 2.14 and 2.15 into equation 2.13 gives,

$$\Delta E = \frac{4\pi}{10}\left|\psi(0)\right|^2 \frac{Ze^2}{4\pi\epsilon_0} r_0^2. \tag{2.16}$$

The difference in the energy shift ΔE between two isotopes with different nuclear sizes is therefore as follows,

$$\delta(\Delta E) = \frac{4\pi}{5}\left|\psi(0)\right|^2 \frac{Ze^2}{4\pi\epsilon_0} r_0^2 \frac{\delta r_0}{r_0}. \tag{2.17}$$

which is more conventially rearranged as,

$$\delta(\Delta E) = \left|\psi(0)\right|^2 \frac{\pi a_0^3}{Z}\frac{2}{5} R_\infty \left(\frac{2Zr_0}{a_0}\right)^2 \frac{\delta r_0}{r_0} \tag{2.18}$$

$$\delta(\Delta E) = \left|\psi(0)\right|^2 \frac{\pi a_0^3}{Z} C\left(Z, r_0, \frac{\delta r_0}{r_0}\right), \tag{2.19}$$

where a_0 is the Bohr radius, R_∞ is the Rydberg constant and C is a factor dependent upon the changes of the nuclear charge density between two isotopes. Whilst equation 2.19 has the correct functional form it can only provide an order of magnitude estimate for the energy shift [12]. This is because the non-relativistic first order perturbation method fails to account for the distortion of the electron wavefunction inside a nucleus of finite volume. The electric potential is much less attractive for a finite nucleus compared to the standard Coulomb potential and so the electron density at the nucleus is reduced [1]. Equation 2.19 will therefore overestimate the extent of the field shift between two isotopes. Broch[13] developed a non-perturbative method for calculating the field shift which took into account the distortion of the electron wavefunction inside the nucleus. Bodmer extended this work and developed the following equation for the field shift[14],

$$\delta E = \left|\psi(0)\right|^2 \frac{\pi a_0^3 h}{Z} f(Z) \delta\langle r^2\rangle^{A,A'} \tag{2.20}$$

where $f(Z)$ is a factor that corrects the electron wavefunction for relativistic effects and the finite extent of the nucleus and $\delta\langle r^2\rangle^{A,A'}$ is the change in mean-square charge radius (MSCR) of the nucleus between isotopes of mass numbers A' and A. Equation 2.20

has the same form as equation 2.19 with $C = f(Z)\delta\langle r^2\rangle^{A,A'}$. The mean-square charge radius is a model-independent quantity defined as,

$$\langle r^2\rangle = \frac{\int_0^\infty 4\pi r^2\rho(r)r^2dr}{\int_0^\infty 4\pi\rho(r)r^2dr} = \frac{\int_0^\infty \rho(r)r^4dr}{\int_0^\infty \rho(r)r^2dr}, \tag{2.21}$$

where $\rho(r)$ is the nuclear charge density. Equation 2.20 yields the field shift for a single electron energy level between two isotopes however the experimentally observed quantity is the field shift for a transition between two atomic energy levels. The observed field shift in transition frequency $\delta\nu_{FS}^{A,A'}$ is,

$$\delta\nu_{FS}^{A,A'} = \frac{\pi a_0^3}{Z}\Delta\left|\psi(0)\right|^2 f(Z)\delta\langle r^2\rangle^{A,A'} \tag{2.22}$$

$$= F_i\delta\langle r^2\rangle^{A,A'}, \tag{2.23}$$

where F_i is the field factor and $\Delta\left|\psi(0)\right|^2$ is the change in electron charge density between the two transition levels. The field factor contains all of the electronic dependence for a given transition, i.

In reality, the electron wavefunction is not constant across the whole nuclear volume. This is especially true for heavier elements and a more accurate description of the field shift can be expressed as follows,

$$\delta\nu_{FS}^{A,A'} = F_i\lambda^{A,A'}, \tag{2.24}$$

where $\lambda^{A,A'}$, is the nuclear factor known as the Seltzer moment [15]. The Seltzer moment accounts for variations in electron wavefunction by expanding the nuclear charge dependence as a power series of radial moments as follows,

$$\lambda^{A,A'} = \delta\langle r^2\rangle^{A,A'} + \frac{C_2}{C_1}\delta\langle r^4\rangle^{A,A'} + \ldots, \tag{2.25}$$

where C_2 and C_1 are factors tabulated by Seltzer [15]. The Seltzer moment can be simplified as follows,

$$\lambda^{A,A'} = k\delta\langle r^2\rangle^{A,A'}. \tag{2.26}$$

where k accounts for the effect of higher order moments. The field shift can therefore be expressed as,

$$\delta\nu_{FS}^{A,A'} = F_i k \delta\langle r^2\rangle^{A,A'}. \tag{2.27}$$

where $\delta\langle r^2\rangle^{A,A'}$ is the change in mean-square charge radius (MSCR) between the two isotopes. For ruthenium, higher order moments typically contribute $\sim$2 – 3$\%$[2] to the Seltzer moment resulting in $k \simeq 0.97$ – 0.98.

2.1.3 Total Isotope Shift

Substituting equations 2.12 and 2.27 into equation 2.2 yields the total isotope shift between isotopes A and A' (where k in equation 2.27 has been set to one for simplicity).

$$\delta\nu_{IS}^{A,A'} = \frac{A'-A}{AA'}M_i + F_i\delta\langle r^2\rangle^{A,A'} \tag{2.28}$$

Laser spectroscopy measurements of the isotope shift between two isotopes can be used to determine the change in mean-square charge radius between them. The method of extracting $\delta\langle r^2\rangle^{A,A'}$ is discussed in detail in chapter 5.

2.2 Hyperfine Structure

Interactions between the electromagnetic multipole moments of the nucleus and the electromagnetic properties of the electron cloud lead to splitting of the fine structure energy levels. This effect is known as hyperfine splitting. The two dominant nuclear electromagnetic moments are the magnetic dipole moment and the electric quadrupole moment.

2.2.1 Magnetic Dipole Moment

The first hyperfine structure effect to be considered is the interaction between the nuclear magnetic dipole moment and the magnetic field at the nucleus produced by the orbiting electrons. The nuclear magnetic dipole moment ($\boldsymbol{\mu}_\mathbf{I}$) is aligned in the same direction as the nuclear spin vector $\mathbf{I}$ and hence its operator can be defined as follows,

$$\boldsymbol{\mu}_\mathbf{I} = \frac{\mu_I}{I}\mathbf{I}, \tag{2.29}$$

where μ_I is the scalar magnetic dipole moment. Similarly, the magnetic field, $\mathbf{B_{el}}$, is aligned anti-parallel to the total electronic angular momentum vector, $\mathbf{J}$, and so its operator can be defined as,

$$\mathbf{B_{el}} = -\frac{B_{el}}{J}\mathbf{J}, \tag{2.30}$$

where B_{el} is the scalar magnetic field and J is the scalar electronic angular momentum. The interaction energy can be determined using the following Hamiltonian [16],

$$H_M = -\boldsymbol{\mu}_\mathbf{I}.\mathbf{B_{el}}, \tag{2.31}$$

which can be expanded using equations 2.29 and 2.30 to produce the following,

$$H_M = (\frac{\mu_I B_{el}}{IJ})\mathbf{I}.\mathbf{J} = A_J\mathbf{I}.\mathbf{J}, \tag{2.32}$$

where,

$$A_J = \frac{\mu_I B_{el}}{IJ}, \tag{2.33}$$

is the magnetic hyperfine constant. By treating H_M as a small perturbation the first order approximation of the energy shift caused by this interaction is determined by the expectation value of H_M. In the absence of hyperfine interactions there is no coupling between the angular momenta of the electrons and nucleus. The wavefunctions of the whole system can therefore be separated into nuclear and electronic coordinates,

$$|\gamma I M_I J M_J\rangle = |\alpha I M_I\rangle\,|\beta J M_J\rangle\,, \tag{2.34}$$

where M_I and M_J are the z projections of I and J and α, β and γ represent any other quantum numbers required to represent the nuclear, electronic and total systems respectively. Using this uncoupled representation the energy shift has the following form,

$$\Delta E_M = \langle\gamma I M_I J M_J|\,H_M\,|\gamma I M_I J M_J\rangle = A_J\,\langle\gamma I M_I J M_J|\,\mathbf{I}.\mathbf{J}\,|\gamma I M_I J M_J\rangle\,. \tag{2.35}$$

This expectation value cannot be evaluated because $\mathbf{I}.\mathbf{J}$ does not commute with operators I_Z or J_Z. A new coupled representation is therefore required and can be formed from linear combinations of the unperturbed wavefunctions $|\gamma I M_I J M_J\rangle$ as follows,

$$|\gamma I J F M_F\rangle = \sum_{M_I M_J} \langle I M_I J M_J|I J F M_F\rangle\,|\gamma I M_I J M_J\rangle\,, \tag{2.36}$$

where F is a new quantum number representing the total angular momentum of the system. The total angular momentum vector $\mathbf{F}$, is defined as follows,

$$\mathbf{F} = \mathbf{I} + \mathbf{J}, \tag{2.37}$$

where vector coupling allows the quantum number F to range from $|I - J|$ to $I + J$ in increments of one. F is a good quantum number as operators $\mathbf{F^2}$ and F_z commute with the unperturbed Hamiltonian with eigenvalues of the standard angular momentum form $F(F + 1)$ and M_F respectively. Importantly, F also remains a good quantum number under the application of the perturbation H_M as $\mathbf{I}.\mathbf{J}$ commutes with the sum $I_z + J_z$. Using the new coupled basis the expectation value becomes,

$$\Delta E_M = A_J \left\langle \gamma I J F M_F \right| \mathbf{I}.\mathbf{J} \left| \gamma I J F M_F \right\rangle . \tag{2.38}$$

The vector product $\mathbf{I}.\mathbf{J}$ can be evaluated by squaring both sides of equation 2.37 to give,

$$\mathbf{F}^2 = (\mathbf{I} + \mathbf{J})^2, \tag{2.39}$$

$$\mathbf{F}^2 = \mathbf{I}^2 + \mathbf{J}^2 + 2\mathbf{I}.\mathbf{J}, \tag{2.40}$$

$$\mathbf{I}.\mathbf{J} = \frac{1}{2}\left[\mathbf{F}^2 - \mathbf{I}^2 - \mathbf{J}^2\right]. \tag{2.41}$$

Substituting equation 2.41 into equation 2.38 yields the following expression for the interaction energy:

$$\Delta E_M = \frac{A_J}{2} \left\langle \gamma I J F M_F \right| \left[\mathbf{F}^2 - \mathbf{I}^2 - \mathbf{J}^2\right] \left| \gamma I J F M_F \right\rangle , \tag{2.42}$$

$$\Delta E_M = \frac{A_J}{2}[F(F+1) - I(I+1) - J(J+1)] = \frac{A_J}{2}K, \tag{2.43}$$

where $K = [F(F + 1) - I(I + 1) - J(J + 1)]$. From equation 2.43 it is clear that there will be no interaction if the nuclear spin $I = 0$. This is because a nucleus with zero spin has no associated magnetic dipole moment. Similarly if $J = 0$ there will be no interaction as there will be no net magnetic field at the nucleus.

As previously mentioned, the quantum number F can take on any incremental value in the range $|I-J|$ to $I+J$. Equation 2.43 therefore has different values for each allowed value of F. The magnetic dipole interaction therefore splits a given fine structure level into $2I + 1$ (if $I \leq J$) or $2J + 1$ (if $J \leq I$) hyperfine structure levels [16] each of which possesses a specific value of F. If only the magnetic dipole interaction is considered, the separation between different F states obeys the following interval rule,

$$\Delta E(F) - \Delta E(F-1) = A_J F, \tag{2.44}$$

where the magnetic hyperfine parameter, A_J, determines the magnitude of the splitting. Measuring the frequency shift between hyperfine structure components in a spectrum therefore enables the value of A_J to be determined.

2.2.2 Electric Quadrupole Moment

The nuclear electric quadrupole moment can also contribute to the hyperfine structure by interacting electrostatically with the atomic electrons. The electrostatic interaction between a proton of charge e and an electron of charge $-e$ is,

$$H_E = \frac{-e^2}{4\pi\epsilon_0 \left|\mathbf{r_e} - \mathbf{r_p}\right|}, \tag{2.45}$$

where $\mathbf{r_e}$ and $\mathbf{r_p}$, see figure 2.5, are the coordinates of the electron and proton respectively with respect to the centre of mass of the nucleus (which is defined as the origin of the system). The total electrostatic interaction between the nucleus and the electrons is calculated by summing equation 2.45 over all electrons and protons in the system.

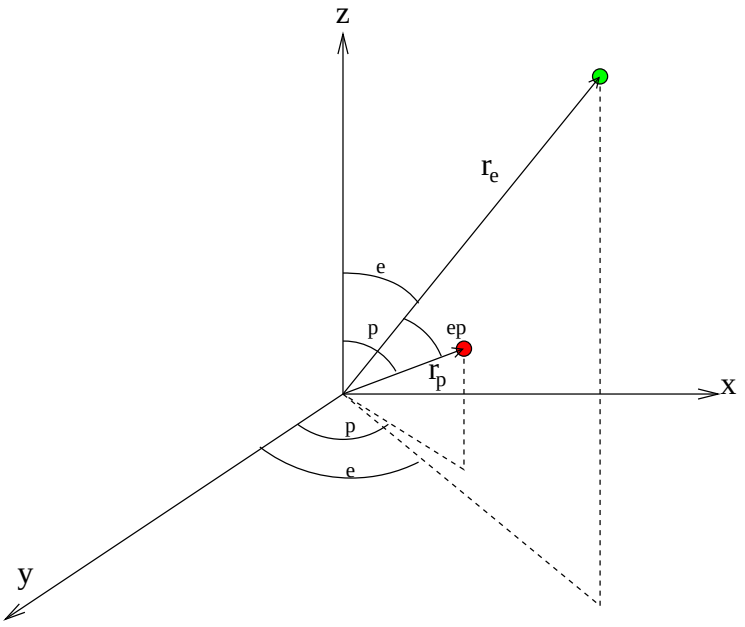

Figure 2.5: Coordinate system used to describe the electric quadrupole interaction.

So far the nucleus has been considered as point-like and spherically symmetric. In order to examine the effect of non-spherical nuclear charge distributions the nucleus

must be assigned electric multipole moments. This can be achieved through use of the following expression,

$$(\mathbf{r_e} - \mathbf{r_p})^2 = r_e^2 + r_p^2 - 2r_e r_p cos\theta_{ep}, \tag{2.46}$$

where θ_{ep} is the angle between the $\mathbf{r_e}$ and $\mathbf{r_p}$. Substituting equation 2.46 into equation 2.45 for the electrostatic interaction yields,

$$H_E = \frac{-e^2}{4\pi\epsilon_0} \left\{ r_e^2 + r_p^2 - 2r_e r_p cos\theta_{ep} \right\}^{-\frac{1}{2}}. \tag{2.47}$$

The term in braces is the generating function for the Legendre polynomials which enables (assuming that $r_e > r_p$) the interaction Hamiltonian to be expressed as:

$$H_E = \frac{-e^2}{4\pi\epsilon_0} \sum_k \frac{r_p^k}{r_e^{k+1}} P_k(cos\theta_{ep}), \tag{2.48}$$

$$= \frac{-e^2}{4\pi\epsilon_0 r_e} - \frac{e^2 r_p}{4\pi\epsilon_0 r_e^2} P_1(cos\theta_{ep}) - \frac{e^2 r_p^2}{4\pi\epsilon_0 r_e^3} P_2(cos\theta_{ep})... \tag{2.49}$$

where k is the order of the polynomial. The first term in equation 2.49 represents the electric monopole interaction which is used to determine the atomic gross structure energy levels. The second term represents the electric dipole interaction. This interaction is not allowed by nuclear symmetry and will be ignored. The third term represents the electric quadrupole interaction. The spherical harmonic addition theorem enables the Hamiltonian to be separated into nuclear and electronic coordinates,

$$H_E = \frac{-e^2}{4\pi\epsilon_0} \sum_k \frac{r_p^k}{r_e^{k+1}} \frac{4\pi}{2k+1} \sum_{q=-k}^{k} (-1)^q Y_k^{-q}(\theta_p\, \phi_p) Y_k^q(\theta_e\, \phi_e), \tag{2.50}$$

where Y_k^q are spherical harmonics of rank k and projection q. Equation 2.50 is the complete multipole expansion of the electrostatic interaction between the electrons and the nuclear charge distribution. The order of the multipole is denoted by the rank k where $k = 0$ is the monopole, $k = 1$ the dipole and $k = 2$ is the quadrupole. For most nuclei the highest significant multipole is the quadrupole and all other multipoles with $k > 2$ are negligible. The electric quadrupole interaction Hamiltonian is,

$$H_Q = \sum_{q=-2}^{2} (-1)^q \left\{ \left(\frac{4\pi}{5}\right)^{\frac{1}{2}} e r_p^2 Y_2^{-q}(n) \right\} \left\{ \left(\frac{4\pi}{5}\right)^{\frac{1}{2}} \frac{-e}{4\pi\epsilon_0 r_e^3} Y_2^q(e) \right\}, \tag{2.51}$$

$$\equiv \sum_{q=-2}^{2} (-1)^q Q_2^{-q}(p) W_2^q(e) \tag{2.52}$$

a scalar product between two rank two tensors. When summed over the protons and electrons this gives the total electric quadrupole interaction between the nucleus and the electrons. Classically, the electric quadrupole interaction energy has the following form[17],

$$E_Q \propto (\mathbf{rr}).(\nabla \mathbf{E}), \tag{2.53}$$

where $\mathbf{rr}$ is the quadrupole tensor and $\nabla\mathbf{E}$ is the electric field gradient. Comparing equation 2.53 to equation 2.52, the nuclear tensor $Q_2^{-q}(p)$ ($\propto r_p^2$) corresponds to the quadrupole moment and the electric tensor $W_2^q(e)$ ($\propto 1/r_e^3$) corresponds to the electric field gradient.

The electric tensor can be expressed in cartesian coordinates in terms of the electric potential at the nucleus V_e,

$$W \propto \begin{pmatrix} \frac{\partial^2 V_e}{\partial x \partial x} & \frac{\partial^2 V_e}{\partial x \partial y} & \frac{\partial^2 V_e}{\partial x \partial z} \\ \frac{\partial^2 V_e}{\partial y \partial x} & \frac{\partial^2 V_e}{\partial y \partial y} & \frac{\partial^2 V_e}{\partial y \partial z} \\ \frac{\partial^2 V_e}{\partial z \partial x} & \frac{\partial^2 V_e}{\partial z \partial y} & \frac{\partial^2 V_e}{\partial z \partial z} \end{pmatrix} \tag{2.54}$$

In order to simplify matters, the electronic coordinate system (x, y, z) can be chosen so that the non-diagonal elements of the electric tensor are equal to zero (i.e. W becomes diagonal). The electronic potential has axial symmetry about the total electronic angular momentum vector $\mathbf{J}$ so that,

$$\frac{\partial^2 V_e}{\partial x^2} = \frac{\partial^2 V_e}{\partial y^2}, \tag{2.55}$$

Also, by assuming that the electric field has a source external to the nucleus and falls to zero at the centre of the nucleus, Laplace's equation applies as follows,

$$\nabla^2 V_e = \frac{\partial^2 V_e}{\partial x^2} + \frac{\partial^2 V_e}{\partial y^2} + \frac{\partial^2 V_e}{\partial z^2} = 0, \tag{2.56}$$

and using equation 2.55,

$$\frac{\partial^2 V_e}{\partial x^2} = \frac{\partial^2 V_e}{\partial y^2} = -\frac{1}{2}\frac{\partial^2 V_e}{\partial z^2}. \tag{2.57}$$

Therefore the diagonal components of the electronic tensor W can all be expressed in terms of the z component. In spherical coordinates this is equivalent to the expectation value of the W_2^0 component of the electronic tensor for the state $|J, M_J = J\rangle$. Therefore the average gradient of the electric field produced by the electrons at the nucleus is defined as follows,

$$\frac{1}{e}\langle J, J| \frac{\partial^2 V_e}{\partial z^2} |J, J\rangle = \frac{2}{e}\langle J, J| \sum_i W_2^0(e)_i |J, J\rangle \tag{2.58}$$

$$= -\langle J, J| \sum_i \frac{(3cos^2\theta_{e_i} - 1)}{r_{e_i}^3} |J, J\rangle , \tag{2.59}$$

where the sum is over all i electrons. Similarly, the nuclear electric quadrupole tensor can be determined by rotating the nuclear coordinate system (x', y', z') so that the nuclear tensor Q_2^{-q} is diagonalised. The intrinsic nuclear electric quadrupole moment can then be defined as the expectation value of the Q_2^0 component of the nuclear tensor for the state $|I, M_I = I\rangle$ as follows,

$$Q_0 \equiv \frac{2}{e}\langle I, I| \sum_i Q_2^0(p)_i |I, I\rangle , \tag{2.60}$$

$$= \langle I, I| \sum_i r_{p_i}^2 (3cos^2\theta_{p_i} - 1) |I, I\rangle . \tag{2.61}$$

where the sum is over all i protons in the nucleus. In the nuclear coordinate system, $z' = r_p cos\theta_p$ so that in Cartesian coordinates the intrinsic quadrupole moment is,

$$Q_0 = \langle I, I| \sum_i (3z_i'^2 - r_{p_i}^2) |I, I\rangle . \tag{2.62}$$

From equation 2.62 it can be shown that when the nuclear charge is distributed primarily in the $x' - y'$ plane (so that distribution in z' is small), $Q_0 < 0$. This charge distribution is known as oblate deformation. When the nuclear charge is distributed along the z' axis (i.e. along the axis of $\mathbf{I}$ so that $r_{p_i} \approx z'^2$), $Q_0 > 0$. This charge distribution is known as prolate deformation. When the nucleus is spherical in shape (i.e. $x'^2 = y'^2 = z'^2$ so that $r_p^2 = 3z'^2$) $Q_0 = 0$.

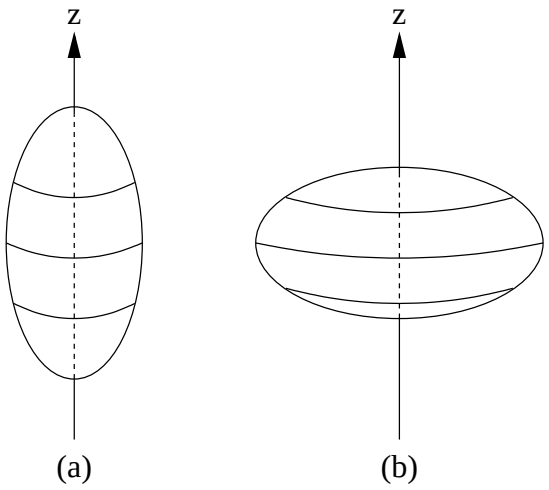

Figure 2.6: (a) Prolate quadrupole deformation. (b) Oblate quadrupole deformation.

The full evaluation of the scalar product in equation 2.52 was performed by Casimir [18] and gives the Hamiltonian for the quadrupole interaction as,

$$H_Q = eQ_s \left\langle \frac{\partial^2 V_e}{\partial z^2} \right\rangle \frac{[3(\mathbf{I}.\mathbf{J})^2 + \frac{3}{2}\mathbf{I}.\mathbf{J} - I(I+1)J(J+1)]}{2I(2I-1)J(2J-1)}, \tag{2.63}$$

where Q_s is the spectroscopic quadrupole moment. The intrinsic quadrupole moment Q_0 is defined in the body-fixed nuclear coordinate system (x', y', z'). However, experimental measurements are made in the space-fixed system (x, y, z) of the electrons. The electric quadrupole moment measured in the electronic coordinate system is known as the spectroscopic quadrupole moment Q_s. The intrinsic and spectroscopic quadrupole moments can be related using the following equation,

$$Q_s = Q_0 \left[\frac{3\Omega^2 - I(I+1)}{(I+1)(2I+3)} \right] \tag{2.64}$$

where Ω is the projection of the nuclear spin vector onto the nuclear symmetry axis. For most ground state nuclei it can be assumed that $\Omega = I$ [19].

The first order energy shift due to the electromagnetic quadrupole interaction can therefore be calculated as follows,

$$\Delta E_Q = \langle IJFM_F | \, H_Q \, | IJFM_F \rangle \tag{2.65}$$

$$= \frac{1}{4} e \left\langle \frac{\partial^2 V_e}{\partial z^2} \right\rangle Q_0 \left[\frac{3\Omega^2 - I(I+1)}{(I+1)(2I+3)} \right] \frac{\frac{3}{2}K(K+1) - 2I(I+1)J(J+1)}{I(2I-1)J(2J-1)} \tag{2.66}$$

$$= \frac{B}{4} \frac{\frac{3}{2}K(K+1) - 2I(I+1)J(J+1)}{I(2I-1)J(2J-1)} \tag{2.67}$$

where K has the same definition as in equation 2.43 and B is the electric quadrupole hyperfine parameter defined as follows,

$$B = eQ_s \left\langle \frac{\partial^2 V_e}{\partial z^2} \right\rangle. \tag{2.68}$$

From equation 2.64 it can be shown that for $I = 0$ or $I = 1/2$ the spectroscopic quadrupole moment $Q_s = 0$ and therefore there is no electric quadrupole interaction. This is because for $I < 1$ the nucleus appears spherical in the electronic space-fixed frame and so there can be no observable quadrupole interaction (even if Q_0 is non-zero). Similarly, if $J = 0$ or $J = 1/2$ the electron charge distribution appears spherical and there is no quadrupole interaction.

2.3 Total Hyperfine Splitting

The total change in energy of a fine structure level due to hyperfine interactions is the sum of equations 2.43 and 2.67,

$$\Delta E_{hf} = \frac{A}{2}K + \frac{B}{4}\frac{\frac{3}{2}K(K+1) - 2I(I+1)J(J+1)}{I(2I-1)J(2J-1)}. \tag{2.69}$$

Figure 2.7 displays two fine structure levels $J = 0$ and $J = 1$. If the nucleus has non-zero nuclear spin, for example $I = 1$, the upper fine structure level will split due to the magnetic dipole interaction. The lower energy level will not split as $J = 0$ and therefore there is no net magnetic field produced by the electrons. If the nucleus is spherical (i.e. $Q_0 = 0$) there will be no electromagnetic quadrupole interaction and the separation between the hyperfine levels will obey the interval rule outlined in section 2.2.1 above. If $Q_0 \neq 0$ the electric quadrupole interaction causes further shifting of the hyperfine energy levels and the magnetic dipole interval rule is no longer valid.

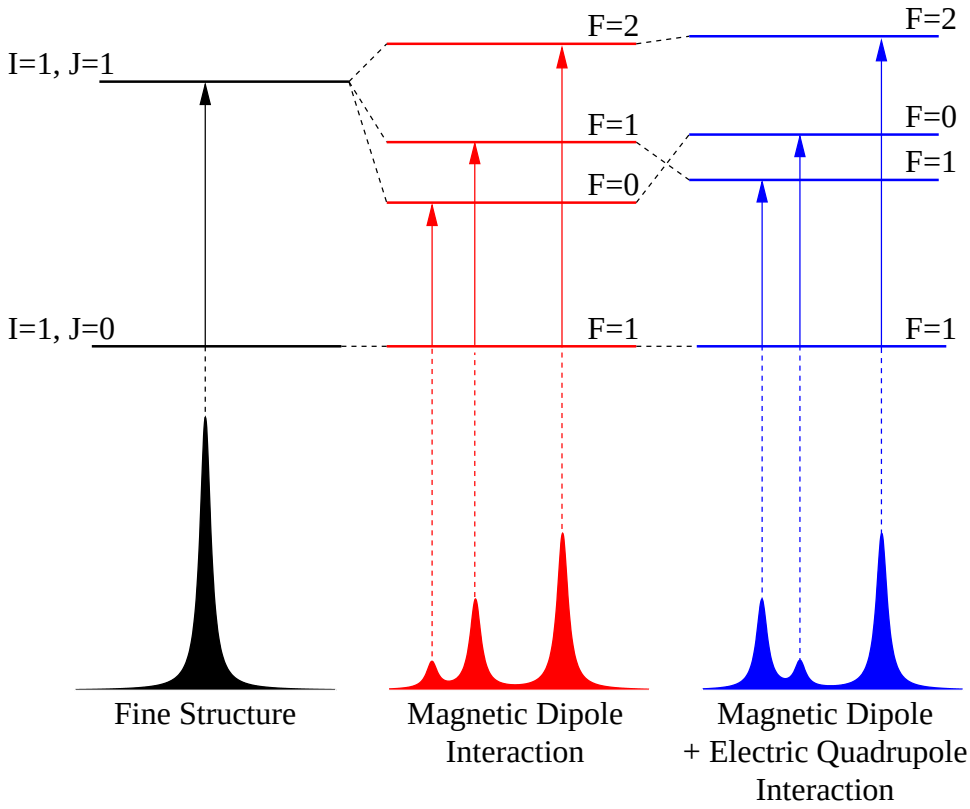

Figure 2.7: The fine structure spectral line is split into three hyperfine structure lines by the magnetic dipole interaction. The electric quadrupole interaction causes further perturbation to the hyperfine energy levels resulting in a different observed spectrum.

The images below the level diagrams in figure 2.7 display how the spectrum obtained from transitions between the two fine structure levels varies as the effect of the hyperfine interactions are considered. The magnitude of the hyperfine shifts are determined by the hyperfine parameters A and B. The frequency of a transition between hyperfine states can be expressed in terms of A and B as follows,

$$\nu(F_L \to F_U) = A_U\alpha(F_U) + B_U\beta(F_U) + \omega - A_L\alpha(F_L) - B_L\beta(F_L), \tag{2.70}$$

where ω is the frequency of the transition in the absence of hyperfine interactions and $\alpha(F_{U,L})$ and $\beta(F_{U,L})$ are expressed as follows,

$$\alpha(F_{U,L}) = \frac{K(F_{U,L})}{2}, \tag{2.71}$$

$$\beta(F_{U,L}) = \frac{\frac{3}{2}K(F_{U,L})\left\{K(F_{U,L})+1\right\} - 2I(I+1)J_{U,L}(J_{U,L}+1)}{I(2I-1)J_{U,L}(2J_{U,L}-1)}. \tag{2.72}$$

The measurement of the transition frequencies $\nu(F_L \rightarrow F_U)$ between hyperfine structure levels therefore enables A and B to be experimentally determined.

2.4 Extraction of Nuclear Parameters

Measuring the frequency of the transitions between hyperfine energy levels via laser spectroscopy enables the hyperfine parameters A and B to be determined. Once A and B have been measured the magnetic dipole moment μ_I, and electric quadrupole moment Q, can be extracted from them. It is clear from equations 2.33 and 2.68 that determining μ_I and Q from the A and B parameters requires knowledge of the magnetic field at the nucleus B_e and the electron electric field gradient $\frac{\partial^2 V_e}{\partial z^2}$, respectively. These factors are extremely difficult to calculate accurately [20]. In order to remove these two factors the ratio between hyperfine parameters is used as follows [21],

$$\frac{A_1}{A_2} = \frac{(\mu/I)_1}{(\mu/I)_2}, \tag{2.73}$$

$$\frac{B_1}{B_2} = \frac{Q_1}{Q_2}, \tag{2.74}$$

where the subscripts 1 and 2 denote different isotopes. If the moments are known for one isotope then equations 2.73 and 2.74 can be used to determine the unknown moments for the second isotope.

The magnitude and sign of the intrinsic quadrupole moment provides a measure of the size and shape of the deformation of the nucleus. The intrinsic quadrupole moment can be approximated in terms of the quadrupole deformation parameter, β_2 as follows [19],

$$Q_0 \approx \frac{3Z\,\langle r\rangle_0^2}{\sqrt{5\pi}}\langle\beta_2\rangle(1+0.36\langle\beta_2\rangle), \tag{2.75}$$

where Z is the atomic number and $\langle r\rangle_0^2$ is the MSCR of a spherical nucleus of the same volume.

The nuclear mean-square charge radius is also dependent upon the nuclear deformation as follows,

$$\langle r^2\rangle = \langle r_0^2\rangle\left(1+\frac{5}{4\pi}\sum_i\langle\beta_i^2\rangle\right) \tag{2.76}$$

where $\langle \beta_i^2 \rangle$ is the mean-square deformation parameter, i is the order of multipole deformation and $\langle r_0^2 \rangle$ is the MSCR of a spherical nucleus of the same volume as the distorted nucleus. The quadrupole is the most dominant multipole and so the MSCR can be approximated as being dependent upon the mean-square quadrupole deformation parameter, $\langle \beta_2^2 \rangle$. If the nucleus exhibits large quadrupole deformation (i.e. large β_2) then the MSCR will be substantially affected [19].The MSCR is also sensitive to the dynamic nature of the deformation of the nucleus. This is due to the fact that the MSCR is dependent upon the mean-square quadrupole deformation parameter, $\langle \beta_2^2 \rangle$, which may be large due to nuclear fluctuations about the zero point (see figure 2.8), even if there is no net nuclear deformation (i.e. if β_2 itself is small or negligible).

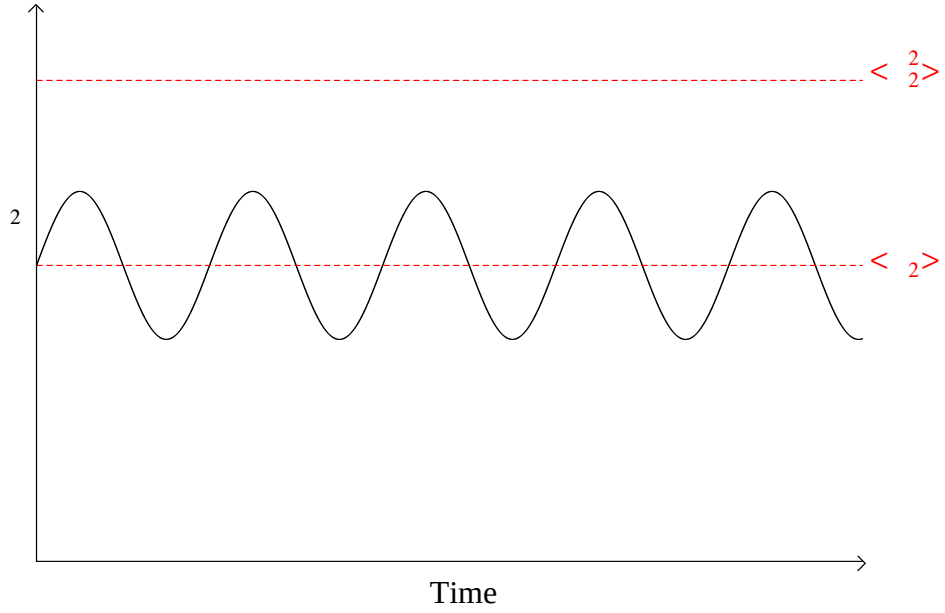

Figure 2.8: Quadrupole deformation parameter, β_2, as a function of time for a nucleus exhibiting dynamic deformation.

In comparison, the quadrupole moment is only dependent upon the mean-quadrupole deformation parameter $\langle \beta_2 \rangle$ which averages out dynamic deformation effects. The extent of dynamic nuclear deformation can therefore be determined by comparing $\langle \beta_2 \rangle^2$, obtained from Q_0, to $\langle \beta_2^2 \rangle$, obtained from $\langle r_0^2 \rangle$.

Chapter 3

High Resolution Laser Spectroscopy

Laser spectroscopy involves stimulating transitions between the electronic energy levels of an atom or ion in order to produce a spectrum. Figure 3.1 displays an electronic energy level system with two levels E_1 and E_2. An electron in the lower energy level E_1 can be excited to the upper energy level E_2 by absorbing a photon of energy E and frequency ν where,

$$E = h\nu = E_2 - E_1. \tag{3.1}$$

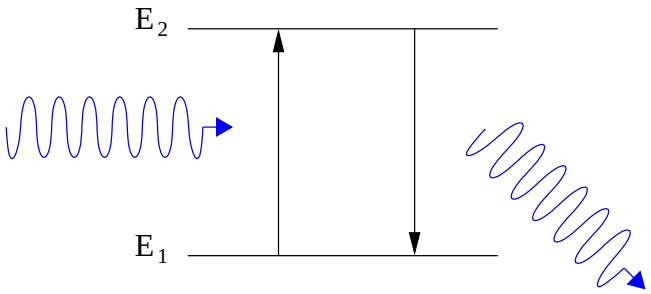

Figure 3.1: Laser Spectroscopy.

Once excited to E_2 the atoms may relax back down to state E_1 by spontaneously emitting a photon of energy E and frequency ν.

Due to it possessing a high energy density localised over a small spatial beam and narrow frequency range, a laser is an ideal source of photons for use in spectroscopy work. The standard laser spectroscopy procedure is to direct a laser beam onto a sample of atoms or ions and to vary the laser frequency ν. When the laser frequency matches the resonant frequency of the atom or ion, fluorescent photons will be emitted. As a

typical laser has a frequency width less than the natural line-width of the transition being stimulated all of the laser power has the potential to stimulate the desired transition. A spectrum is then formed by measuring the production of resonant photons as a function of laser frequency. The power of laser spectroscopy as an experimental method is due to its high sensitivity and resolution. The sensitivity of laser spectroscopy is due to the fact that the resonant photon absorption cross-section of an atom is roughly proportional to the square of the photon wavelength [22, 23]. For visible photons this results in an absorption cross-section that is approximately six orders of magnitude greater than the physical size of the atom. The high level of sensitivity ensures that a detectable number of resonant photons can be produced from even very small samples of material.

3.1 Line Broadening Mechanisms

3.1.1 The Natural Linewidth

In an idealised situation the transition wavelength between two electron energy levels is monochromatic. In reality this is never the case due to the uncertainty principle,

$$\Delta E.\tau \simeq \hbar \tag{3.2}$$

All electronic energy levels (with the exception of the ground state level) have a relaxation lifetime, τ. According to equation 3.2 the lifetime of the state results in each level possessing a finite spread in energy, ΔE. The emitted photons can therefore exhibit a narrow range of frequencies centered on the idealised transition frequency, ν_0, as illustrated by figure 3.2.

The total energy uncertainty for a spectral line is therefore determined by the sum of the lifetimes of the transition upper and lower states, τ_u and τ_l respectively, as follows,

$$\Delta E = \Delta E_u + \Delta E_l = \hbar \left(\frac{1}{\tau_u} + \frac{1}{\tau_l} \right). \tag{3.3}$$

This frequency distribution of the emitted intensity is known as the natural linewidth and it provides a fundamental limit to the resolution of laser spectroscopy measurements. Other line broadening mechanisms discussed later in this section can be reduced via careful experimental design however the natural linewidth is dependent upon the state lifetime and therefore cannot be circumvented. A full semi-classical calculation reveals

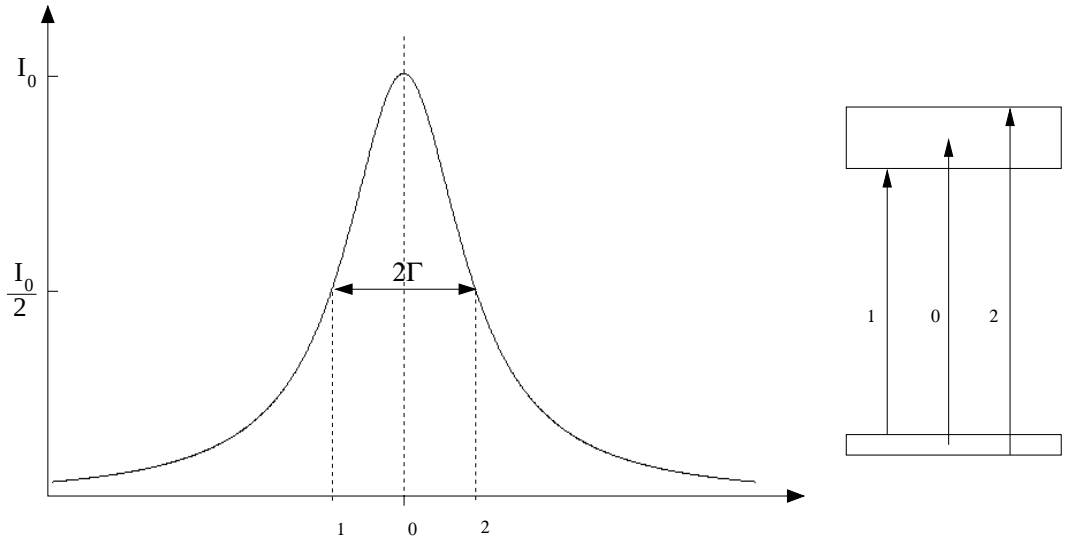

Figure 3.2: Natural Linewidth.

that the natural linewidth induced intensity distribution of a transition is described by a Lorentzian profile [24],

$$L(\nu) = L_0 \frac{\Gamma^2}{(\nu_0 - \nu)^2 + \Gamma^2}, \tag{3.4}$$

where $2\Gamma = 1/\tau_u + 1/\tau_l$ is the full-width-half-maximum (FWHM) of the distribution and L_0 is the maximum intensity at $\nu = \nu_0$. In the case of optical transitions from the ground state the natural linewidth is determined by the upper state lifetime only. For typical transitions used in laser spectroscopy experiments the upper state lifetime is $\sim 10^{-7}$s which results in a natural linewidth of a few tens of MHz. The natural linewidth is therefore much narrower than the frequency spacing associated with hyperfine structure and isotope shifts which are typically a few hundred MHz in magnitude. The laser used in this work has a frequency width of $\sim$2MHz. This would mean that for interactions with a stationary atom the measured intensity profile would be determined by the Lorentzian profile of the transition. Unfortunately this is not often the case due to the other broadening mechanisms that will be discussed now.

3.1.2 Power Broadening

For high incident laser power it is possible that the rate of absorption of electrons from the transition lower state to the upper state exceeds the rate of relaxation transitions

from the upper state back to the lower state. In this situation the transition lower state becomes depopulated and unable to absorb further laser photons. Just as the emitted intensity distribution possesses a Lorentzian profile due to the natural width, the atom also has a Lorentzian shaped absorption profile centred on the transition frequency. The absorption rate is therefore greater at the absorption profile central frequency than in the wings of the distribution. This results in the centre of the profile depopulating more rapidly than those atoms in the wings. The photon emission profile therefore saturates at the central frequency for high laser power whereas the intensity of the wings is able to increase resulting in a broadened profile. This effect, known as power broadening, can be overcome by ensuring that the laser power density is not too high when interacting with the atom sample. This can be achieved by reducing the laser power or increasing the size of the laser beam spot.

3.1.3 Doppler Broadening

A significant source of line-broadening is the Doppler shift of the atomic transition due to the velocity distribution of the atoms. Those atoms with a velocity component that is anti-parallel to the incident laser beam, v, observe a Doppler shifted laser frequency, ν_{obs},

$$\nu_{obs} \simeq \nu_0 \left(1 + \frac{v}{c}\right), \tag{3.5}$$

where ν_0 is the unshifted atomic transition frequency. An atom travelling towards the laser beam, with velocity component $+v$, will therefore observe a different laser frequency than a stationary atom, $v = 0$, or an atom moving away from the laser beam with velocity $-v$. Different atoms will therefore undergo resonant transitions at different laser frequencies depending upon their velocity. For a gas at thermal equilibrium, the velocity distribution of its atoms can be represented by a Maxwell distribution which, when ignoring the natural linewidth, results in the Doppler intensity profile having the following form [24],

$$G(\nu) = I_0 exp\left(-\frac{mc^2}{2k_B T}\left(\frac{\nu - \nu_0}{\nu_0}\right)^2\right) \tag{3.6}$$

where T is the temperature of the gas and I_0 is the maximum intensity at the centre of the profile where $\nu = \nu_0$. The Doppler broadened line profile, $G(\nu)$ given by equation

3.6, is a Gaussian lineshape with a full-width-half-maximum, $FWHM$, of,

$$FWHM = \left(\frac{\nu_0}{c}\right)\sqrt{\frac{8k_BTln2}{m}}. \tag{3.7}$$

Using equation 3.7, the FWHM of the 349.8942nm transition for ^{102}Ru at $T \sim 2600K$ (the melting point of ruthenium) is $\simeq$1.5GHz. This is considerably greater than the natural line-width and importantly it is much larger than the typical isotope shifts observed in ruthenium (which are typically $\sim$ 100 – 500MHz). Doppler broadening is therefore a factor that can severely limit the ability of laser spectroscopy experiments to measure isotope shifts and hyperfine structure.

In reality the Doppler broadened linewidth is not represented by a pure Gaussian line profile because each population of atoms, with velocity component v, possesses a range of absorption/emission frequencies due to the natural linewidth. The natural line width has a Lorentzian profile as defined in equation 3.4 so the total observed line profile is a Gaussian distribution of velocity populations which each exhibit a Lorentzian natural line profile. The observed line profile can therefore be represented by a Voigt profile, $V(\nu)$, which is a convolution of Lorentzian and Gaussian line shapes:

$$V(\nu) = \int_{-\infty}^{\infty} G(\nu')L(\nu - \nu')d\nu', \tag{3.8}$$

where $L(\nu - \nu')$ and $G(\nu')$ are expressed in equations 3.4 and 3.6 respectively.

3.2 Doppler Reduced High Resolution Laser Spectroscopy Methods

3.2.1 Crossed Beam Laser Spectroscopy

Crossed-beam laser spectroscopy experiments overlap a laser beam perpendicularly with an atomic beam in order to reduce Doppler broadening. Figure 3.3 displays a schematic outline of a typical crossed-beam experiment. An oven is used to form a plume of the atoms of the element under study which is then formed into a beam through the use of narrow collimation slits. The slits only allow atoms with near-vertical velocity components to reach the region where interaction with the laser beam occurs. The atoms in the collimated atomic beam therefore possess only a small velocity component in

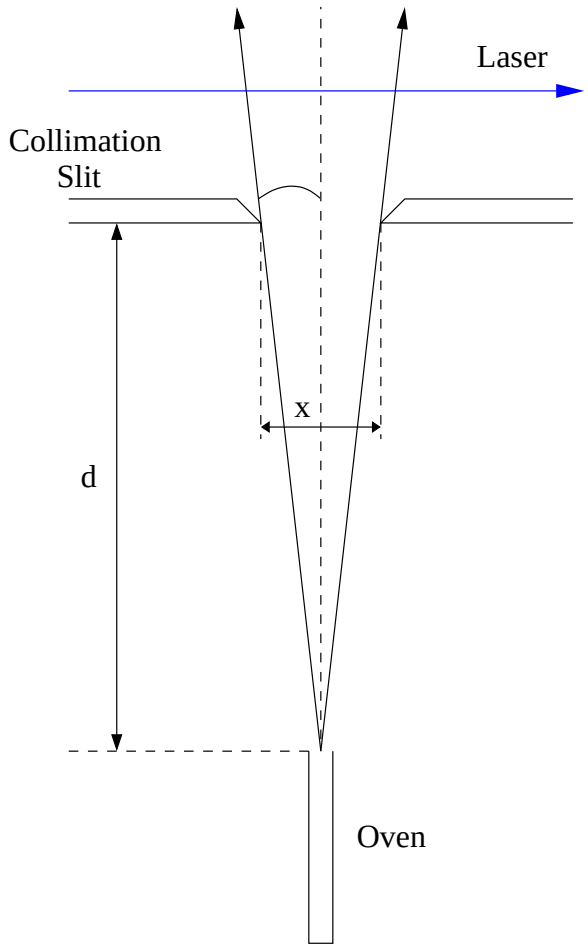

Figure 3.3: Outline of a crossed-beam laser spectroscopy experiment.

the direction travelling parallel to the laser beam. As it is only atomic motion directly towards (or away) from the laser beam that contributes towards Doppler broadening, the crossed-beam experimental geometry has a reduced Doppler width.

It can be shown[24] that the Doppler width, $d\nu$, of a spectral line measured using crossed-beam spectroscopy is reduced to,

$$d\nu = d\nu_0 \sin\theta, \tag{3.9}$$

where $d\nu_0$ is the Doppler width for an uncollimated beam of thermal atoms and the Doppler width reduction factor, $\sin\theta$, is calculated as follows,

$$\sin\theta \simeq \frac{x}{2d}, \tag{3.10}$$

where θ is the collimation angle, x is the slit width and d is the oven to slit distance as displayed in figure 3.3. Typically, crossed-beam experiments utilise narrow slits with

x ∼1mm and large oven-to-slit distances of d ∼a few tens of centimetres in order to reduce the Doppler width by two to three orders of magnitude. At this level of reduction, the Doppler width is of a similar magnitude as the natural linewidth enabling the resolution of isotope shifts and hyperfine structure.

The crossed-beam spectroscopy method is advantageous due to the simplicity of the equipment involved. An atomic beam can be formed relatively easily via the heating of a sample in an oven and collimated sufficiently over a small distance of a few tens of centimetres. Over such small distances a vacuum pressure of approximately 10^{-6} mbar is required to ensure that the mean-free path of the atomic beam is greater than the oven-to-laser distance and this can be achieved simply with diffusion or turbo pumps. The main disadvantage of this method is that it is not very efficient[22]. A significant percentage of the atoms produced by the oven are blocked by the collimation slits and therefore never interact with the laser beam to produce resonance photons. As a result of this, the technique is limited to the use of stable isotopes or long-lived radioactives [20].

3.2.2 Collinear Laser Spectroscopy

Collinear laser spectroscopy experiments overlap a laser beam with an electrostatically accelerated beam of ions travelling in a direction parallel to the laser beam. Kaufman[25] and Wing et al.[26] independently determined that accelerating a beam of ions reduces the width of their velocity distribution. The kinetic energy of an ion is,

$$E = \frac{1}{2}mv^2, \tag{3.11}$$

and differentiating yields

$$dE = mvdv, \tag{3.12}$$

$$dv = \frac{dE}{mv}. \tag{3.13}$$

For a constant energy spread, dE, the velocity spread of a beam of the ions, dv is reduced by increasing the velocity of the ions, v. This effect is illustrated in figure 3.4. The Doppler width of a measured spectral line is determined by the magnitude of the velocity distribution dv and is therefore reduced by ion acceleration. Typically electrostatic acceleration voltages of the order of tens of kilovolts are used in order to reduce Doppler broadening to the same magnitude as the natural line-width.

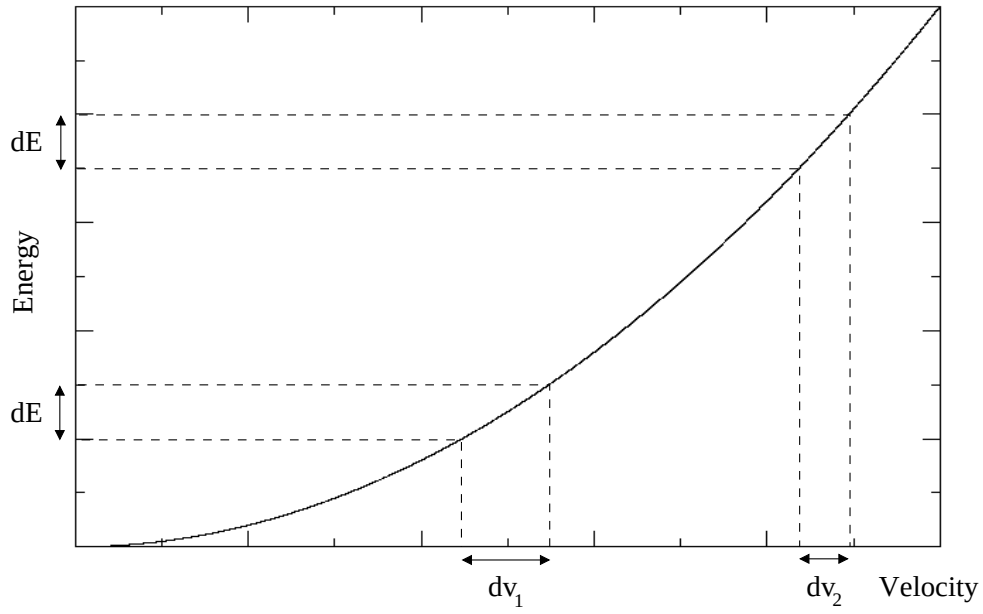

Figure 3.4: Reduction in velocity distribution of ion beam as beam velocity is increased.

As well as significantly reducing Doppler-broadening, the collinear method is advantageous as it is very efficient and hence can be used to study very small samples of ions. A high percentage of the ions in the beam are steered to the light collection region and are therefore able to produce detectable fluorescent photons. This enables successful measurements to be made for even short lived radioactive isotopes (which can only be produced in small quantities). The disadvantage of the collinear laser spectroscopy method is its complexity. Long beam lines with high-voltage acceleration regions and substantial vacuum systems are required and so collinear lines are usually built at large radioactive beam facilities such as the IGISOL at the University of Jyväskylä, and ISOLDE at CERN. As a result, collinear experiments are often time consuming and expensive to operate.

Chapter 4

Experimental Equipment and Techniques

The experimental work conducted for this thesis utilised crossed-beam laser spectroscopy in order to reduce the Doppler broadening of the measured spectral lines. As outlined earlier in chapter 3, crossed-beam laser spectroscopy overlaps a laser beam at right-angles to an atomic beam. The experiment used during this work overlapped a horizontal laser beam with a vertical beam of atoms in order to achieve this geometry. This chapter will discuss this experimental setup in detail.

4.1 The Dye Laser

The tuneable laser used during this work was a Spectra Physics 380 Ring Dye Laser. A dye laser is an ideal tool for use in spectroscopy due to its ability to produce narrow bandwidth beams across a wide range of wavelengths. This enables a large number of atomic transitions to be studied. A laser has three main components; an active medium which produces and amplifies the laser photons, a pump mechanism that puts energy into the active medium and creates the population inversion required to produce amplification and finally a resonator cavity to reflect the generated laser photons back to the active medium for amplification [24]. Each of these components plays an important role in the output wavelength of the Spectra Physics 380 dye laser.

4.1.1 The active medium

In a dye laser, the active medium is a liquid of organic dye molecules dissolved in a solvent. The complex dye molecules possess a large number of rotational and vibrational energy states that broaden each electronic energy level into continuous bands (see figure 4.1). A diode-pumped solid state (DPSS) laser is used to optically pump an electron from the lower energy band (S0) to the upper energy band (S1). Once in the upper band the electron rapidly relaxes to the bottom of the band via non-radiative phonon interactions due to collisions between the dye and solvent molecules. The electron may then relax to any of the rotational/vibrational states that make up the lower energy band (S0), by spontaneously emitting a photon. The continuous band of lower energy states enables a large number of photon wavelengths to be produced. The lifetime of the intraband phonon relaxation process is of the order of 10^{-12}s. This is significantly shorter than the lifetimes of the radiative transitions between bands which is of the order of 10^{-9}s [24]. This results in electrons rapidly relaxing and accumulating at the bottom of the upper state (S1) and producing the population inversion required for laser action.

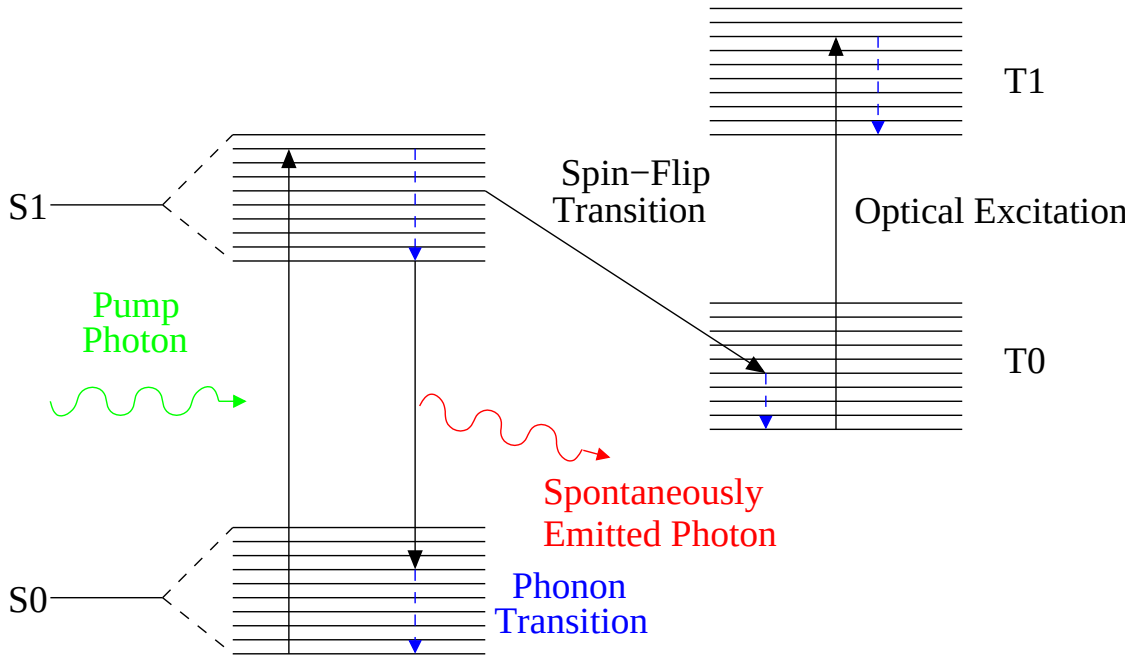

Figure 4.1: Dye molecule energy level scheme. The electronic energy levels are split into vibrational and rotational bands of levels

It is also possible for an electron in the upper singlet state (S1) to relax to a state in the lower energy triplet band (T0). This transition requires a spin-flip of the electron and such a transition between a singlet state and a triplet state is much less likely than a transition between two singlet (or two triplet) states. The lifetime for the relaxation of the

triplet state to singlet ground state is long as this transition would also require an electron spin-flip. Electrons inhabiting the lower triplet band are readily able to absorb energy via excitation to higher triplet bands (T1). The longer a dye laser operates the more electrons pass into triplet states reducing the number available to produce photons, and the more electrons in triplet states the more laser energy that is lost via triplet excitations. These two factors reduce the laser gain. This problem is removed by using a jet of circulating dye inside the cavity. The time taken for the dye to circulate around the dye circulatory system and back to the pumping location is longer than the lifetime of the spin transitions from the triplet band to the singlet ground state. This ensures that the triplet states remain sparsely populated.

4.1.2 The pump beam and laser cavity

Figure 4.2 below displays a schematic of the Spectra Physics 380 dye laser cavity. The pump beam is provided by a *Millenia Pro 6sJ* Neodymium Yttrium Vanadate (Nd:YVO4) solid state laser capable of producing up to 6W of laser power with a wavelength of 532nm. The pump beam is vertically polarised however the dye laser only supports horizontally polarised beams. To overcome this discrepancy the pump beam passes through a polarisation rotator when entering the dye laser cavity which rotates the pump beam polarisation by 90 degrees. It is then directed onto the dye jet by the pump mirror. As described above, the optically pumped dye produces photons with a range of different wavelengths. Some of these photons are directed around the cavity and back to the dye jet by four mirrors set up in a figure-of-eight configuration. The returning photons generate more photons by stimulated emission and hence instigate laser action.

In a conventional resonator cavity the laser beam produced forms a standing wave with longitudinal modes separated in frequency by,

$$d\nu = \frac{c}{2L}, \tag{4.1}$$

where L is the length of the cavity. This condition follows as a result of the cavity's ability to only support laser modes with an integer number of half-wavelengths inside the cavity. Standing waves exhibit maxima and minima that remain at fixed locations around the cavity. This results in only those parts of the dye jet that coincide with the position of a wave maximum being stimulated by the returning photons. Those regions of

the dye that overlap with wave minima are not stimulated and so maintain a sufficiently high enough level of gain to stimulate lasing at other cavity modes. This effect is known as spatial hole burning and destroys the single-mode single-frequency nature of the laser output beam.

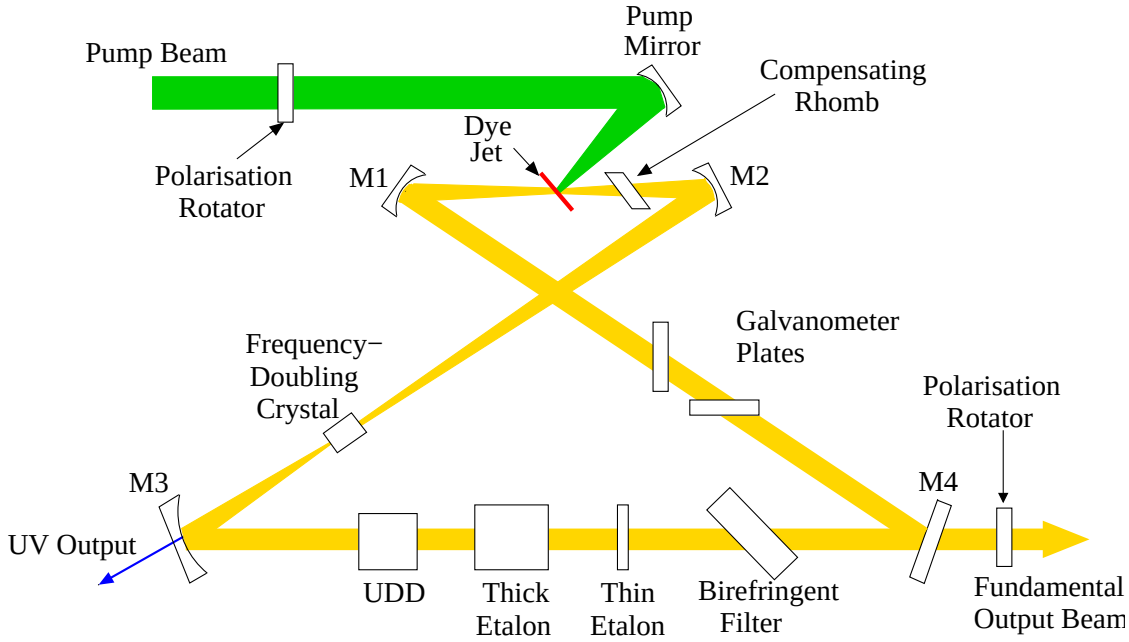

Figure 4.2: Schematic diagram of the Spectra Physics 380 ring dye laser cavity.

The figure-of-eight configuration of the Spectra Physics 380 cavity produces travelling waves instead which possess modes with the following frequency separation,

$$d\nu = \frac{c}{L}. \tag{4.2}$$

These travelling wave modes propagate continuously around the cavity ensuring that all of the dye is utilised by a single cavity mode. This removes the spatial hole burning effect. However, the travelling waves produced are free to propagate around the cavity in both directions. This is unfavourable as only half of the cavity power is travelling in the desired direction. A unidirectional device (UDD) is used to ensure single-direction operation. The light travelling inside the cavity is horizontally polarised. The UDD consists of a Faraday rotator and a quartz plate that combine to produce a net polarisation rotation of a few degrees to the travelling wave propagating in the undesired direction around the cavity. Multiple circuits of the cavity lead to a large net rotation of the polarisation of the undesired beam direction. A number of the components inside the cavity are positioned at Brewster's angle relative to the beam causing the rotated beam

to suffer losses as it propagates around the cavity and rapidly preventing laser operation. The travelling wave propagating in the desired direction receives no net polarisation rotation as the rotation produced by the quartz plate and Faraday rotator are of near equal magnitude but act in opposite direction. Consequently the desired beam propagates without loss.

The galvanometer plates enable the output frequency of the laser beam to be scanned. They consist of quartz plates on galvanometer mounts which rotate when a current is applied. Rotating the plates in opposite directions changes the optical path length of the cavity without changing the path of the beam. From equation 4.2 varying the path length, L, causes the frequency separation of the laser modes to change therefore enabling the frequency of the laser beam to be tuned continuously.

4.1.3 Frequency Selection

The laser cavity can support a large number of laser modes with a frequency separation of $\simeq$230MHz. Single mode operation is achieved by aligning the transmission profiles of the thick and thin etalons and the birefringent filter with a chosen laser mode. An etalon consists of two parallel partially-reflecting surfaces separated by a distance, d. Constructive and destructive interference occurs inside an etalon as an incident beam is reflected between its two surfaces. The transmission profile of an etalon therefore consists of regularly spaced interference maxima. The frequency separation of two transmission maxima is known as the free-spectral range (FSR) of the etalon and can be calculated from the etalon mirror separation as follows,

$$FSR = \delta\nu = \frac{c}{2dn}, \tag{4.3}$$

where n is the refractive index of the medium inside the etalon. The width of the transmission peaks is related to the property of an etalon known as the finesse, F,

$$F = \frac{\pi}{2}\sqrt{\frac{4R}{(1-R^2)}}, \tag{4.4}$$

where R is the reflectivity of the etalon mirrors. The higher the reflectivity of the mirrors the larger the finesse of the etalon and the narrower the etalon transmission peaks. Figure 4.3 displays the transmission profiles of etalons with different mirror reflectivities, R.

For large values of R the full-width-half-maximum, $FWHM$, of an etalon transmission profile is [24],

$$FWHM = \frac{4}{\sqrt{4R/(1-R^2)}}. \tag{4.5}$$

The thick etalon in the Spectra Physics 380 cavity consists of two glass plates separated to create an FSR of 75GHz. The glass plates are mounted in a temperature controlled housing (to limit the effect of thermal fluctuations upon the plate separation) with one of the plates positioned upon a piezoelectric mount. This allows the plate separation d, and hence the FSR, of the etalon to be changed in order to track a single laser cavity mode when the laser frequency is scanned (see section 4.3.4). The thin etalon consists of a 0.1mm thick glass plate and has an FSR of 900GHz. Both etalons have relatively low finesse. Only cavity modes that occur at frequencies where the transmission maxima in both etalon transmission profiles overlap will be able to propagate around the cavity. This severely limits the number of modes that are supported by the cavity.

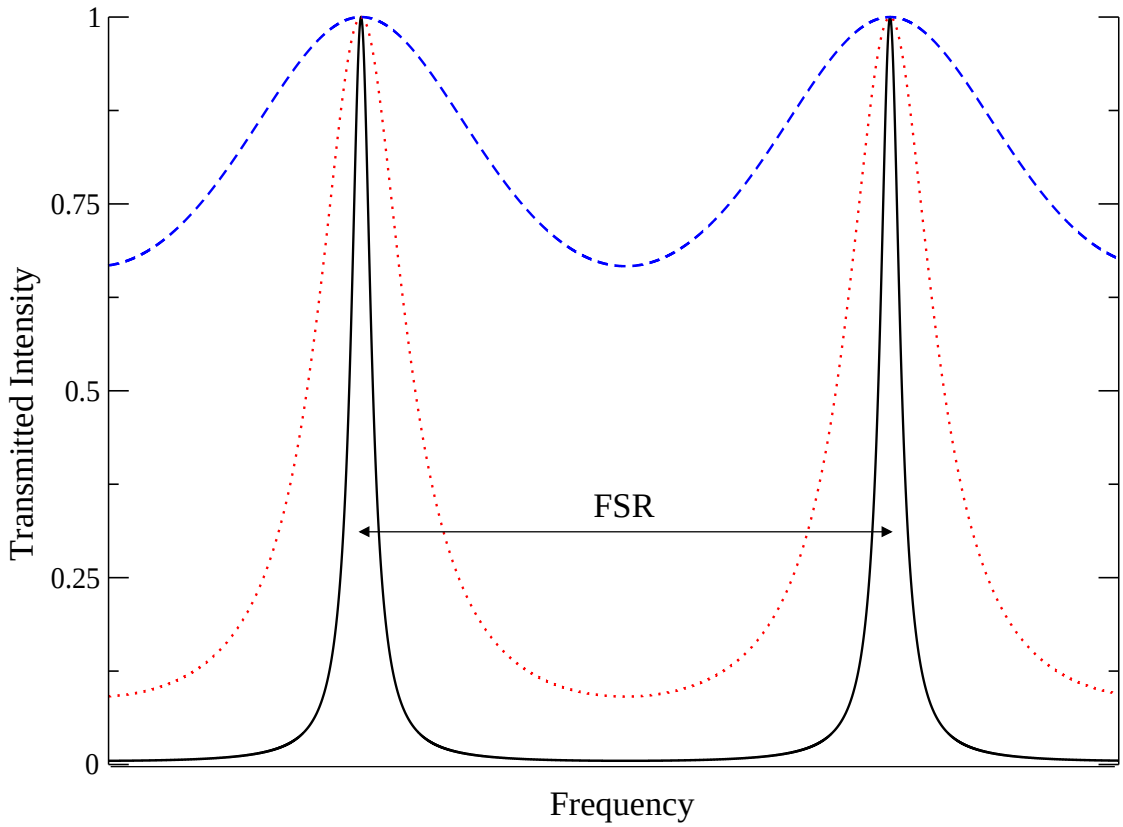

Figure 4.3: Transmittance of an etalon with mirror reflectivity of 0.1 (blue, dashed), 0.55 (red, dotted) and 0.9 (black, solid).

Further mode selection is provided by the broad transmission profile of the birefringent filter. The birefringent filter consists of up to three quartz plates positioned at

Brewster's angle to the laser beam. Only certain wavelengths are able to pass through the filter without suffering a net polarisation rotation and hence losses at the Brewster surfaces. Figure 4.4 illustrates how the transmission profiles of the various cavity components align to select a single cavity mode. The mode selected can be coarsely tuned by the user by rotating the birefringent crystal about the beam axis. This shifts the wavelength at which the peak in the birefringent filter's intensity profile occurs and changes the laser wavelength.

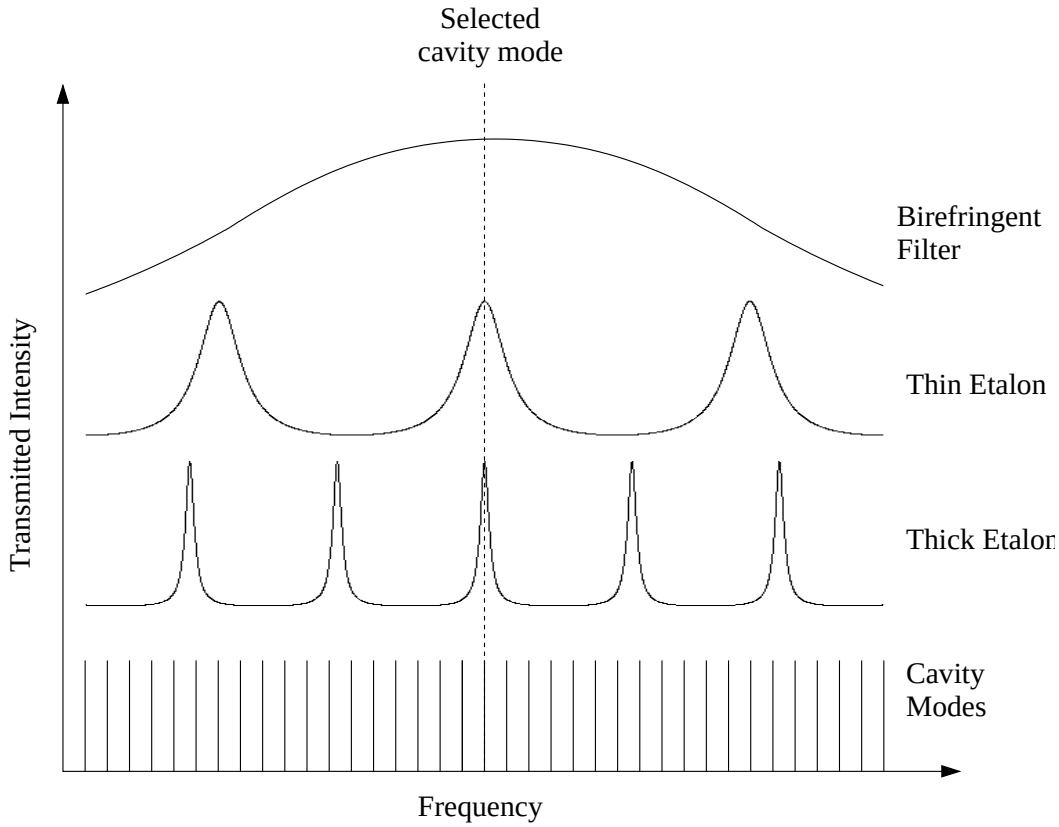

Figure 4.4: Schematic diagram of the transmission profiles of the mode selection components of the dye laser cavity (not to scale).

4.1.4 Laser Wavelength Range

The operational wavelength range of the dye laser cavity is dependent upon three components: the type of dye, the wavelength of the pump laser and the reflectivity of the cavity components and mirrors. Primarily the type of dye molecule restricts the range of output wavelengths that can be produced by the laser. Different dye types have different molecular structures and therefore absorb and emit light over different wavelength ranges. Figure 4.5 displays the absorption and emission spectrum for a typical dye molecule. A typical dye will allow laser operation over a range of approximately 50 – 70nm. For all

dyes the emission profile peaks at longer wavelengths than the absorption profile. The reason for the offset between peak absorption and emission wavelength can be appreciated from figure 4.1. The range of absorbed photon energies will be mostly larger than the range of photon emission energies due to the rapid non-radiative relaxation lifetime of the upper band. This directly leads to the observed offset in peak wavelengths. Figure 4.5 also displays the absorption profile of triplet states. As discussed above in section 4.1.1, the triplet state absorption profile overlaps the dye emission profile and can lead to a drop in photon production efficiency.

In principle a dye laser can produce an output of any wavelength provided an appropriate dye can be found. However the choice of laser dye is restricted by the fixed wavelength of the available pump laser beam. The Nd:YVO_4 pump laser used for this experiment has a wavelength of 532nm and therefore only dyes which absorb strongly at this wavelength could be used during this experiment.

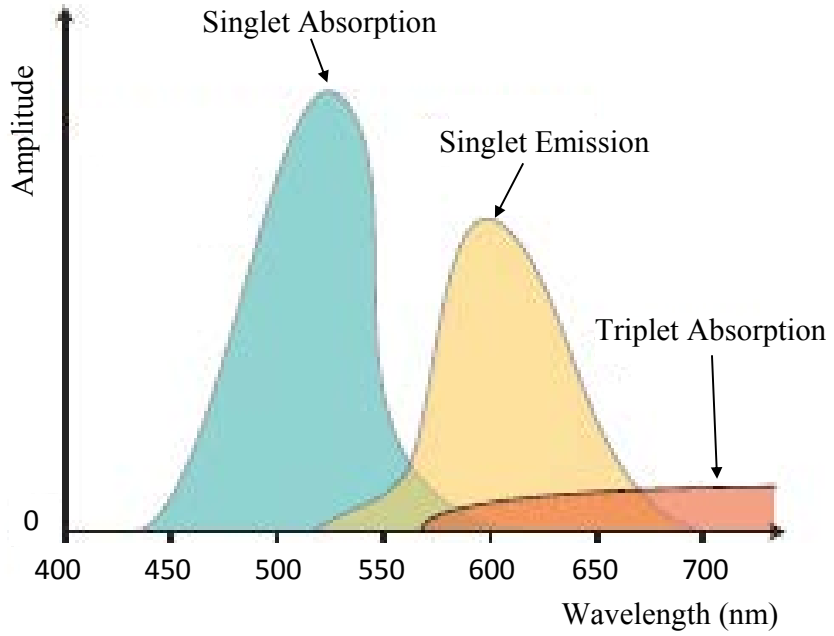

Figure 4.5: The absorption and emission profiles of a typical dye molecule (reproduced from the Ph. D. thesis of M. D. Gardener[27]).

Finally, the photons emitted from the dye must be redirected to the jet by the cavity mirrors for lasing to occur. The cavity mirrors used in this work use multi-layer dielectric coatings to produce high levels of reflectivity over wavelength ranges of approximately 50 – 100nm (depending upon the particular mirror and wavelength). Outside of these wavelength ranges the mirrors rapidly become transparent to the laser beam. Table 4.1 displays the various laser dyes that were used during this work along with both the range

of absorption and the range of emission wavelengths associated with each dye molecule.

Dye	Minimum wavelength (nm)	Maximum wavelength (nm)	Peak Emission wavelength (nm)
Rhodamine 6G	560	650	590
Rhodamine B*	605	675	640
Sulforhodamine 101	636	675	655
Pyridine 1	670	780	710
Pyridine 2	685	820	720

Table 4.1: Emission wavelength properties[28] for dyes used during this work. *Rhodamine B was not used by the author but was used previously to obtain transitions by E. Cochrane.

4.1.5 Second Harmonic Generation

The majority of transitions from the atomic ground state multiplet of ruthenium have wavelengths in the 200-400nm range. These wavelengths can be produced by utilising the frequency-doubling properties of non-linear crystals. A beta-barium borate (β-BBO) frequency doubling crystal is positioned at the auxiliary beam waist in the dye laser cavity between mirrors M2 and M3. When tilted to the correct matching angle (to ensure that the path length of the fundamental and frequency-doubled beams match up inside the crystal[29]) a beam of UV photons is produced which travels towards M3. M3 has a dielectric coating that is highly reflective for the wavelength of the fundamental beam but transparent for UV wavelengths. The UV beam therefore exits the cavity through M3 and is then steered and focused through a series of mirrors and lenses into the region where it interacts with the atomic beam.

4.2 The Atomic Beam Unit

Figure 4.6 displays a diagram of the atomic beam unit (ABU) used to produce collimated atomic beams during this work. The ABU consists of a central cylindrical vessel made up of either two or three chambers of equal height, with two arms extending perpendicularly from the upper chamber. At the base of the bottom chamber is positioned a small tantalum oven which is used to produce the atomic beam. The oven consists of a tube of tantalum approximately 1mm in diameter and 5cm in length. A sample

of ruthenium sponge was positioned inside the oven and resistively heated by passing a current of approximately 70 – 80A between the oven's arms and base. As the oven heats up the sample placed within it melts and evaporates producing a dense plume of atoms that travels upwards through the beam unit. The ABU is held at a low pressure of 2×10^{-6}mbar by three diffusion pumps. At this low pressure the mean-free-path of the atoms travelling up through the unit is significantly larger than the size of the unit itself. This ensures that the atoms travel from the oven to the top of the unit without colliding with any air molecules and therefore maintain the velocity vector that they obtain from the oven. The laser beam enters the ABU along the horizontal arms and crosses the atomic beam perpendicularly at the centre of the top chamber. The three chamber system provides a greater distance between the mouth of the oven and the collimation slits in the top chamber. Increasing this distance provides improved angular collimation and hence reduces the magnitude of Doppler broadening as described in section 3.2.1. The two chamber system does not have the same level of angular collimation and therefore has poorer experimental resolution. However more beam atoms reach the interaction point with the laser beam for a two chamber system which increases the experimental efficiency.

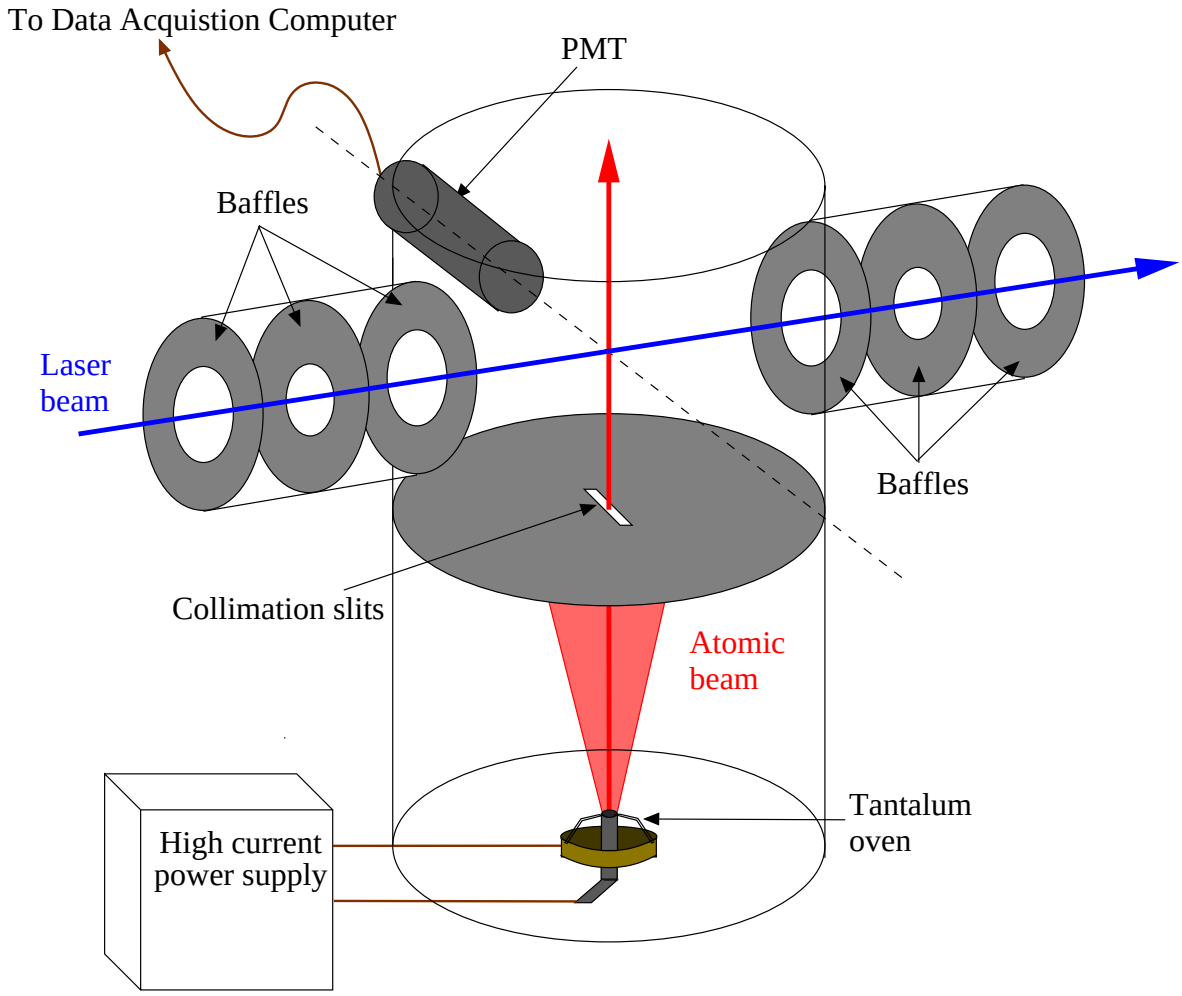

Figure 4.6: Schematic diagram of the Atomic Beam Unit

4.2.1 Producing the Atomic Beam

The narrow bore of the tantalum oven ensures that the velocity vectors of the atoms emerging from the oven are predominantly orientated up through the unit. However a significant portion of the plume of atoms emitted from the oven will still possess a velocity component in the direction of the laser beam. Provided that the oven is vertically aligned the atomic horizontal velocity distribution will be symmetric about zero so that a measured resonance will be symmetrically Doppler broadened. This Doppler width can be significantly reduced by positioning apertures along the axis of the atomic beam. The apertures cut out the atoms with large horizontal velocity components and hence reduce the velocity spread of the atomic beam.

Careful oven alignment is imperative. If the oven is offset then a significant proportion of the atomic beam will be blocked by the apertures and not reach the interaction

region. This will significantly reduce the number of atoms available to interact with the laser beam and produce resonant photons, resulting in a decreased experimental efficiency. It is also important to ensure that the oven is vertical. If the oven is tilted slightly then the atoms will receive a horizontal velocity component directed with the tilt of the oven. This will lead to asymmetric resonances due to Doppler shift of the resonances observed by the atoms.

4.2.2 The Light Collection Region

The interaction region, where the laser intersects the atomic beam, is positioned within the light collection region (LCR). The LCR is a black metal box, positioned inside the upper chamber of the ABU, with apertures in its side and base to allow the laser and atomic beams to enter (see figure 4.7). The LCR contains a spherical mirror and a Fresnel lens which are used to collect resonant photons from the interaction region and to direct them towards the photomultiplier tube (PMT). Baffles are positioned along the axis of the PMT to reduce the number of scattered photons entering the PMT which contribute to spectrum background. The aperture in the base of the LCR is enclosed by a pair of adjustable jaws that can be closed and shaped to reduce the velocity spread of the incoming atomic beam. Typically the jaws are positioned in order to produce a rectangular aperture that is $\sim$1mm wide in the direction of the laser beam and $\sim$1cm wide in the direction perpendicular to the laser. This geometry is chosen to reduce the velocity spread (and hence the transition Doppler width) of the atomic beam in the direction of the laser whilst providing a wider atomic beam in the plane perpendicular to it to provide a larger target for the laser. The jaws at the base of the LCR also provide the important function of reducing the amount of oven glow that is scattered into the PMT. When heated to the temperatures required to produce a beam of ruthenium the oven glows white-hot and is the dominant contributor to spectrum background.

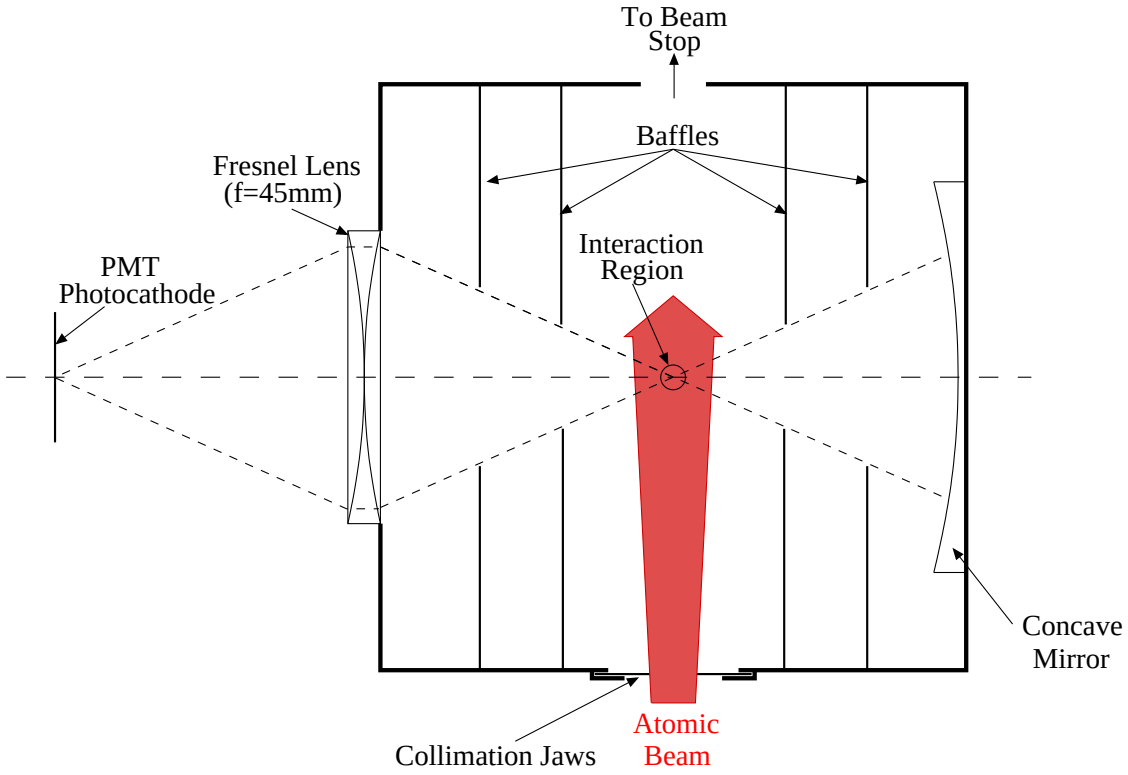

Figure 4.7: The Light Collection Region. The laser is directed out of the page.

4.2.3 Photomultiplier and Data Acquisition System

The photomultiplier tube is positioned with its photocathode facing onto a window looking into the LCR (see figure 4.7). One of two photomultiplier tubes were used during this work each with a peak quantum efficiency at different wavelength regions. The Hamamatsu R1527 tube can measure photons over the 185-680nm range and has peak quantum efficiency of $\simeq$20% for wavelengths in the range 200-400nm. The THORN EMI 9863B/350 tube is sensitive over the wavelength range 300-800nm and has peak quantum efficiency of $\simeq$20% at approximately 430nm. Selection of a PMT is based upon the atomic transition being measured and the wavelength of the range of resonant photons that are produced. A blue-glass, BG-12, filter is positioned between the window and the PMT. The transmission profile of a BG-filter allows 200-400nm light to pass with minimum absorption losses but prevents light outside of this range from entering the PMT. This reduces the scattered oven light detected by the PMT and lowers the experimental background signal.

4.3 The Optical bench

Figure 4.8 displays a schematic of the optical bench and electronics systems used to perform crossed beam laser spectroscopy experiments during this work. The UV beam from the laser is steered through to the atomic beam unit where it interacts with the atomic beam to produce resonant photons. The fundamental beam from the laser is steered and split into a number of components on the optical bench which are used to measure the laser wavelength and maintain its stability. The experimental equipment will be discussed in the following sections according to the roles that each part performs.

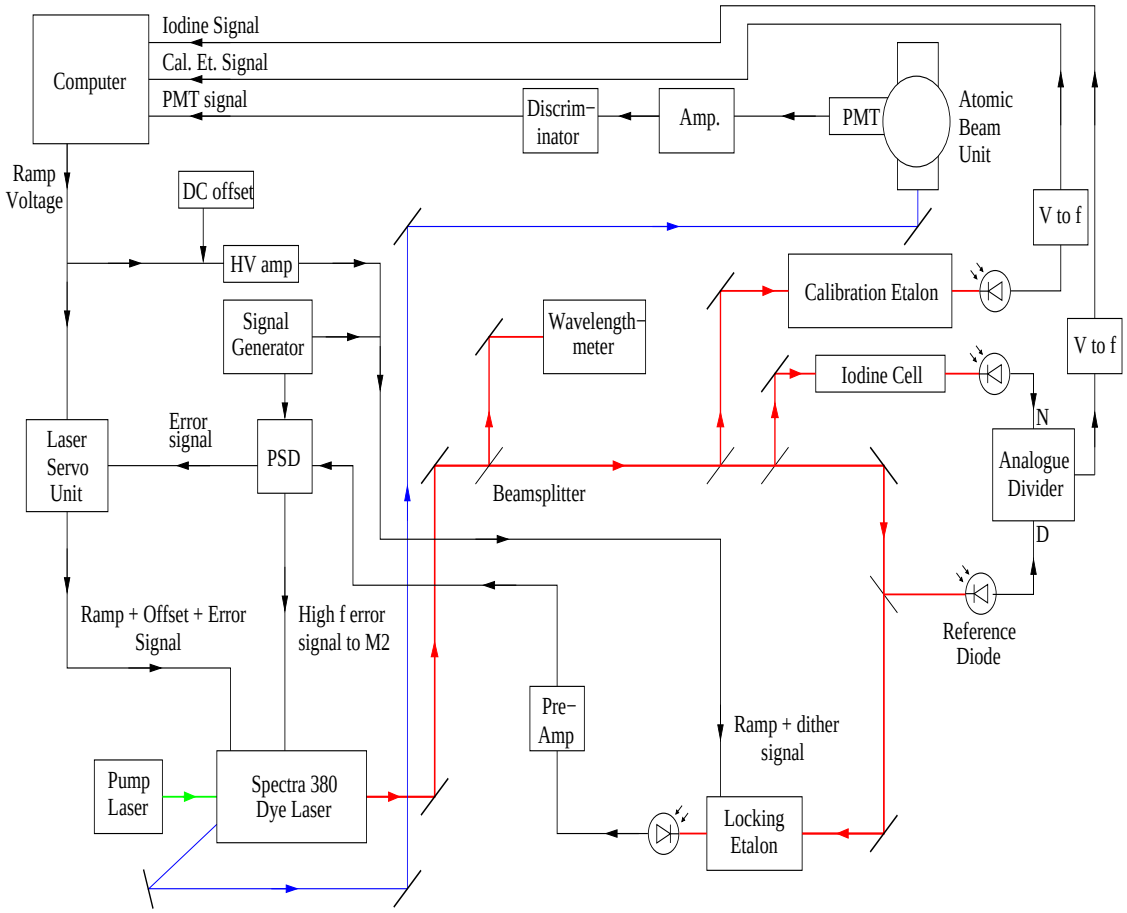

Figure 4.8: Schematic diagram of the optical bench and scanning electronics. Red lines indicate the fundamental laser beam. Blue lines indicate the UV beam. Black lines indicate electronic connections.

4.3.1 Wavelength Selection

In order to perform laser spectroscopy the wavelength of the laser beam must be accurately measured and tuned to the atomic transition wavelength. The exact transition wavelength is achieved in three steps. Firstly a coarse measurement of the laser's wave-

length is achieved using a wavemeter. The wavemeter (see figure 4.9) was designed and built at the University of Birmingham by J. A. R. Griffith and is essentially a Michelson interferometer. The incident dye laser beam is split down the two arms of the wavemeter by the beam splitter at its centre. The optical path length of each arm is varied by a pair of corner-cube reflectors that oscillate in a regular manner. The beams from each arm are then recombined and the interference pattern is monitored on a photodiode. The beam from a helium-neon (He-Ne) laser of a known wavelength is also steered around the wavemeter and its interference pattern is also measured. The wavelength of the dye laser beam is then determined by comparing the interference pattern of the dye laser beam to that of the He-Ne. The wavemeter's accuracy is dependent upon the stability of the He-Ne laser which allows the dye laser wavelength to be measured to the nearest 0.01nm. Unfortunately this level of accuracy is not sufficient to guarantee that the laser is at the atomic transition wavelength.

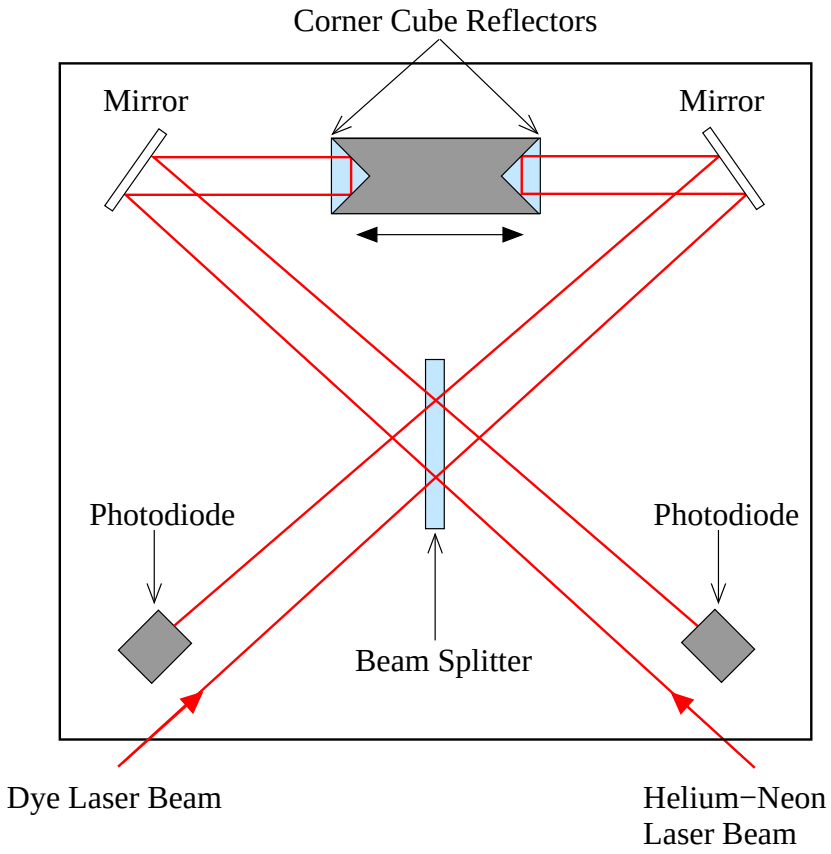

Figure 4.9: Schematic diagram of the wavemeter.

Further tuning of the laser wavelength is achieved by steering a fraction of the dye laser beam through an iodine vapour cell and measuring the absorption spectrum on a

photodiode. The absorption spectrum is observed by scanning the laser over a range of 30GHz and viewing the output of the photodiode using an oscilloscope. The absorption spectrum of molecular iodine is extremely detailed across the majority of the visible spectrum and is also well known and recorded. Comparing the observed absorption spectrum to a published atlas of molecular iodine [30] therefore enables the laser wavelength to be determined to an accuracy of 0.001cm^{-1} which corresponds to 0.00015nm (figure 6.5 in chapter 6 displays an example iodine spectrum from the iodine atlas). The laser is then scanned manually by applying an offset current to the dye laser galvanometer plates and the piezo mount of the thick etalon. The thick etalon must be scanned simultaneously with the galvanometer to ensure that the laser continues to operate in the desired mode. When the laser frequency matches the atomic transition frequency, fluorescent photons are observed on a ratemeter.

4.3.2 Frequency stabilisation

As described in section 4.1.2, scanning the laser frequency is achieved by changing the optical path length of the dye laser cavity. However thermal and acoustic fluctuations in the cavity result in the laser frequency jittering (and even mode jumping) during a scan. In order to measure a spectrum accurately the laser frequency must be scanned in a linear manner and without jitter. The laser frequency is stabilised by electronically locking the laser frequency to a transmission peak of the "locking" etalon positioned on the optical bench.

The "locking" etalon used during this work was a temperature controlled Tropel T240 confocal etalon. A confocal etalon consists of two spherical mirrors facing each other with radius of curvature equal to their separation distance, d (see figure 4.10). Confocal etalons are significantly easier to align than plane surface etalons due to the focusing effect of the curved surfaces. For an incident beam that enters a confocal etalon above or below the central axis the light travels the length of the cavity four times before returning to the entrance point on the first mirror (see figure 4.10). This results in the FSR of a confocal etalon, as expressed in equation 4.6, being half that of a plane etalon with the same mirror separation d (see equation 4.3).

$$FSR = \frac{c}{4nd}, \tag{4.6}$$

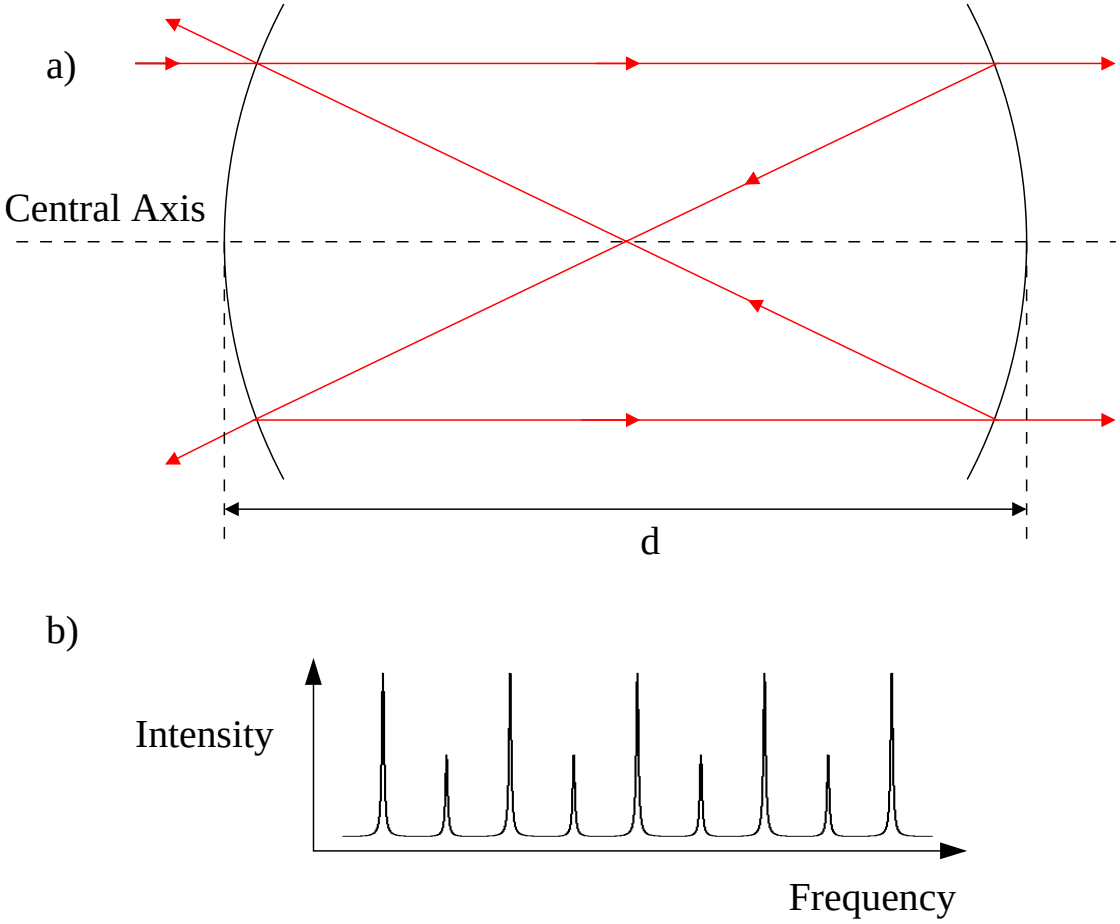

Figure 4.10: a) Diagram of the off-axis optical path through a confocal etalon. b) Transmission profile of a mode-matched confocal etalon.

The locking etalon has a free spectral range of 1.5GHz. However, the FSR of an etalon can drift in time due to two effects. Firstly, fluctuations in temperature and air pressure can lead to the refractive index of the air inside the etalon changing which, by equation 4.6, leads to the FSR changing. Secondly, temperature changes can lead to tiny fluctuations in the cavity length causing the mirror separation d, and hence the FSR, to vary. Passive frequency control mechanisms are employed to reduce the influence of these two effects. Refractive index variations are limited by encasing the etalon inside a temperature controlled vessel that also reduces the effect of atmospheric pressure variations. The effects of thermal length variations are combated by constructing the etalon out of materials, such as INVAR, that possess a low thermal expansion coefficient.

A portion of the fundamental output beam is steered though the locking etalon and its transmission profile is monitored via a photodiode. A 56.4kHz and 2V amplitude dither signal is generated by a programmable function generator and sent to a mirror of the locking etalon that is mounted upon a piezoelectric motor. The dither voltage changes the

etalon mirror separation distance and hence the FSR of the locking etalon from equation 4.6. As the FSR of the etalon is dithered the intensity of the light transmitted through the etalon will also oscillate, with frequency ν_{tran}, in a manner that is characterised by the difference between the laser frequency and the peak transmission frequency of an adjacent etalon mode. This effect is illustrated in figure 4.11.

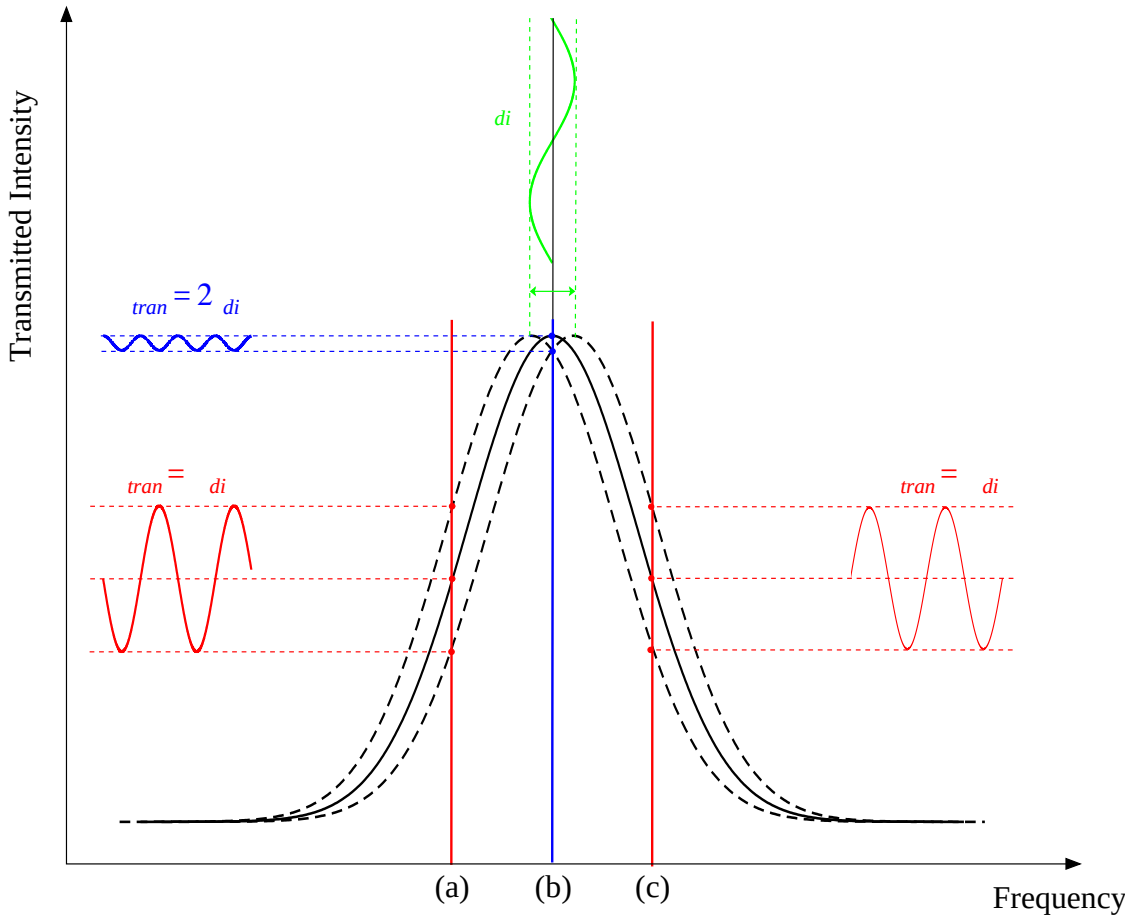

Figure 4.11: Locking to an etalon transmission peak. The etalon transmission peak is dithered by applied frequency ν_{di} (green trace). The horizontal travelling waveforms indicate the observed transmitted wave ν_{tran} when the laser frequency is a) lower than (red trace on left side of diagram), b) equal to (blue trace) or c) greater than (red trace on right side of diagram) the etalon peak transmission frequency .

If the laser frequency is slightly lower (as illustrated by the red vertical line labelled (a) in figure 4.11) or higher than the transmission frequency of the etalon (as illustrated by the red vertical line labelled (c) in figure 4.11) then as the etalon is dithered at frequency ν_{di} the transmitted intensity will vary with the same frequency ($\nu_{tran} = \nu_{di}$). The relative phase difference between ν_{di} and ν_{tran} indicates whether the laser frequency is higher or lower than the actual transmission peak frequency. If the laser frequency is the

same as the etalon transmission frequency (as illustrated by the blue vertical line in figure 4.11) then the transmitted intensity will oscillate at twice the dither frequency (ν_{tran} = $2\nu_{di}$). This provides a direct means of monitoring the laser frequency during operation. A phase sensitive detector (PSD) is used to compare the oscillation frequencies ν_{tran} and ν_{di} and is used to generate an appropriate error signal to return the laser frequency to the peak etalon transmission frequency.

The error signal is then sent to a servo which generates both a low and high frequency output. The low frequency output amends the current sent to the galvanometer plates and thick etalon in the dye laser cavity and can compensate for noise with a frequency less than 100Hz. For noise of higher frequency than this the galvanometer plates cannot be moved quickly enough. The high frequency servo output is thus sent to a piezoelectric mount on mirror M2 in the dye laser cavity which makes subtle changes to its optical path length.

Overall, the locking etalon enables the laser frequency to be kept within 1MHz of the desired laser frequency as it is scanned.

4.3.3 Frequency calibration

The data acquisition system measures the number of fluorescent photons as a function of the ramp voltage applied to scan the laser wavelength. In order to convert the applied ramp voltage into the generated change in laser frequency the output profile of the calibration etalon is measured. The calibration etalon is a confocal etalon with an accurately known FSR of 299.63(1)MHz. A portion of the fundamental beam of the dye laser is directed through the calibration etalon onto a photodiode to monitor its intensity (see figure 4.8). During a spectrum scan, the intensity profile of the calibration etalon is measured in conjunction with the resonant photons produced inside the ABU. The intensity profile forms a frequency ruler with markers separated in frequency space by the FSR of the calibration etalon. The frequency spacing of atomic spectrum lines can then be determined by comparing the atomic spectrum to the frequency markers in the calibration etalon spectrum. The calibration process is discussed further in chapter 5.

The calibration etalon is carefully aligned so that the incident laser beam is nearly steered along its central axis (see figure 4.10a). For this geometry a confocal etalon closely resembles a plane surface etalon and the confocal modes are suppressed. This

results in a distinctive transmission profile (see figure 4.10b) where every-other etalon peak has a lower intensity than the adjacent peaks. This arrangement is known as mode-matching and provides a useful means of identifying specific calibration etalon peaks to determine whether the laser frequency has jumped during a scan.

4.3.4 Scanning the Laser Frequency

In order to perform accurate measurements of atomic transition spectra it is necessary to scan the fundamental laser frequency over a range of a few GHz in a stable manner. Laser frequency scanning is achieved via a linear ramp signal generated by the data acquisition computer. An offset voltage is sent from the computer to the laser servo unit which adjusts the position of the galvanometer plates. After a user specified dwell time, the computer then increases the magnitude of the offset voltage by a user specified step size which adjusts the galvanometer plates (and thick etalon) again. This process is repeated until the galvanometer plates have rotated by the amount required to achieve the maximum desired change in laser frequency. As the frequency of the cavity mode changes, its position relative to the transmission peak of the cavity thick etalon also changes (see figure 4.4). Eventually the desired laser mode is no longer the closest laser mode to the transmission peak of the thick etalon. This can cause the laser to hop frequency to a new laser mode that is approaching the transmission peak of the etalon. These mode-hops are avoided by sending a portion of the ramp signal to a piezo-mounted mirror inside the thick etalon. This adjusts the FSR of the thick etalon so that its transmission peaks change in frequency at the same rate as the desired laser mode.

Laser stability is maintained during a scan by locking the frequency of the laser to the transmission peak of the locking etalon as described in section 4.3.2. When scanning the laser, the ramp signal is also sent to the piezo-mount of one of the mirrors inside the locking etalon in order to shift its transmission peak at the same rate as the laser frequency. If the locking etalon was not scanned simultaneously, as the laser frequency is scanned it would move away from the transmission peak of the etalon and generate an error signal. This signal would be sent to the laser and drag its frequency back towards the etalon transmission peak. The frequency of the locking etalon peak determines the start frequency of the scan. Ideally the laser start frequency should be close to the atomic transition frequency so that the entire spectrum can be measured without resorting to

long scans. An offset voltage can be applied to the piezo-mounted mirror of the locking etalon so that the position of the locking etalon peaks can be shifted to achieve the best locking position.

Figure 4.12 displays an example of the data obtained from the data acquisition system during a laser scan of atomic ruthenium. The photomultiplier signal passes through an amplifier and discriminator prior to entering the data acquisition computer. A National Instruments 6602 Counter/Timer card is used to count the number of detected fluorescent photons. The iodine absorption and calibration etalon spectra are obtained by the output of photodiodes passed through voltage-to-frequency converters and fed into separate inputs of the counter/timer card.

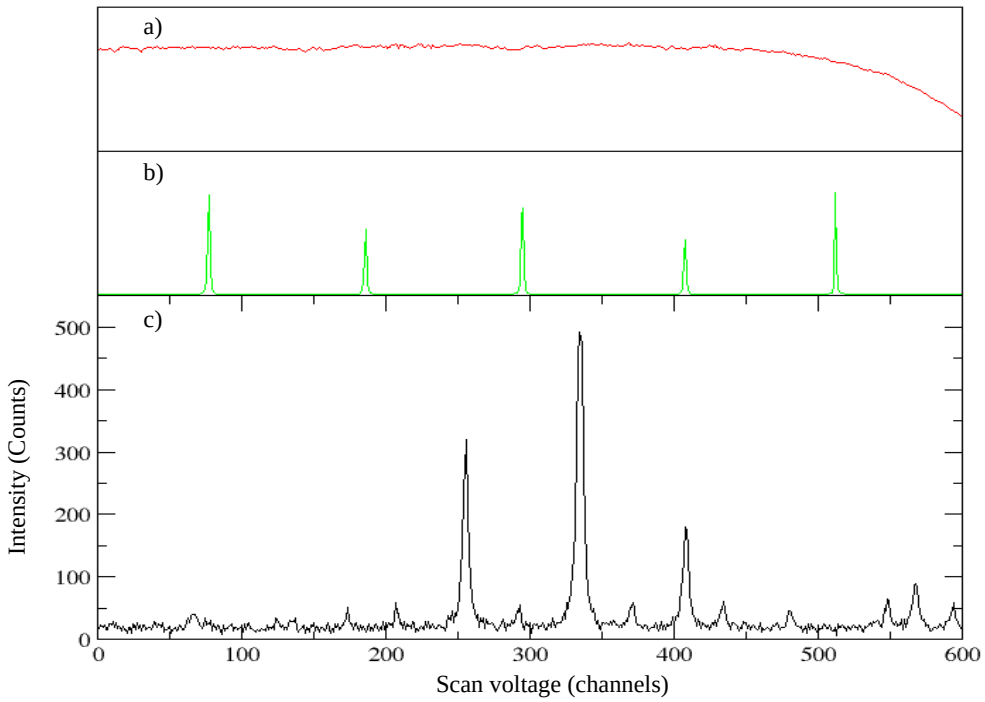

Figure 4.12: Example spectrum of the 329.4112nm transition in ruthenium. a) The iodine absorption profile. b) The calibration etalon transmission profile. c) The atomic fluorescent spectrum.

4.4 Laser Spectroscopy of Ruthenium

4.4.1 Choice of atomic transition

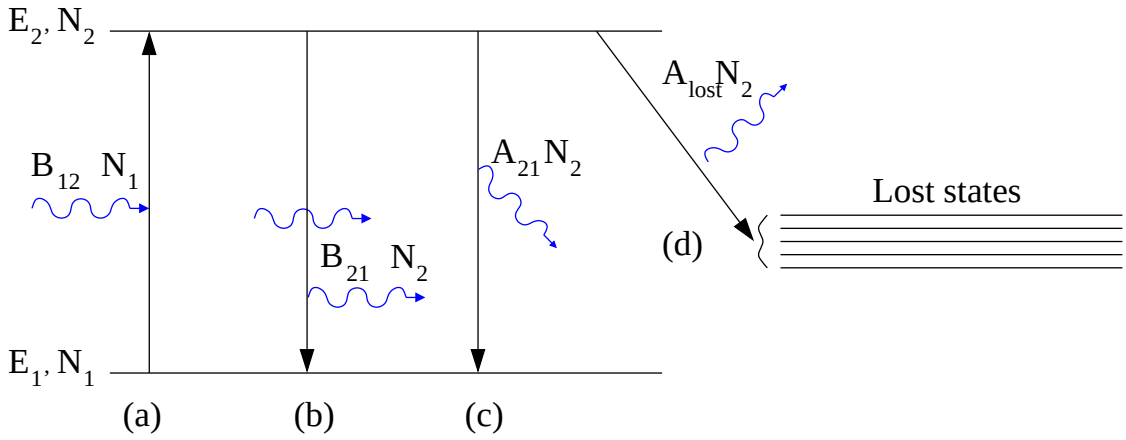

Figure 4.13: Optical transitions between two energy levels. a) Stimulated absorption. b) Stimulated emission. c) Spontaneous emission of a photon by returning to the transition lower state. d) Spontaneous emission to a state other than the transition ground state (a lost state).

A successful transition measurement is dependent upon producing a large enough number of resonant photons for efficient detection by the photomultiplier tube via the reflection optics inside the light collection region. Figure 4.13 displays the optical processes that occur when a laser beam of energy density, ρ, is directed at an atom. An electron in the lower state, E_1, will absorb an incoming photon and become excited to the upper energy level, E_2. This process is called stimulated absorption (see figure 4.13a) and the probability that it will occur, P_{abs} is calculated as follows,

$$P_{abs} = B_{12}\rho, \tag{4.7}$$

where B_{12} is the Einstein coefficient for stimulated absorption. The presence of the laser beam may also cause an electron in state E_2 to relax to the lower state by emitting a photon. This processes is known as stimulated emission (see figure 4.13b) and results in the emission of a photon that is identical to the original photon. The probability that stimulated emission will occur, P_{stim} is calculated as follows,

$$P_{stim} = B_{21}\rho, \tag{4.8}$$

where B_{21} is the Einstein coefficient for stimulated emission. An electron in state E_2 may also relax to a lower energy level in the absence of any incoming photons. This

process is known as spontaneous emission and the probability that an electron will spontaneously return to state E_1 is,

$$P_{spon} = A_{21}, \tag{4.9}$$

where A_{21} is the Einstein spontaneous emission coefficient. Unlike the stimulated emission process, an electron in E_2 may relax by spontaneous emission to any lower energy level allowed by electric dipole (E1) transition rules (see figure 4.13d).

For an E1 transition to occur there must be a change in parity between the upper and lower transition states. For spontaneous emission to be possible from state E_2 to state E_1 and any of the states E_i it must be the case that states E_1 and E_i have the same parity. Therefore once an electron has entered a state E_i it can not return directly to the state E_1 via E1 spontaneous emission. The states E_i will henceforth be referred to as lost states as an electron that relaxes to one of these states is unable to return quickly to E_1 for re-excitation by the laser beam. The atom is therefore lost to the possibility of producing further photons via spontaneous emission.

The probability for a transition occurring from state E_2 to any of the states E_i is,

$$P_{lost} = \sum_{i \neq 1} A_{2i}, \tag{4.10}$$

where $\sum_{i\neq 1} A_{2i}$ is the sum of the Einstein spontaneous emission coefficients to each of the individual lost states. If E1 transitions are forbidden it is possible for a lost state to decay via higher order radiation such as magnetic dipole (M1) and electric quadrupole (E2) transitions. However the spontaneous emission transition probabilities of these higher order transitions are considerably lower than E1 with $A_{M1}/A_{E1} \simeq 10^{-5}$ and $A_{E2}/A_{E1} \simeq 10^{-6}$[31]. It is highly unlikely that such a transition will occur during the interaction time between the laser and atom and so the effect of higher order radiation is neglected. Similarly, a lost state could also return to state E_1 via a non-radiative collision transition however the time-scales for such an interaction in an atomic beam are also significantly longer than the transit time of the atom crossing the laser beam. Return to E_1 via this collisional de-excitation is therefore also neglected. From equations 4.7 to 4.10 it is possible to form equations for the time-dependent change in state population due to the presence of a laser beam of energy density ρ,

$$\frac{dN_1}{dt} = A_{21}N_2 + B_{21}\rho N_2 - B_{12}\rho N_1, \tag{4.11}$$

$$\frac{dN_2}{dt} = B_{12}\rho N_1 - B_{21}\rho N_2 - (A_{21} + A_{lost})N_2. \tag{4.12}$$

where N_1 and N_2 are the populations of states E_1 and E_2 respectively. Laser spectroscopy experiments are only sensitive to the detection of photons produced by spontaneous emission. This is because spontaneously emitted photons can be emitted in any direction whereas photons produced by stimulated emission always travel in the direction of the laser beam. Stimulated emission photons can therefore not be detected by the PMT positioned at right-angles to the beam. The rate of spontaneously emitted photons, $\dot{n_\gamma}$, is calculated as follows,

$$\frac{dn_\gamma}{dt} = (A_{21} + \sum_{i \neq 1} A_{2i})N_2. \tag{4.13}$$

From equation 4.13 it is apparent that in order to produce a large number of spontaneously emitted photons it is necessary to:

- choose a strong transition with a large A_{21}-value for its upper state. Upper states which relax to lost states also produce detectable photons however lost state transitions also act to remove atoms from the system. Transitions with a high value of $\sum_i A_{2i}$ therefore have a lower probability of producing multiple photons per atom. The effect of lost state transitions upon the experimental efficiency is of greater importance for collinear laser spectroscopy experiments than crossed-beam work. Collinear experiments tend to utilise low density atomic beams and therefore it is advantageous to excite each atom multiple times.

- effectively populate the transition upper state, N_2. From equation 4.12, the population of the upper state is determined by the transition stimulated absorption rate B_{12} and also the energy density of the laser beam ρ. It can be shown that [24, 31],

$$B_{12} = \frac{g_2}{g_1} B_{21}, \tag{4.14}$$

where g_1 and g_2 are the degeneracies of the lower and upper states and,

$$A_{21} = \frac{8\pi\nu^3 h}{c^3} B_{21}, \tag{4.15}$$

i.e. the stimulated absorption rate is related to the spontaneous emission rate A_{21}. It is therefore still favorable to choose a transition with a high A_{21} value and to optimise laser power to increase ρ. From equation 4.12, it is also important to ensure that the lower state population, N_1, is initially high in order to achieve effective population of the upper state. Table 4.2 displays the percentage population of the energy levels in the ground state multiplet of ruthenium at different thermal temperatures calculated using the Boltzmann distribution. The thermal percentage population of energy levels greater than the 3105cm^{-1} state is effectively negligible which prevents laser spectroscopy being performed from these levels.

	Oven Temperature (K)					
E (cm^{-1})	1500	1750	2000	2250	2500	2750
0	71.6	66.6	62.4	58.6	55.2	52.1
1190.64	18.7	20.5	21.7	22.4	22.8	22.9
2091.54	6.1	7.6	8.8	9.8	10.5	11.1
2713.24	2.4	3.3	4.0	4.7	5.3	5.7
3105.49	1.0	1.4	1.8	2.2	2.5	2.8

Table 4.2: Boltzmann distribution calculation of the percentage population of the energy levels in the ground state multiplet for various oven temperatures.

4.4.2 Ruthenium transition measurements

Nineteen atomic transitions in ruthenium were measured during this work across a wide range of laser wavelengths. All the transitions measured were from the 0 – 3105.49cm^{-1} ground state multiplet and had strong A-coefficients of $> 10^6$s^{-1}. These were complemented by four transitions measured in 1999 by E. Cochrane on the same experimental set-up at the University of Birmingham. The details for all of these transitions are displayed in table 4.3. The measurement of these transitions will now be discussed in order of the various laser dyes used to record them.

4.4.3 The Rhodamine 6G range

The eleven transitions in the wavelength range 296.5166 – 309.9280nm were measured using the dye Rhodamine-6G (R6G). R6G is a very popular and commonly used dye due

λ (nm)	A (s^{-1})	E_l (cm^{-1})	J_l	Config.	E_u (cm^{-1})	J_u	Config.
296.5166	1.926$\times 10^7$	2091.540	3	$4d^7 5s$	35806.620	3	$4d^6 5s5p$
297.6925	1.109$\times 10^7$	1190.640	4	$4d^7 5s$	34772.550	5	$4d^6 5s5p$
298.8947	1.856$\times 10^7$	0.000	5	$4d^7 5s$	33446.840	4	$4d^6 5s5p$
299.4968	1.040$\times 10^7$	2091.540	3	$4d^7 5s$	35471.150	4	$4d^6 5s5p$
300.6586	2.746$\times 10^7$	2713.240	2	$4d^7 5s$	35963.870	2	$4d^6 5s5p$
301.7235	3.218$\times 10^7$	3105.490	1	$4d^7 5s$	36238.770	1	$4d^6 5s5p$
302.0873	1.118$\times 10^7$	2713.240	2	$4d^7 5s$	35806.620	3	$4d^6 5s5p$
304.0314	3.184$\times 10^6$	1190.640	4	$4d^7 5s$	34072.410	3	$4d^6 5s5p$
304.2478	1.254$\times 10^7$	3105.490	1	$4d^7 5s$	35963.870	2	$4d^6 5s5p$
304.8788	3.521$\times 10^6$	2091.540	3	$4d^7 5s$	34881.920	2	$4d^6 5s5p$
309.9280	1.089$\times 10^7$	1190.640	4	$4d^7 5s$	33446.840	4	$4d^6 5s5p$
315.9929†	5.696$\times 10^6$	2091.540	3	$4d^7 5s$	33728.660	2	$4d^6 5s5p$
318.6043†	7.590$\times 10^6$	2713.240	2	$4d^7 5s$	34091.060	1	$4d^6 5s5p$
318.9979†	2.699$\times 10^6$	2091.540	3	$4d^7 5s$	33430.650	3	$4d^6 5s5p$
319.6605†	2.424$\times 10^7$	3105.490	1	$4d^7 5s$	34379.640	0	$4d^6 5s5p$
329.4112	2.781$\times 10^6$	0.000	5	$4d^7 5s$	30348.450	4	$4d^7 5p$
330.1594	2.786$\times 10^6$	0.000	5	$4d^7 5s$	30279.680	5	$4d^7 5p$
342.8318	1.994$\times 10^7$	0.000	5	$4d^7 5s$	29160.460	6	$4d^6 5s5p$
343.6736	4.900$\times 10^7$	1190.640	4	$4d^7 5s$	30279.680	5	$4d^7 5p$
349.8942	8.955$\times 10^7$	0.000	5	$4d^7 5s$	28571.890	6	$4d^7 5p$
358.9213	8.221$\times 10^7$	3105.490	1	$4d^7 5s$	30958.800	2	$4d^7 5p$
359.3018	7.904$\times 10^7$	2713.240	2	$4d^7 5s$	30537.060	3	$4d^7 5p$
359.6178	4.354$\times 10^7$	2091.540	3	$4d^7 5s$	29890.910	4	$4d^7 5p$

Table 4.3: Measured transitions listed in order of ascending wavelength. † indicates transitions measured in 1999 by E. Cochrane. All transition information was taken from the Kurucz Atomic Database[32]

to its ability to produce a stable fundamental beam with good power over a broad wavelength range[28]. Using a β-BBO frequency doubling crystal, UV laser beams of typically 0.3 – 0.5mW (for 4.5 – 5W pump laser power) were produced to measure the transitions. For all R6G region transitions, very small isotope shifts were observed resulting in very narrow spectra with difficult to resolve structure. The reason for this is due to the configurations of the electrons involved in the transitions. The ground state configuration of ruthenium is $1s^2 2s^2 2p^6 3s^2 3p^6 3d^{10} 4s^2 4p^6 4d^7 5s$. The Kurucz atomic database[32] lists all of the measured R6G transitions as $4d^7 5s$ to $4d^6 5s5p$ type transitions. Transitions involving d-electrons (or indeed any transitions not involving s-electrons) have low field shifts due to the zero (or very small for $p_{\frac{1}{2}}$ electrons) probability of the electron inhabiting the nuclear volume (see section 2.1.2). Figure 4.14 shows a measured spectrum for the 304.8788nm transition in ruthenium. A visual comparison of figures 4.14a and 4.14b shows that nearly the entire atomic spectrum fits within two calibration FSR. This corresponds to a frequency range of $\simeq$1.2GHz.

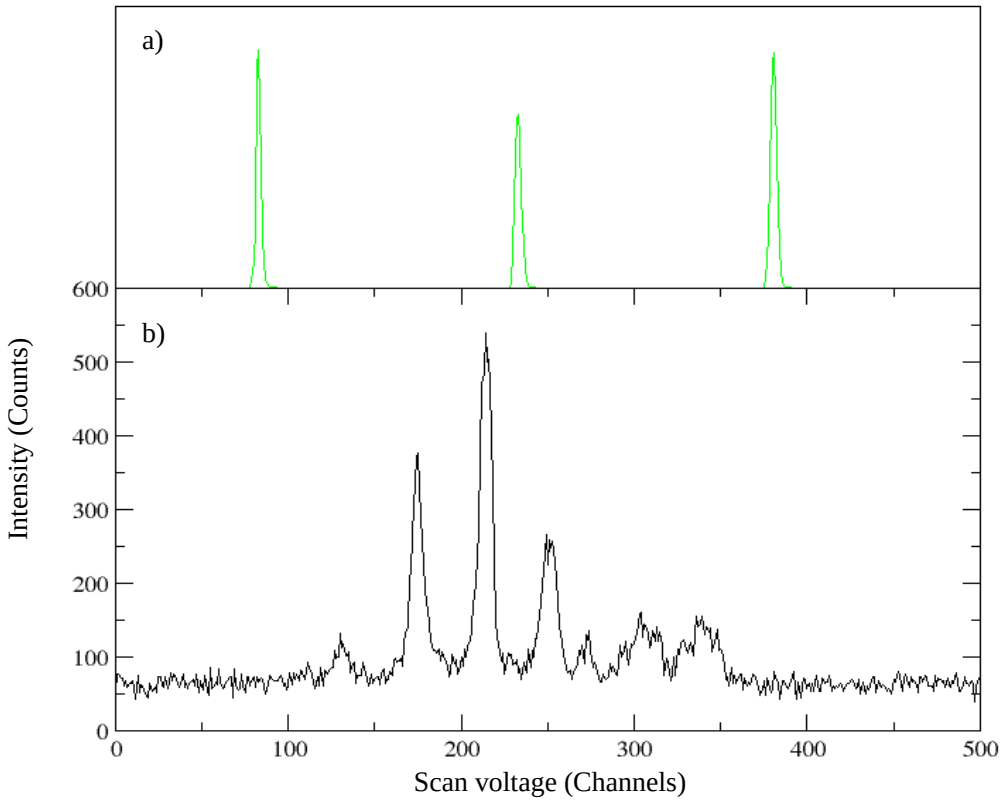

Figure 4.14: Spectrum of the 304.8788nm transition in ruthenium. a) The calibration etalon profile. b) The atomic fluorescent spectrum.

4.4.4 The Sulforhodamine 101 range

Following on from the R6G region, the 329.411nm and 330.159nm transitions were measured using the laser dye Sulforhodamine-101 (SR-101). SR-101 enabled the production of UV beams with a typical power of 0.4mW (for ∼4W pump laser power). These transitions were selected as they are $4d^7 5s$ to $4d^7 5p$ type transitions and were therefore likely to exhibit larger field shifts than those observed in R6G due to the change in the number of s electrons during the transition. Figure 4.15 below displays a spectrum of the 329.4112nm transition. This transition covers a significantly greater frequency range than the R6-G transitions (see figure 4.14) and hence justified the change in laser dye. Generally the ruthenium transitions in the SR-101 region are much weaker than those in R6G. Several transitions, other than the 329.411nm and 330.159nm, were attempted in the SR-101 wavelength range however they could not be experimentally detected. This is most likely due to the low spontaneous emission coefficient resulting in an insufficient number of resonant photons being produced.

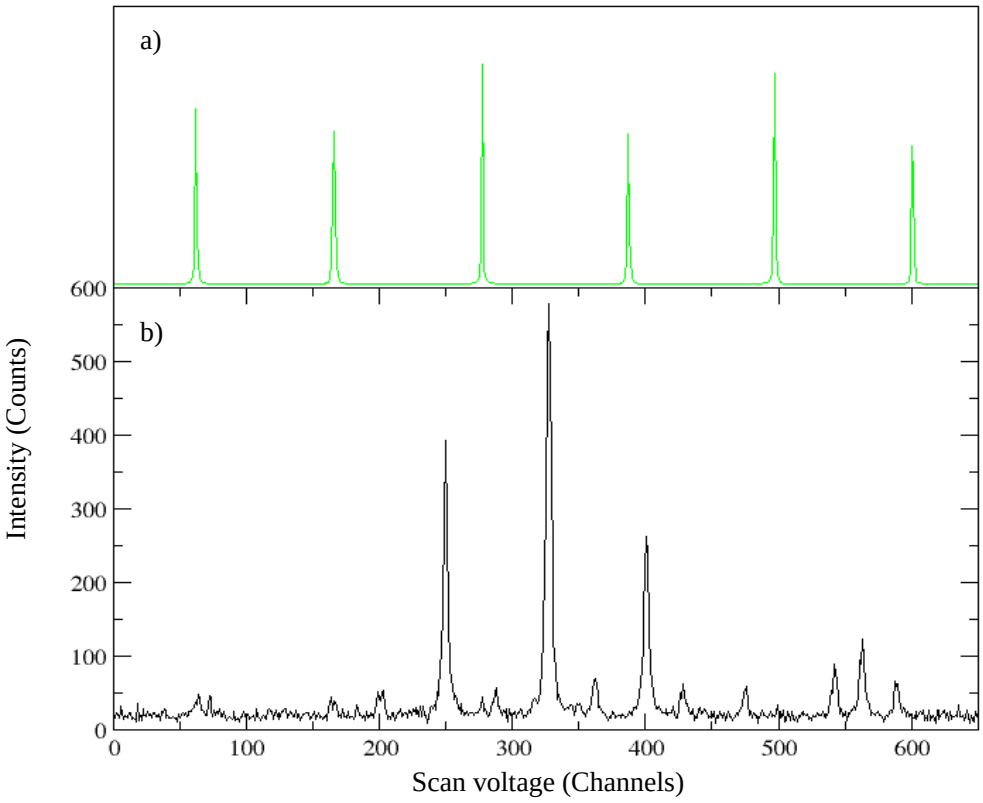

Figure 4.15: Spectrum of the 329.4112nm transition in ruthenium. a) The calibration etalon profile. b) The atomic fluorescent spectrum.

4.4.5 The Pyridine 2 range

The lack of strong measurable transitions in ruthenium in the SR-101 wavelength region prompted another change in dye. Pyridine 2 (P-2) produces a wide range of output wavelengths however its absorption peak is not as well matched to the wavelength of the dye laser pump beam as R6G. To combat this a 4mmol solution (double the regular concentration[28]) of P-2 dye was used and the power of the pump laser beam was increased to 6W to boost the absorption rate of the dye. It was found that P-2 produced very good UV beams with a power $\sim$1 – 1.5mW.

Pyridine-2 was used to successfully measure the six transitions in the wavelength range 342.8318 – 359.6178nm. The majority of these transitions are $4d^7 5s$ to $4d^7 5p$ type transitions and exhibit well-spaced spectra. The measured transitions also have very high A-coefficients which enabled their successful detection. Further high-strength (A-coefficient $>10^7$ s^{-1}), $4d^7 5s$ to $4d^7 5p$ type transitions exist at wavelengths greater than 360nm. These wavelengths can be produced using P-2 however it was observed that for fundamental laser beam wavelengths greater than 700nm the reflection coatings on the mirrors of the locking and calibration etalons became increasingly transparent. As the reflectivity of an etalon decreases, its finesse decreases and the width of its transmission peaks increase according to equations 4.4 and 4.5 respectively. The increase in the calibration etalon transmission peak width can be seen when comparing figure 4.16a to figure 4.15a. At $\sim$720nm the calibration and locking etalon mirrors became completely transparent and it was no longer possible to produce the regular intensity profiles required for locking operation or calibration referencing. No long-wavelength etalon mirrors or alternative etalons were available during this work so ruthenium transitions beyond 720nm proved to be inaccessible.

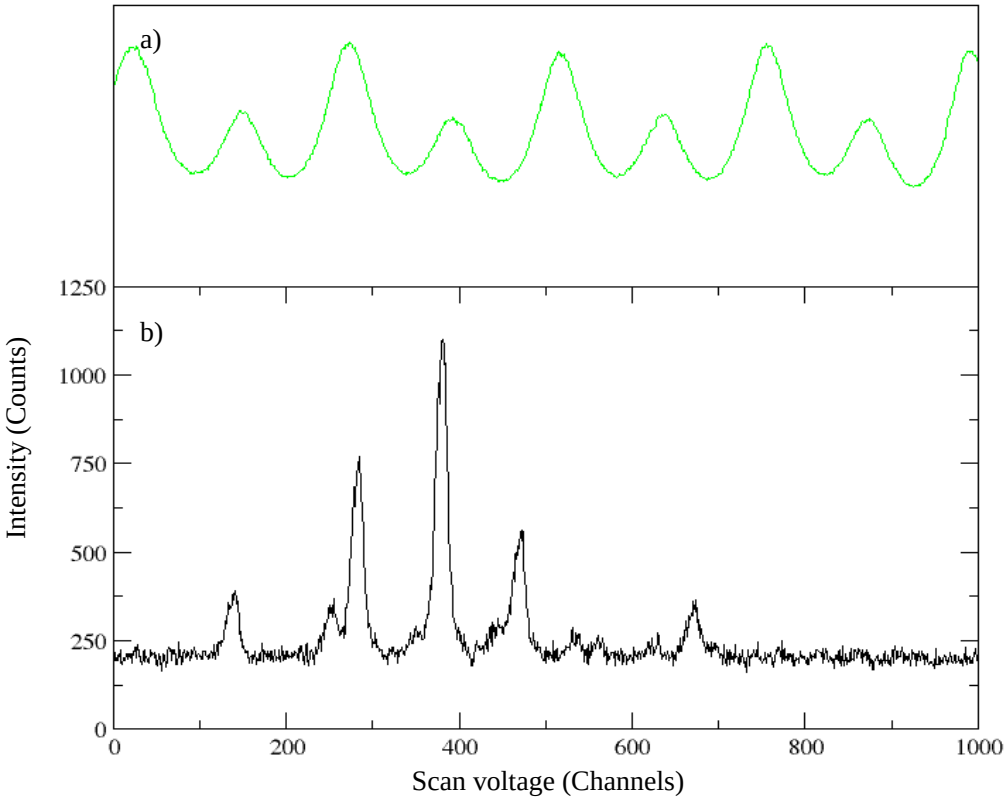

Figure 4.16: Spectrum of the 358.9213nm transition in ruthenium. a) The calibration etalon profile illustrating the decrease in etalon finesse. b) The atomic fluorescent spectrum.

Before P-2 was successfully employed, Pyridine-1 (P-1) was tested as an alternative dye for the same wavelength region. The absorption peak of P-1, however, is even further separated from the wavelength of the pump laser and it was found that even high dye concentrations were unable to produce sufficient power for use during experiments. P-1 was therefore abandoned in favour of P-2.

4.4.6 Atomic beam unit configuration

As discussed at the beginning of section 4.2, the central cylindrical vessel of the ABU consists of either two or three chambers depending upon the need for higher experimental efficiency or higher angular collimation respectively. The eleven R6-G transitions were measured using a two-chamber atomic beam unit arrangement in order to ensure that a large number of ruthenium atoms reached the interaction region with the laser. This decision was made prior to the discovery that (as discussed in 4.4.3) the R6-G transitions exhibited small isotope shifts which were difficult to resolve with the experimental resolution provided by a two-chamber ABU configuration. When moving to

other laser dyes the ABU was modified to a three-chamber configuration to improve the angular collimation of the experiment and hence improve the experimental resolution.

4.4.7 Oven damage

Ruthenium is a highly refractory element with a high melting point of 2607K[33]. Due to its high melting point, it was found that oven currents of 70-80A were required to produce atomic beams of sufficient density at the laser interaction region to produce a detectable number of fluorescent photons. At these temperatures, the tantalum ovens used during this work had an unusually high failure rate. Typically an oven can be used for many days of operation before a weakness develops in the tantalum and the oven breaks (usually at one of the arms). However, during ruthenium experiments a tantalum oven would often only last a few hours before developing a hole in the main oven body and then breaking. It would seem that at the high operation temperatures used during experiments the ruthenium would alloy with the tantalum of the oven and that the alloy produced had a lower melting point than the surrounding tantalum. As the ruthenium-tantalum alloy melted holes would develop in the oven. A series of tests were conducted where an element was positioned inside the oven and heated until largely evaporated. It was hoped that some of the melted element would alloy with the tantalum oven and form a protective layer that would prevent the formation of the damaging ruthenium-tantalum alloy. Copper, iron, aluminium and hafnium were tested, but no improvement in the average oven lifetime was observed.

Chapter 5

Analysis and Results

As described in section 4.4.2, nineteen electric dipole transitions were measured in atomic ruthenium by crossed-beam laser spectroscopy. In order to extract the physical parameters of interest from the measured spectra the data were analysed in three stages,

1. The x-axis of each spectrum was converted from channel numbers to relative laser frequency using a calibration based on the frequency spacing of the calibration etalon transmission peaks.

2. The various peaks in the atomic structure were identified and the centroids were fitted. From the atomic peak centroids the isotope shifts were determined and the hyperfine parameters extracted.

3. A combined analysis method was utilised in order to determine the change in mean-square-charge-radius (MSCR) between isotopes from the already extracted isotope shifts.

This chapter will discuss each of these steps in more detail and present the final experimental results. In addition to the nineteen transitions measured by the author, a further four transitions in atomic ruthenium were measured by E. Cochrane in 1999 using the same fundamental experimental set-up (see table 4.3). These four transitions were not published by E. Cochrane and have been analysed independently by the author of this work .

5.1 Data Calibration

5.1.1 Etalon drift

The measured fluorescence spectra are calibrated by comparison to the intensity profile of the calibration etalon. The calibration etalon transmission peaks provide regularly spaced frequency markers that can be used to convert data acquisition channels into frequency. However, before applying the calibration it is necessary to quantify and compensate for etalon drift. In an idealized situation the FSR of the calibration etalon would be constant over the course of a measurement of a single spectrum. In reality this is not the case due to changes in atmospheric conditions. The FSR of a confocal etalon is given by equation 4.6. Changes in air pressure and temperature result in the refractive index of the air inside the etalon changing (slowly) in time. This changes the speed of the light traveling inside the etalon and results in a small drift in FSR. Similarly, changes in temperature can lead to thermal changes in the length of the etalon. This will also contribute to a shift in etalon FSR. A change in etalon FSR, δFSR, causes the frequency of the n^{th} transmission peak to shift. The change in frequency of the n^{th} etalon peak, $\delta\nu_n$, can be calculated as follows,

$$\delta\nu_n = \nu_n - \nu_n^*, \tag{5.1}$$

$$\delta\nu_n = n(FSR + \delta FSR) - nFSR, \tag{5.2}$$

$$\delta\nu_n = n\delta FSR, \tag{5.3}$$

where ν_n and ν_n^* are the shifted and un-shifted frequency of the n^{th} etalon peak respectively. For visible light wavelengths $n \sim 10^6$ for the etalon peaks measured during a scan[20]. Therefore even small changes in the FSR due to atmospheric changes can result in a measurable shift in an etalon peak's frequency.

Figure 5.1 illustrates the experimental difficulties that arise as a result of etalon drift. The measurement of a spectrum typically takes a few minutes to complete. At time $t0$ during a laser scan the n^{th} etalon peak is measured at frequency $\nu_n^*(t0)$. The next etalon peak (the $(n+1)^{th}$ mode) would occur at frequency $\nu_{n+1}^*(t0)$ if the whole spectrum could be measured instantaneously. Instead the $(n+1)^{th}$ etalon peak is measured at frequency $\nu_{n+1}(t1)$ at the later time $t1$. In the time taken for the laser to scan between the two etalon peaks, changes in the etalon FSR cause the peak frequencies to drift. The measured FSR, $FSR_{meas} = \nu_{n+1}(t1) - \nu_n^*(t0)$ is therefore larger than the FSR if it could

be measured instantaneously ($= \nu^*_{n+1}(t0) - \nu^*_n(t0)$). Etalon drift results in the measured FSR changing over the course of a scan. Before using the position of the calibration etalon peaks to calibrate a spectrum it is important to first correct for etalon drift and move the etalon peaks back to their correct positions.

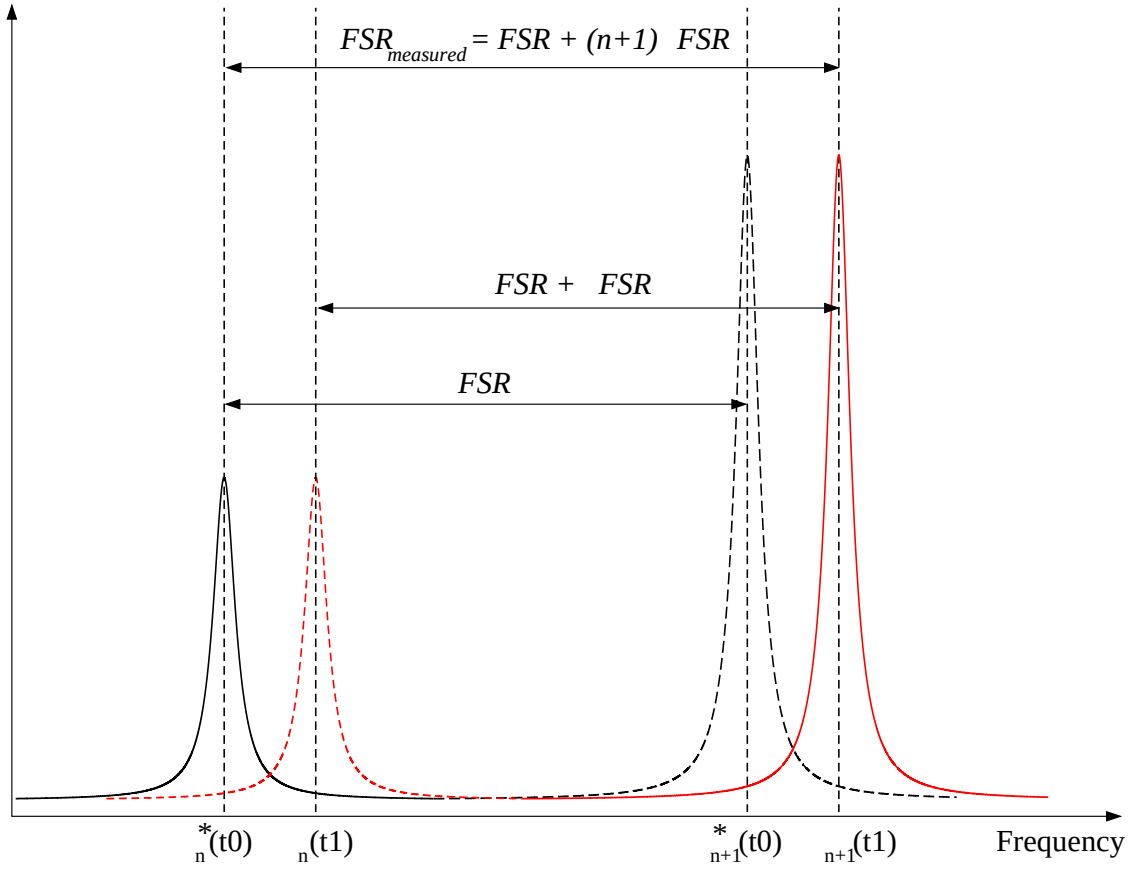

Figure 5.1: Etalon drift shifts the absolute frequencies of the etalon peaks in time. The measured etalon FSR ($\text{FSR}_{measured}$) is therefore greater than the instantaneous FSR.

D. Forest[20] proposed a method for returning the calibration etalon peaks to their correct positions by assuming that the etalon drift rate, ρ, expressed in channels per second, is linear in time. Equation 5.4 then relates the measured etalon peak centroid position, c_n, measured in channels, to its un-drifted centroid position, c^*_n, also measured in channels,

$$c_n = c^*_n + \rho\tau c_n, \tag{5.4}$$

where τ is the time spent by the laser at each frequency increment measured in units of seconds per channel. In order to use equation 5.4 to correct the etalon centroid positions the etalon drift rate, ρ must be determined. This is achieved by comparing a calibration

etalon centroid, c_n, to the centroid of an atomic resonance, c_{at}. The centroid of the atomic resonance provides a fixed frequency reference. For a scan started at time, t, the difference in channels between a specific etalon centroid and an atomic centroid, δ, is [20],

$$\delta = c_{at} - c_n = \delta_0 - \rho(t + \tau c_n) \tag{5.5}$$

where δ_0 is the difference between the two peaks in the absence of drift. The drift rate can therefore be determined by plotting δ against $t + \tau c_n$ for a series of successive measurements and by fitting equation 5.5 to the resulting data. The gradient of the line yields the drift rate, ρ. Figure 5.2 shows an example of such a plot for ten measurements of the 358.921nm transition. Three different isotopes are used as frequency references to three different etalon peaks. All three data sets are linear which justifies the assumption made earlier that the etalon drift rate is constant.

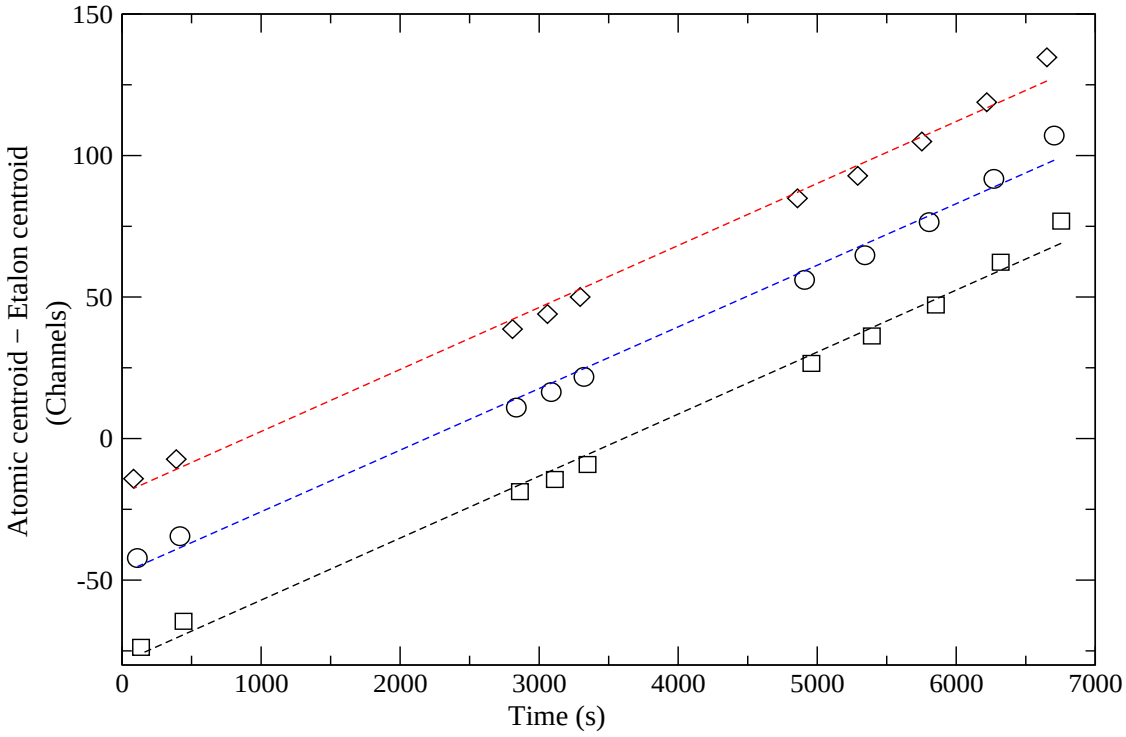

Figure 5.2: Graph displaying the difference between 104 (diamond), 102 (circle) and 100 (square) isotopes and specific etalon peaks for ten measurements of the 358.921nm transition taken at different times. The errors are smaller than the data points.

Figure 5.3 illustrates the difference between a spectrum calibrated with and without etalon drift correction. As the scan progresses, the effect of etalon drift leads to an increasing difference in frequency calibration which can lead to a significant change in

peak centroid frequency.

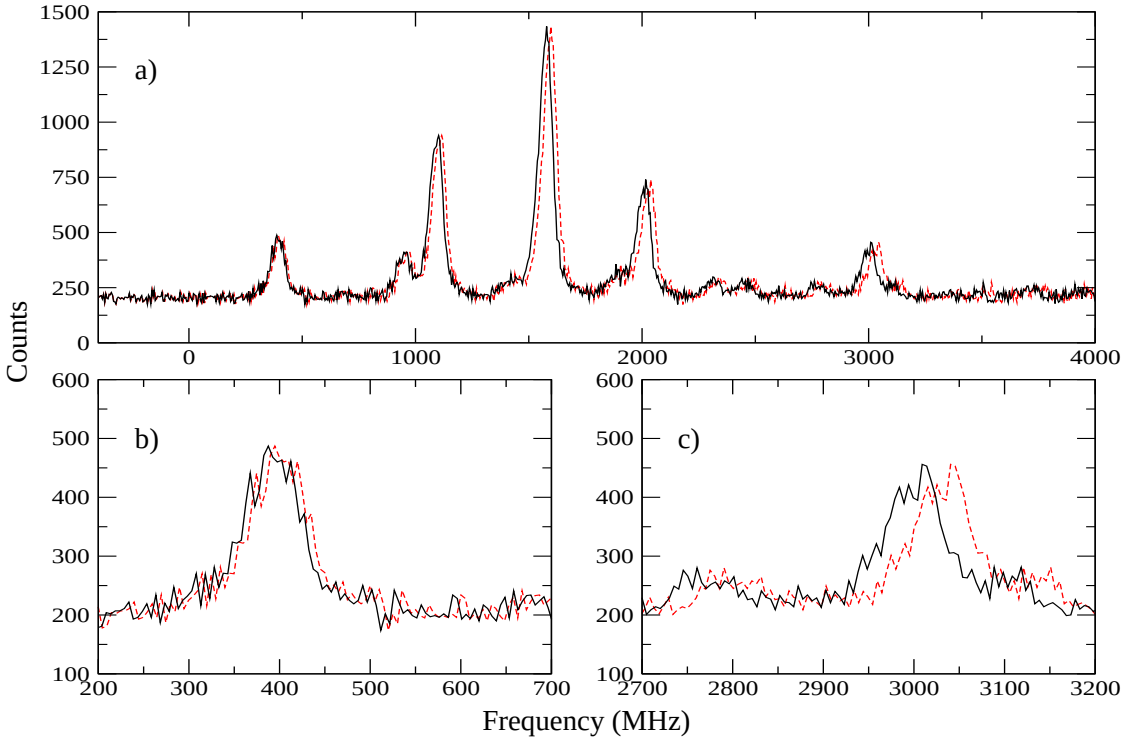

Figure 5.3: a) Spectrum of the 358.921nm transition calibrated with (black, solid trace) and without (red, dashed trace) etalon drift compensation. Enlargement of b) the start and c) the end of the scan region.

5.1.2 Calibration Methods

Once etalon drift has been compensated for and the calibration etalon peak centroids returned to their correct channels the spectrum can be calibrated. A version of *xmgrace*[34] (modified by D.Forest to include calibration and peak fitting routines) is used to determine the centroids of the calibration etalon peaks in terms of channel numbers and to perform the calibration. Each of the m etalon peaks in the spectrum is assigned a frequency, ν_m,

$$\nu_m = (m-1)FSR, \tag{5.6}$$

so the first etalon peak in the spectrum, $m = 1$, is designated the frequency 0MHz. One of three functions is then fitted to the calibration etalon centroids to determine the laser frequency assigned to each channel. Figure 5.4 displays plots of calibration etalon peak centroids in channels versus the corresponding laser frequency (determined using equation 5.6) along with the three types of calibration functions. The data points plotted in figure 5.4 have been synthesized to illustrate the small non-linearities that are observed

in most experimental scans however the magnitude of those non-linearities have been exaggerated here to make them more visible. Each calibration function will now be discussed in more detail.

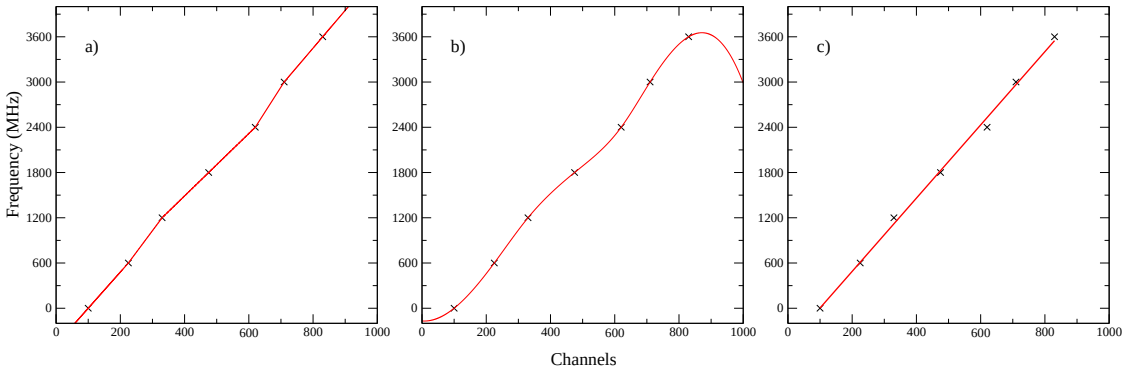

Figure 5.4: Plots of laser frequency (MHz) against calibration etalon peak centroids (channels) with a) a local linear fit, b) a cubic spline fit and c) a global linear fit.

5.1.3 Local Linear Calibration

The local linear calibration method assigns each etalon centroid channel with a frequency determined by equation 5.6 and then assumes a linear frequency per channel relationship between adjacent etalon peaks. Each spectrum channel, c_x, in between two etalon peaks with centroids at channel c_m and c_{m+1} is then assigned a frequency, ν_x, given by,

$$\nu_x = \nu_m + (c_x - c_m)\frac{FSR}{(c_{m+1} - c_m)}. \tag{5.7}$$

Figure 5.4a shows the local linear function applied to a synthesized data set. The spectrum channels prior to the first calibration etalon peak are extrapolated using the frequency per channel relationship between the first two etalon peaks. Similarly, the channels after the last etalon peak in the scan are extrapolated using the frequency per channel ratio from in between last two etalon peaks.

The local linear calibration utilises the calibration etalon peaks as markers in a spectrum where the laser frequency is known and then assumes that the laser frequency changes linearly in the space between adjacent markers. By fitting separate linear relationships to the space between each pair of etalon peaks this method can compensate for any small non-linearities in the scan of the laser frequency.

5.1.4 Cubic Calibration

The cubic calibration method uses an interpolated cubic spline function to determine the relationship between channel number and laser frequency. Figure 5.4b shows an example cubic spline function. Like the local linear calibration, the cubic calibration function utilises the calibration etalon peak centroids as fixed frequency markers. The cubic spline function however is able to fit more smoothly to the whole data set and provides a more realistic representation of the change in laser frequency between etalon peaks. The channel numbers before the first etalon peak and after the last etalon peak are calibrated by extrapolating the cubic spline out to those channel numbers. Unlike the local linear fit, the cubic spline extrapolation can lead to unrealistic calibrations at the front and end of a scan. This effect is evident (although exaggerated due to the deliberately emphasized non-linearities in the synthesized example data set) in figure 5.4b where the fit curves back around after the last etalon peak. The cubic calibration, whilst providing a more realistic fit to scan non-linearities, should be used carefully.

5.1.5 Global Linear Calibration

The global linear calibration method performs a linear regression on the frequency and channel numbers assigned to the calibration etalon centroids. The equation obtained for the linear fit is then used to convert spectrum channel numbers into laser frequency. This method does not require that the fit passes through all of the measured calibration etalon peak values, as illustrated by figure 5.4c, however it does demand that the laser frequency scan is linear across the whole spectrum. This method allows for errors in etalon peak positions by not forcing the fit to go through all of the etalon data points.

The local linear calibration method was the most commonly used calibration method during this work. This is because this method is the most simple and utilises each of the calibration etalon peaks as reference points in the spectrum where the laser frequency is known. If a fit to a spectrum calibrated using the local linear method produced a large χ^2 value then the spectrum was re-calibrated using either the cubic or global calibration methods in an attempt to achieve an improved fit χ^2 value. If the χ^2 value for the fit was then still large then it was assumed that a substantial glitch had occurred during the laser scan (causing irregular etalon spacing) and the spectrum was not included when averaging the repeat measurements together to yield the final results.

5.2 Fitting the Spectra

Ruthenium has seven naturally occurring isotopes, ^{96}Ru, ^{98}Ru, ^{99}Ru, ^{100}Ru, ^{101}Ru, ^{102}Ru and ^{104}Ru. Each of the even isotopes contributes a single peak to the observed spectrum. The odd isotopes have spin $I = 5/2$ and therefore each contribute several hyperfine (HF) structure component peaks to the spectrum. Figure 5.5 displays a calibrated measurement of the 349.8942nm transition. This transition is a $J = 5$ to $J = 6$ transition so each odd isotope contributes fifteen HF structure peaks to the spectrum. Overall, the 349.8942nm transition produces thirty five potentially measurable peaks of various intensities in the spectrum.

In order to calculate the isotope shifts evident in a spectrum it is necessary to accurately determine the centroid of each peak in the spectrum. This is achieved by using a chi-squared minimisation fitting routine in a modified (by D. Forest) version of *xmgrace*[34] which attempts to fit a function to the data. Every component in the spectrum is described by a line shape $P(\Gamma)$ where Γ represents the width parameter (or parameters for the case of a Voigt profile). The contribution of the i^{th} component to the fit function is,

$$F_i(\nu) = I_i P_i(\Gamma, \nu - \omega_i), \tag{5.8}$$

where I_i and ω_i are the intensity and centroid of the i^{th} component respectively. The full fit is therefore given by the sum of all of the individual components,

$$y(\nu) = \sum_i F_i(\nu). \tag{5.9}$$

For hyperfine structure components the parameter ω_i is dependent upon the hyperfine A and B parameters of the transition states and the weighted centroid of the isotope (see equation 2.69). The values for ω_i for all of the HF structure components of a single isotope are therefore interlinked via these isotope dependent properties.

The fitting routine compares the fitted line function, $y(\nu)$, to the measured spectrum and determines the chi-squared value for the fit function. The programme then varies the aforementioned line function variables in an iterative process in order to achieve the minimum value for chi-squared. The final values for the isotope centroids generated by the fitting routine can then be used to calculate isotope shifts. By fitting the whole spectrum using a single function the fitting routine takes into account the relative positions

of all of the peaks. This is advantageous for determining accurate HF parameter values. Separate aspects of the fitting routine will now be discussed in more detail.

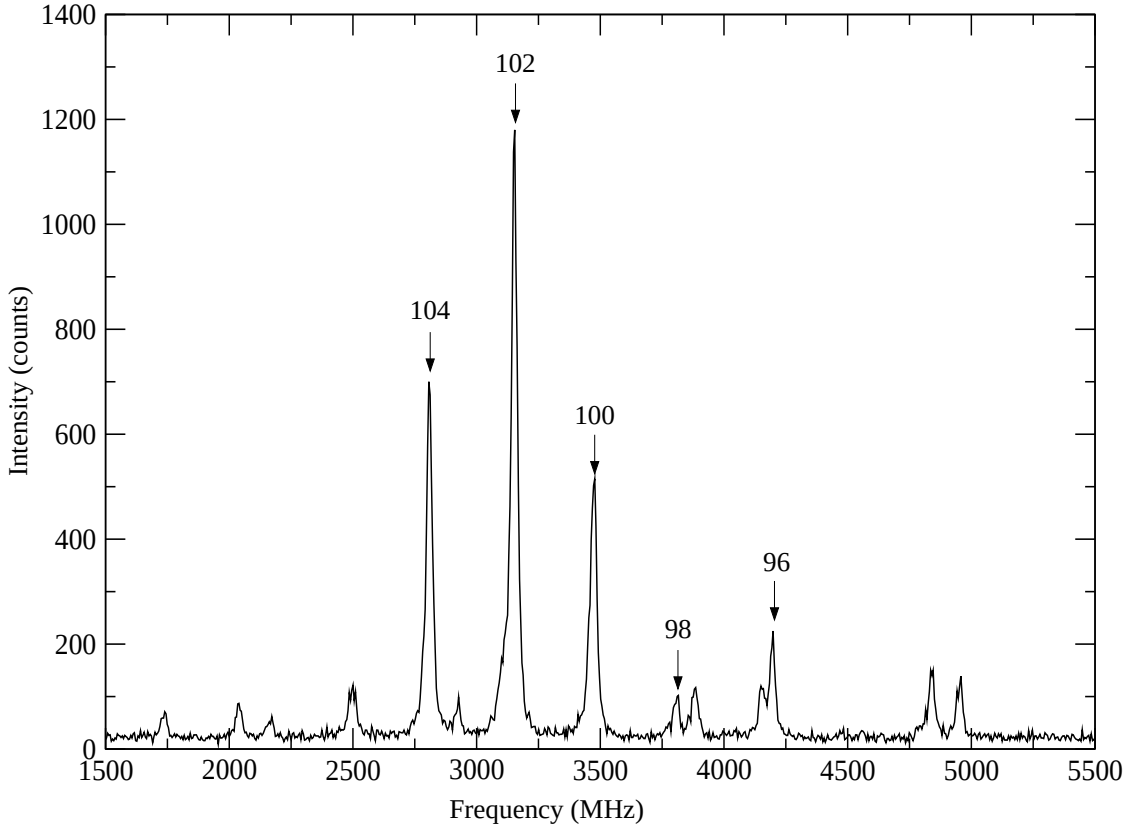

Figure 5.5: Calibrated spectrum of the 349.8942nm transition. The even isotope centroids are labeled. The remaining unlabeled peaks are hyperfine structure components.

5.2.1 The Fitted Line-Shape

As discussed above, the fitted spectrum consists of a sum of line-shape functions. The shape of the line-shape function is determined by the dominant line-broadening mechanism that is evident in the measured spectrum. Therefore the same line-shape and line-width is applied to every peak in the spectrum (see section 3.1). The programme user may choose which line-shape function is used by the fitting routine. The available options are Lorentzian, Gaussian and Voigt profiles. The Lorentzian function is best suited to spectra where the natural-line width defines the measured peak shape. The Gaussian function is required for spectra where Doppler broadening is the dominant broadening mechanism. The Voigt profile is used when the natural line-width and Doppler broadening are of similar magnitude. Ultimately, the final choice of line-shape is made by the chi-squared minimisation fitting routine. The line-shape that produces the best fit (i.e. the smallest reduced χ^2/degree of freedom value) is used as the final choice for a spec-

trum. For the vast majority of analysed spectra, a Voigt profile was found to produce the best fit.

5.2.2 Identifying the Spectrum Peaks

In order for the fitting routine to correctly fit a measured spectrum the user must enter preliminary values for each of the variable parameters. It is therefore important to be able to identify which peaks correspond to each isotope so that initial estimates for the isotope centroids can be determined. The even isotopes can be identified by comparing the relative measured peak intensities to the known atomic abundances of ruthenium displayed in table 5.1.

Istope	Abundance (%)	Abundance relative to ^{102}Ru	Spin (I^{π})
^{96}Ru	5.54	0.176	0
^{98}Ru	1.87	0.059	0
^{99}Ru	12.76	0.404	5/2+
^{100}Ru	12.60	0.399	0
^{101}Ru	17.06	0.541	5/2+
^{102}Ru	31.55	1.000	0
^{104}Ru	18.62	0.591	0

Table 5.1: Ruthenium naturally occurring atomic abundances [35].

This method was used to label the even isotopes in figure 5.5. The remaining unlabeled spectrum peaks are hyperfine structure components belonging to either ^{101}Ru or ^{99}Ru. A preliminary value for the centroid of the odd isotope structures can be determined by examining the centroid positions of the even isotopes. An approximate linear relationship exists between the even isotope centroid positions and mass number (see figure 5.6). This linear relationship is confirmed by examining the charge radii systematics for molybdenum for the same neutron number values (see figure 1.1). Molybdenum has two fewer protons than ruthenium and would therefore be expected to exhibit similar changes in isotope shift with neutron number. The values for $\delta\langle r^2\rangle^{A,A'}$ for molybdenum are approximately linear across the range $50 < N < 60$ which (from equation 2.28) implies a linear change in isotope shift with neutron number.

Assuming that this linear relationship is also valid for the odd mass isotopes allows approximate centroid frequencies for ^{101}Ru and ^{99}Ru to be interpolated. In reality it is likely that the odd mass ruthenium isotopes will be staggered relative to the even isotopes. Odd-even staggering (OES) is evident in the isotope chains of all elements in this region of the nuclear chart as displayed in figure 1.1. However the magnitude of OES is sufficiently small in the neighbouring isotope chains that its effects can be assumed negligible for the purpose of an initial estimate of the centroid values for the odd ruthenium isotopes.

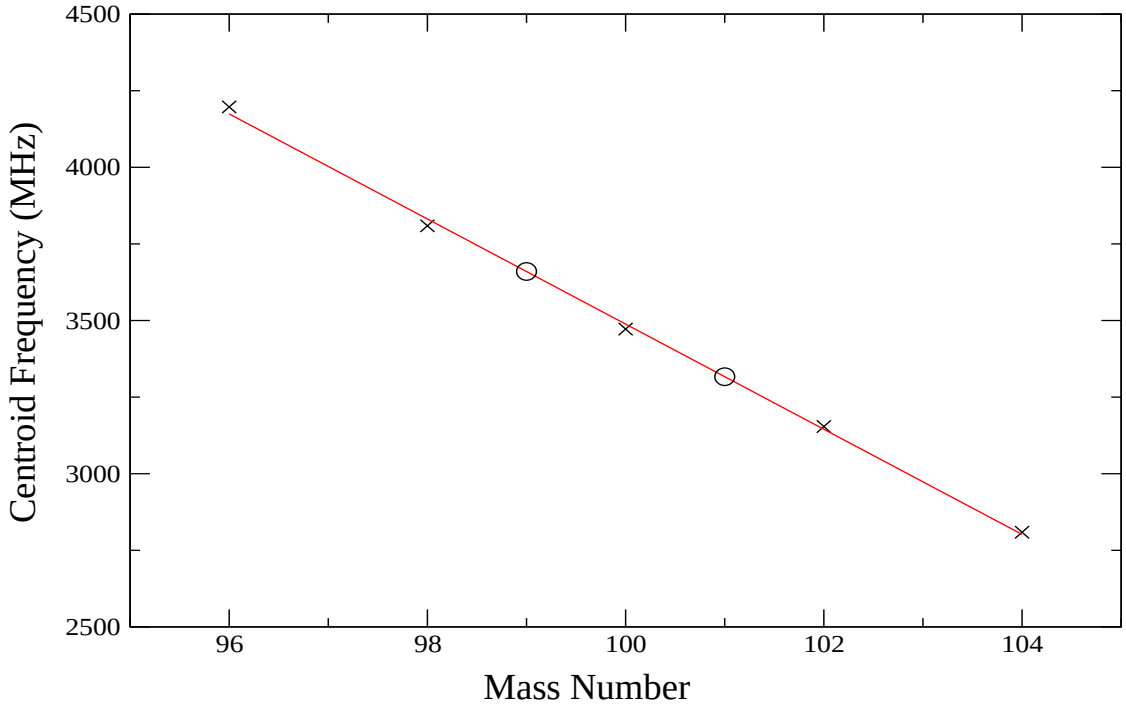

Figure 5.6: Graph displaying peak centroid frequency against mass number for the 349.8942nm transition. The odd isotope centroids (o) are calculated using the line of best fit through the plotted even isotopes (x). Error bars are comparable to the size of the data points.

It is also necessary to provide the fitting routine with preliminary values for the HF parameters. For the four lowest atomic energy levels the HF A and B parameters have been measured accurately for both ^{101}Ru and ^{99}Ru by magnetic resonance experiments (Büttgenbach et al[36]). These values are listed in table 5.6 in section 5.3 below. For transitions from these energy levels, only the values of the upper state HF parameters are unknown. The parameters A_U and B_U are determined for each isotope separately by setting up and solving simultaneous equations of the form,

$$\nu_i = A_U\alpha_i^U + B_U\beta_i^U + \omega - A_L\alpha_i^L + B_L\beta_i^L, \tag{5.10}$$

where ν_i is frequency of the i^{th} HF structure component, the parameters α and β are given by equations 2.71 and 2.72 respectively, ω is the isotope centroid that was estimated above (using figure 5.6) and A_L and B_L are known. To solve for one of the odd isotopes it is necessary to identify two peaks belonging to that isotope with frequency ν_1 and ν_2.

The intensity of each HF structure component can be predicted through a series of scaling relations. Firstly, the intensity of a specific HF structure component between two F states, F_L and F_U, can be calculated using the Racah intensity equation,

$$Intensity \propto (2F_U + 1)(2J_L + 1)(2J_U + 1) \left| \begin{Bmatrix} J_L & F_L & I \\ F_U & J_U & 1 \end{Bmatrix} \right|^2 , \qquad (5.11)$$

where the subscripts U and L denote the transition upper and lower state respectively. For more information on the origin of equation 5.11 see Edmonds[37]. The relative intensity of each hyperfine component can then be scaled relative to the most intense HF component. Table 5.2 below displays the Racah intensities (relative to the most intense component) of the 15 HF components for the 349.8942nm transition. The Racah intensities were calculated by a subroutine (written by D. Forest) of *xmgrace*[34].

F_L	F_U	Intensity
15/2	17/2	1
13/2	15/2	0.839506
11/2	13/2	0.699301
9/2	11/2	0.578512
7/2	9/2	0.476618
5/2	7/2	0.393939
11/2	11/2	0.085823
13/2	13/2	0.077355
9/2	9/2	0.076183
15/2	15/2	0.049383
7/2	7/2	0.048634
11/2	9/2	0.002755
13/2	11/2	0.002331
9/2	7/2	0.001871
15/2	13/2	0.001122

Table 5.2: Racah intensity† (expressed as a fraction of the most intense component) for the HF components of the 349.8942nm ($J_L = 5 \longrightarrow J_U = 6$) transition. Nuclear spin $I = 5/2$. † calculated using a subroutine of the program xmgrace.

The expected intensity can then be determined for that peak by scaling to the identified even isotopes according to the atomic abundance. Comparing the predicted intensities to the measured spectrum enables two peaks to be selected for use in the simultaneous equations. From table 5.2 it can be seen that whilst each odd isotope has 15 HF components for the 349.8942nm transition only six HF components (including the most intense component) have an intensity greater than ten percent of the most intense component. This is true for most of the transitions measured during this work and hence typically only a few HF components are visible for each odd isotope in a spectrum.

As the HF parameters are not known for the 3105.49cm^{-1} state it is necessary to assemble a set of four simultaneous equations in order to determine preliminary values of A_L, B_L, A_U and B_U for any transition from this state.

Determining intial values for the HF parameters in this manner can be challenging for narrow spectra as the HF structure lines are often close together or obscured by even

isotopes and hence are difficult to identify. For these spectra it can be useful to generate a chi-squared surface plot of the fit using various input values for A_U and B_U. The method for generating a chi-squared surface plot is discussed in appendix B. Initial values for A_U and B_U can then be determined by identifying the position of the global minimum in the chi-squared surface plot. This method can be time consuming and is generally not necessary for well spaced spectra.

5.2.3 Reducing the Number of Fit Parameters

In order to ensure that the fitting routine finds the global chi-squared minimum a number of the fit parameters are initially either fixed or linked together using known physical values and scaling relationships. As has previously been mentioned the lower state HF parameters are known for many transitions from magnetic resonance experiments. A_L and B_L are therefore held fixed to these measured values during the fitting process. Fixing these parameters is justified by the fact that the accuracy of the magnetic resonance measurements is significantly greater than the accuracy that can be obtained in a laser spectroscopy experiment.

As outlined in section 2.3, the ratio of the upper state HF A parameters is equal to the ratio between the lower state HF A parameter as follows,

$$\frac{A_L^{99}}{A_L^{101}} = \frac{\mu_{99}/I_{99}}{\mu_{101}/I_{101}} = \frac{A_U^{99}}{A_U^{101}}. \tag{5.12}$$

The HF upper parameter of one isotope can therefore be scaled to the other odd isotope as follows.

$$A_U^{99} = A_U^{101}\frac{A_L^{99}}{A_L^{101}}. \tag{5.13}$$

Equation 5.13 is also true for the HF B parameters. The peak intensities are also scaled during the fitting process. Firstly, the isotope intensities are all scaled to an even isotope, usually ^{102}Ru as it has the greatest intensity, according to atomic abundances. The measured intensities should replicate the atomic abundances provided that the detection system was not saturated during the measurement. Secondly, the hyperfine structure peaks are scaled relative to the most intense HF peak according to the Racah intensities. It is often the case that some HF components are found underneath the considerably more intense even isotope peaks. Scaling the HF components' intensities according to

the HF components ensures that even peaks masked in this way are considered correctly by the fitting routine.

The scaling ratios described above were enforced during the chi-squared minimisation process in order to obtain initial values for the peak centroids and HF parameters. Once obtained, the scaling ratios were released one-by-one and the fitting routine was repeated to assess the impact of the scaling factor on the chi-squared per degree of freedom value for the fit. It was found that releasing the scaling ratios produced a negligible change in the chi-square per degree of freedom value for the majority of spectra. This justified the use of scaling ratios to fit the data.

5.3 Isotope Shifts and Hyperfine Parameters

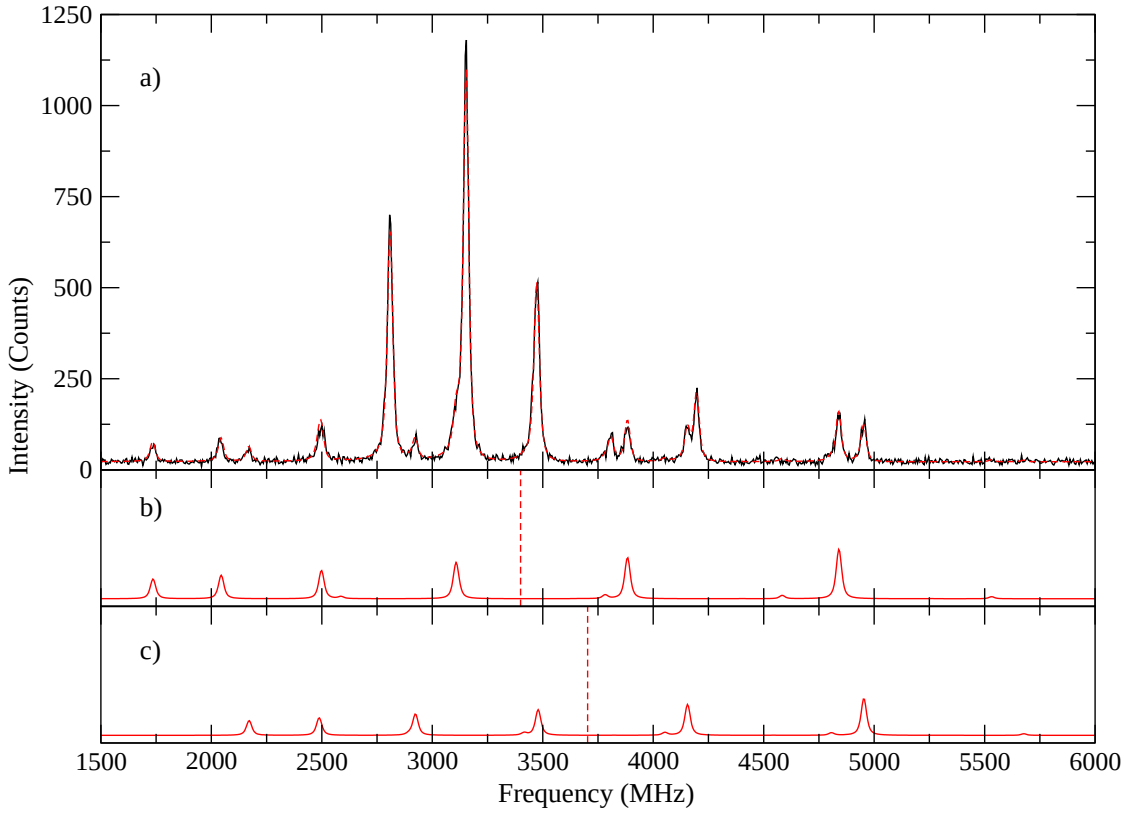

Figure 5.7: a) A fitted 349.8942nm transition (χ^2 per degree of freedom = 1.59). b) The ^{101}Ru peaks with the centroid marked with a dashed line. c) The ^{99}Ru peaks with the centroid marked with a dashed line.

Figure 5.7 displays an example of a fully calibrated and fitted spectrum. Once the isotope centroids are determined using the fitting routine, the isotope shift between two isotopes can be calculated using equation 2.1. Table 5.3 displays the measured isotope shifts, relative to the ^{104}Ru isotope, for eight of the transitions measured during this work and

λ (nm)	102	101	100	99	98	96
298.8947	137.6(8)	213.6(15)	277.2(14)	356.0(17)	426.4(14)	579.6(19)
315.9929†	199.7(3)	326.2(3)	395.4(4)	517.6(2)	597.9(11)	823.9(4)
318.6043†	202.5(2)	330.3(4)	400.4(3)	524.7(5)	605.3(8)	834.9(3)
318.9979†	175.3(4)	280.7(2)	350.6(2)	453.9(10)	532.2(13)	730.2(7)
319.6605†	191.5(5)	309.9(6)	379.4(8)	495.6(5)	574.5(16)	791.5(6)
329.4112	428.1(18)	750.2(26)	827.2(22)	1124.6(18)	1238.7(24)	1732.2(19)
330.1594	448.2(6)	777.7(22)	857.3(12)	1164.6(10)	1286.4(24)	1792.3(21)
343.6736	453.4(23)	792.5(30)	873.3(39)	1186.3(39)	1302.3(37)	1827.7(46)
349.8942	346.6(18)	595.0(19)	672.2(24)	904.4(19)	1008.3(29)	1404.4(29)
358.9213	479.0(32)	828.3(30)	918.4(19)	1235.3(29)	1361.1(25)	1899.9(50)
359.3018	455.8(14)	801.3(22)	879.9(18)	1196.8(26)	1327.0(31)	1841.5(49)
359.6178	278.9(17)	461.1(22)	536.2(17)	706.5(29)	805.7(34)	1125.7(25)

Table 5.3: Measured isotope shifts (MHz) relative to ^{104}Ru. † signifies a transition measured by E. Cochrane but analysed by the author.

the four transitions measured by E. Cochrane. Each value in the table is an average of at least five repeat measurements. The fitting routine also calculates the fitting error for each centroid which can be used to determine a value for the isotope shift error. The error on the fit to the data is typically very small $\sim$0.1MHz. The error values displayed in the table are the standard errors calculated from the standard deviations between repeat measurements. This value is larger than the error on the fit and, for this reason, is chosen as the definitive error on the isotope shift as it better reflects the level of experimental uncertainty.

Table 5.4 displays the hyperfine structure coefficients of the transition upper energy levels for the same twelve transitions displayed in table 5.3. As for the isotope shift values, the displayed HF parameters are an average of at least five repeat measurements. Similarly, the displayed error values are calculated from the standard deviation of the repeat measurements. For all measured transitions, the error on the B parameters is always much larger than that for the A parameters. This is due to the fact that the electric quadrupole interaction has a considerably smaller perturbative effect upon the electronic energy levels than the magnetic dipole interaction. Changing B therefore has a small effect on the spectrum. This leads to larger variation in fitted B values between repeated measurements which in turn leads to a greater standard error.

Table 5.5 displays the hyperfine structure components of the 3105.49cm^{-1} state extracted from analysis of the 319.6606nm and 358.9213nm transitions. There is generally good agreement between the two transition measurements except for the ^{99}Ru B coefficient. There is no obvious reason for this discrepancy other than the previously mentioned fitting routines' lack of sensitivity to the value of the HF B parameters. Using the B HF coefficient equivalent of equation 5.13 it is possible to estimate the expected HF B coefficient for ^{99}Ru from the HF B coefficient for ^{101}Ru by multiplying the ^{101}Ru B coefficient extracted from measurements with the ratio of B coefficients from a different atomic energy level (such as those obtained by magnetic resonance measurements[36] in table 5.6). Scaling the ^{101}Ru B coefficient for the 319.6606nm transition (displayed in table 5.5) in this way replicates (within errors) the measured 319.6606nm ^{99}Ru B coefficient. However, scaling the ^{101}Ru B coefficient for the 358.9213nm transition (displayed in table 5.5) in this way yields a results that is not consistent with the measured 358.9213nm ^{99}Ru B coefficient. The 358.9213nm transition has a large number of small hyperfine structure components that are easily lost in the spectrum background which

may cause the fitting routine to provide an inaccurate value for the B HF coefficients. This suggests that the HF coefficients obtained from the 319.6606nm transition are more reliable than those obtained from the 358.9213nm transition. For this reason, the HF coefficients obtained from the 319.6606nm transition are used as the definitive HF coefficients for the values 3105.49cm^{-1} and are displayed in table 5.6 with the magnetic resonance measurements for the HF parameters of the other members of the ground state multiplet. This is the first measurement of the HF parameters for the 3105.49cm^{-1} state.

As discussed in section 4.4.3, the 296 – 310nm transitions studied during this work exhibit extremely small isotope shifts and hence have very narrow spectra. For this reason, these spectra proved very difficult to analyse as it is often the case that large numbers of hyperfine components are masked beneath the closely spaced even isotopes. This is also true for the 342.8318nm transition. Small isotope shifts make these transitions unsuitable for extracting nuclear mean-squared charge radii (as will be discussed in section 5.4) and for this reason the isotope shifts and HF parameters determined for these transitions (with the exception of the 298.8947nm transition) are not displayed here. However, the transitions were fitted and values for the measured isotope shifts and HF parameters can be found in appendix C. It is worth noting that the fit to the 304.2478nm transition provides HF coefficient values for the 3105.49cm^{-1} energy level (see table C.2) that are consistent with the values obtained from the 319.6606nm transition displayed in table 5.5. This provides further confirmation for selecting the HF coefficients obtained from the 319.6606nm transition as the definitive values for the 3105.49cm^{-1} state.

			99		101	
λ (nm)	E_u (cm^{-1})	J	A_u	B_u	A_u	B_u
298.8947	33446.84	4	-156.6(2)	-6.1(36)	-175.2(2)	-10.7(35)
315.9929	33728.66	2	-105.2(1)	-7.7(9)	-117.8(1)	-47.0(6)
318.6043	34091.06	1	-97.8(2)	8.3(13)	-109.7(1)	39.6(9)
318.9979	33430.65	3	-133.1(1)	-26.7(29)	-149.3(1)	-149.7(28)
319.6605	34379.64	0	0	0	0	0
329.4112	30348.45	4	-78.0(2)	8.5(54)	-87.3(3)	16.3(86)
330.1594	30279.68	5	-66.5(2)	33.8(45)	-74.3(5)	226.1(91)
343.6736	30279.68	5	-66.5(2)	39.8(38)	-74.5(3)	243.6(75)
†	30279.68	5	-66.5(1)	37.3(29)	-74.5(2)	236.6(58)
349.8942	28571.89	6	-86.7(1)	55.7(38)	-97.1(1)	349.6(38)
358.9213	30958.80	2	-224.1(10)	9.7(82)	-249.1(5)	162.8(28)
359.3018	30537.06	3	-109.9(5)	28.5(50)	-123.4(3)	178.9(27)
359.6178	29890.91	4	-114.6(1)	19.0(43)	-128.8(5)	125.2(88)

Table 5.4: Measured hyperfine structure parameters (MHz) of the transition upper states for both ^{99}Ru and ^{101}Ru. † signifies the weighted mean values for the 30279.68cm^{-1} state using the 343.67nm and 330.16nm transition data.

	99		101	
Transition λ (nm)	A	B	A	B
319.6605	107.1(2)	7.3(6)	119.6(2)	39.0(3)
358.9213	105.3(8)	0.8(13)	121.0(7)	40.8(13)

Table 5.5: Measured hyperfine structure parameters (MHz) of the 3105.49cm^{-1} state for both ^{99}Ru and ^{101}Ru.

		99		101	
E (cm^{-1})	J	A	B	A	B
0.00 (†)	5	-204.5514(33)	27.281(62)	-229.2881(33)	158.934(62)
1190.64 (†)	4	-163.6845(36)	17.455(52)	-183.4744(36)	101.799(52)
2091.54 (†)	3	-135.0294(37)	10.164(50)	-151.3502(38)	59.323(50)
2713.24 (†)	2	-82.5325(27)	5.457(22)	-92.4974(27)	31.869(23)
3105.49	1	107.11(15)	7.28(64)	119.63(20)	38.97(34)

Table 5.6: Hyperfine structure parameters (MHz) for the ground state multiplet. States labelled † are values from Büttgenbach et al.[36] whereas the 3105.49cm^{-1} values are the weighted mean of results listed in table 5.5.

5.4 Extracting the Change in Mean Square Charge Radius between Isotopes

The change in mean-squared charge radius, $\delta\langle r^2\rangle^{A,A'}$, between isotopes A and A' was determined using the combined analysis technique discussed in detail by Fricke et al.[38, 2]. The combined analysis method draws together data from numerous different types of experiments in order to determine a more accurate value for $\delta\langle r^2\rangle^{A,A'}$. Data from the following four types of experiment are typically used in the technique:

1. Optical isotope shift measurements (such as those measured during this work). Optical isotope shifts (such as those in table 5.3) are related to the change in mean square charge radius between isotopes as outlined in section 2.1.3. Optical isotope shifts can be measured to a relatively high level of accuracy however extraction of $\delta\langle r^2\rangle^{A,A'}$ values requires knowledge of the electronic factors F_i and M_i. Ab initio calculations of F_i are often very challenging due to the non-trivial task of calculating the change in electron charge density at the nucleus which requires detailed knowledge of the electron wavefunction. Similarly ab initio calculations of M_i are difficult as they require calculation of the specific mass shift which also requires knowledge of the electron wavefunction.

2. K X-ray measurements. Like optical transitions, K X-ray transitions exhibit mass and field shifts which are similarly related to the $\delta\langle r^2\rangle^{A,A'}$. The advantage of K X-ray measurements over optical transitions is that the electronic parameters F_i

and M_i can be calculated considerably more accurately for inner electrons than valence electrons. The disadvantage of K X-ray measurements is the much poorer experimental accuracy relative to optical isotope shift measurements[1].

3. Muonic X-ray measurements. Muon X-ray experiments measure the transition energies between the levels of a muon bound in an atom. As a muon is considerably heavier than an electron it orbits much closer to the nucleus and is very sensitive to its size. Perturbations in the muon energy levels due to the size of the nucleus are related to the Barrett equivalent radius, $R_{k\alpha}$[2].

4. Electron scattering measurements. Electron scattering experiments provide accurate measurements of the nuclear charge distribution $\rho(r)$ which enables calculation of all of the nuclear radial moments, $\langle r^n \rangle^{1/n}$. Electron scattering data also enables values of $R_{k\alpha}$ to be determined, however to a lower degree of accuracy than that from muon experiments.

Each experiment measures a different property of the charge distribution of the nucleus. Figure 5.8 displays a flow chart of the processes required to produce a combined value for $\delta\langle r^2 \rangle^{A,A'}$. The ratio of the radial moments from electron scattering data, V_n^e, is used in conjunction with the Barrett equivalent radius extracted from muon data, $R_{k\alpha}^{\mu}$, to obtain precise model-independent radii values, $\langle r^n \rangle_{\mu e}^{1/n}$. The change in nuclear Seltzer moments between isotopes can then be determined using equation 2.25. A more accurate value for the Seltzer moment, $\lambda_{o\mu e}^{AA'}$, is formed via a graphical technique known as a King plot. This technique, first proposed by King[1], will now be described in more detail.

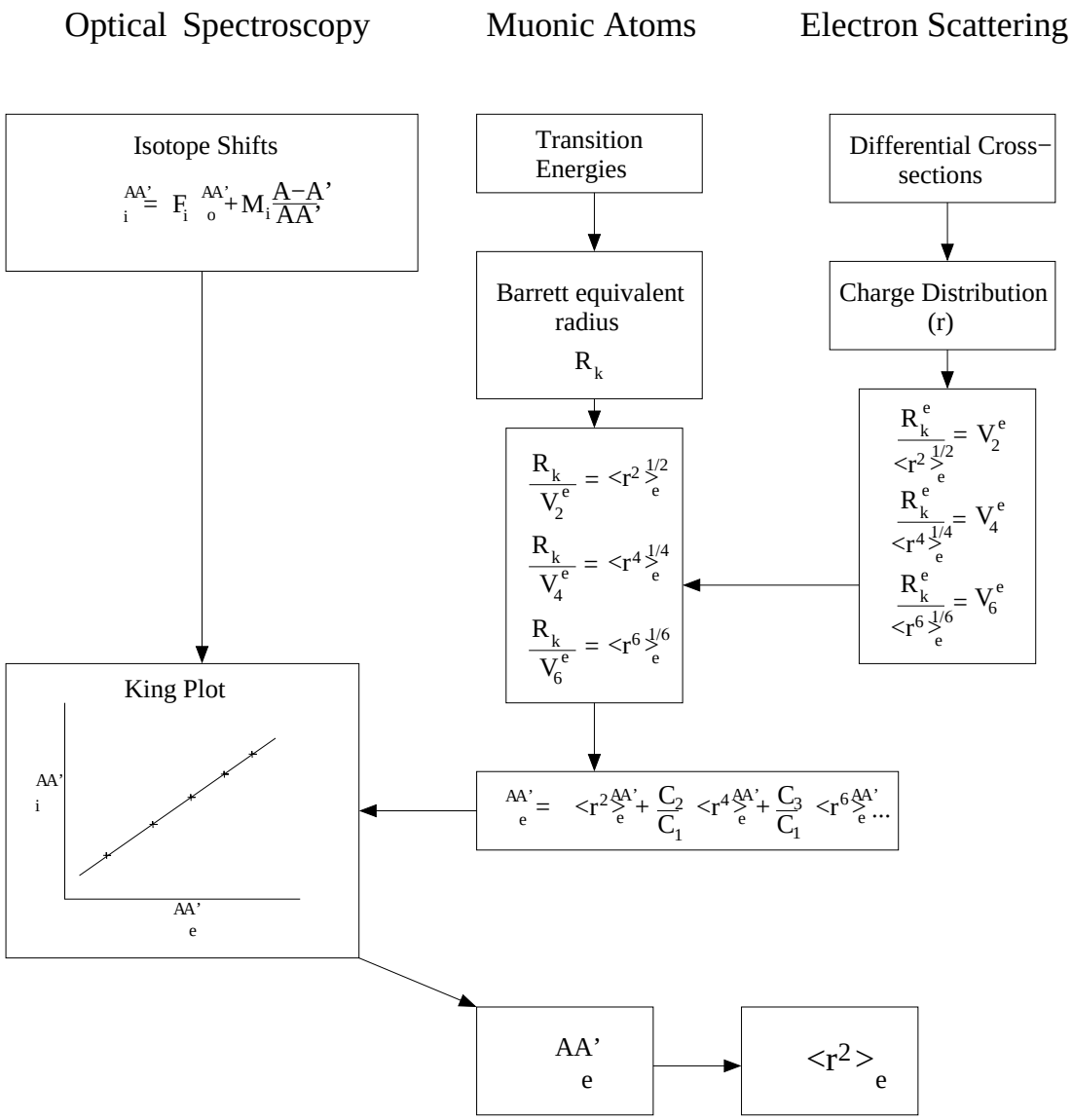

Figure 5.8: Flow diagram (reproduced from [38]) illustrating how different experimental results combine to determine $\delta\langle r^2\rangle^{A,A'}$. Subscripts o, e and μ illustrate parameters extracted from optical, electron scattering and muonic experiments respectively.

5.4.1 The King Plot Method

For a transition, i, the measured isotope shifts, $\delta\nu_i^{A,A'}$, are related to the nuclear Seltzer moment, $\lambda^{AA'}$ as follows,

$$\delta\nu_i^{A,A'} = \frac{A' - A}{AA'} M_i + F_i \lambda^{AA'}. \tag{5.14}$$

In order to extract $\lambda^{AA'}$ it is necessary to determine values for the atomic factors F_i and M_i. For many transitions, determining F_i is incredibly difficult due to the non-trivial task of calculating the change in electron charge density at the nucleus which requires detailed knowledge of the electron wavefunction. King [1] developed a graphical method for determining the electronic factors using empirical measurements. The technique, known as a King plot, involves plotting a set of modified optical isotope shifts against modified values for the change in Seltzer moments between the same isotope pairs. The plotted values are modified by multiplication with a modification factor,

$$\mu^{AA'} = \frac{AA'}{A - A'} \mu_{ref}, \tag{5.15}$$

where μ_{ref} is a constant reference factor, used to maintain the order of magnitude of $\delta\nu_i^{A,A'}$, that is evaluated as follows,

$$\mu_{ref} = \frac{A_{ref} - A'_{ref}}{A_{ref} A'_{ref}}. \tag{5.16}$$

Multiplying both sides of equation 5.4.1 by the modification factor, $\mu^{AA'}$, removes the isotopic dependency in the equation as follows,

$$\mu^{AA'} \delta\nu_i^{A,A'} = \frac{A' - A}{AA'} \mu^{AA'} M_i + F_i \mu^{AA'} \lambda^{AA'} \tag{5.17}$$

$$\mu^{AA'} \delta\nu_i^{A,A'} = \frac{A_{ref} - A'_{ref}}{A_{ref} A'_{ref}} M_i + F_i \mu^{AA'} \lambda^{AA'}. \tag{5.18}$$

The gradient and intercept of a King plot of $\mu\delta\nu_i^{A,A'}$ against $\mu\lambda^{AA'}$ are therefore equal to F_i and $\frac{A_{ref} - A'_{ref}}{A_{ref} A'_{ref}} M_i$ respectively.

By plotting Seltzer moments determined from combined muonic and electron scattering data, $\lambda_{\mu e}^{AA'}$, in a King plot with optical isotope shifts, accurate F_i and M_i values can be determined. Seltzer moments for each optically measured isotope shift can then be calculated using equation 5.4.1 and the new values for F_i and M_i.

Table 5.7 below displays the isotope shift ($\delta\nu_{IS}^{A,A'}$) values for the 349.8942nm transition in ruthenium measured during this work and Seltzer moments of ruthenium obtained from muonic atom spectroscopy[38]. Also displayed in table 5.7 are modified isotope shifts and Seltzer moments obtained using modification factors calculated with equation 5.15 and reference masses $A_{ref} = 104$ and $A'_{ref} = 102$.

A'	A	μ	$\delta\nu_{IS}^{A,A'}(MHz)$	$\lambda^{AA'}(fm^2)$	$\mu\delta\nu_i^{A,A'}(MHz)$	$\mu\lambda^{AA'}(fm^2)$
101	100	1.90	-77.2(19)	0.0707(41)	-146.9(36)	0.1346(78)
99	98	1.83	-103.9(16)	0.1013(68)	-190.0(30)	0.185(12)
98	96	0.89	-396.1(17)	0.2649(68)	-351.3(15)	0.2349(60)
104	102	1.00	-346.6(18)	0.2515(48)	-346.6(18)	0.2515(48)
100	99	1.87	-232.2(18)	0.1626(96)	-433.4(33)	0.304(18)
102	101	1.94	-248.4(20)	0.1731(63)	-482.5(38)	0.336(12)

Table 5.7: Isotope shifts for the 349.8942nm transition in ruthenium along with Seltzer moments[38] and modified values

Figure 5.9 below displays the King plot obtained by plotting the modified isotope shifts against the modified Seltzer moments displayed in table 5.7. A linear fit to the data points in figure 5.9 provides values for the gradient and intercept of F_i=-1826(200)MHzfm^{-2} and $\mu_{ref}M_i$=105(48)MHz respectively. Not all of the data points fall on the straight line fit to the data. However, substituting the measured isotope shift values from table 5.7 along with the transition factors F_i and M_i obtained from the King plot into equation enables new accurate Seltzer moments (based upon both muonic and laser spectroscopy data) to be calculated.

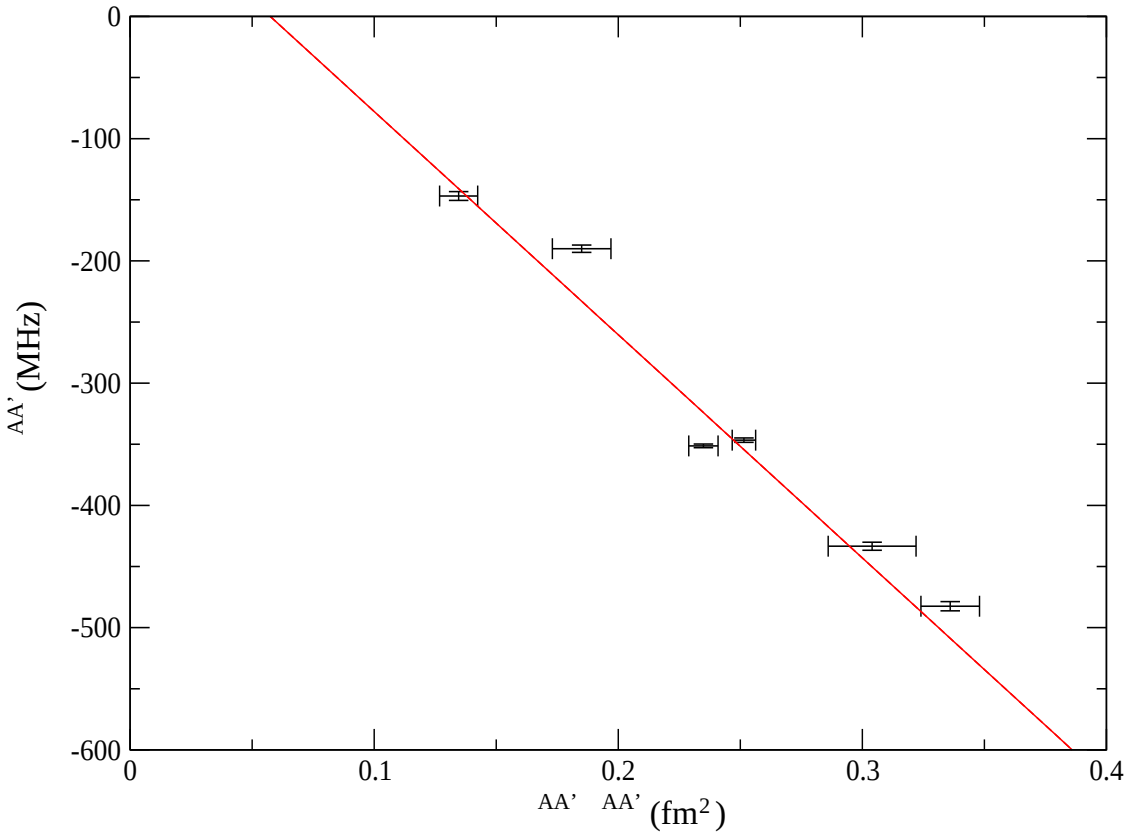

Figure 5.9: King plot of modified isotope shift values versus modified Seltzer moments for the 349.8942nm transition in atomic ruthenium

Finally, the change in mean-squared charge radius between isotopes, $\delta\langle r^2\rangle^{A,A'}_{o\mu e}$, can be determined by removing the contribution from higher order moments using equation 2.25 which is repeated below for convenience,

$$\lambda^{AA'} = \delta\langle r^2\rangle^{A,A'} + \frac{C_2}{C_1}\delta\langle r^4\rangle^{A,A'} + \frac{C_3}{C_1}\delta\langle r^6\rangle^{A,A'} + \ldots, \tag{5.19}$$

where values for the Seltzer coefficients are available from literature [39]. The higher order radial moments can be determined from the electron scattering and muonic atom data.

5.4.2 Ruthenium

For ruthenium there is an extremely limited set of experimental data available. Fricke et al.[38] lists a set of Barrett equivalent radii obtained from muonic atom experiments. Fricke et al. also reports that, up to 2004, no electron scattering or K X-ray experimental data exist for ruthenium. A literature review by the author of this work has confirmed that there has been no change to this situation before the completion of this work. It

is therefore not possible to produce a set of Seltzer moments by combining the values of electron and muon experiments. Fricke et al. presents a set of Seltzer moments determined from the muonic atom data only.

It is also the case that prior to this work there was very little optical isotope shift data for ruthenium. The only optical isotope shift data available is for a single transition measured using a hollow-cathode experiment [10]. Fricke used the combined analysis technique to obtain values of $\delta\langle r^2\rangle^{A,A'}$ by combining $\lambda_{\mu}^{AA'}$, obtained from muonic data, and $\delta\nu_i^{A,A'}$, obtained via optical hollow-cathode work, in a King plot. The Fricke et al. $\delta\langle r^2\rangle^{A,A'}$ values are displayed in table 5.8.

A'	A	$\delta\langle r^2\rangle^{A,A'}(10^{-3}fm^2)\ddagger$	$\delta\langle r^2\rangle^{A,A'}(10^{-3}fm^2)\dagger$	$\delta\langle r^2\rangle^{A,A'}(10^{-3}fm^2)^\star$
98	96	287.4(20)	288.3(20)	281(23)
100	98	253.8(21)	253.5(21)	263.9(93)
102	100	244.2(25)	244.2(25)	245(15)
104	102	255.0(17)	254.9(17)	256(21)
99	98	91.7(15)	91.5(16)	98.8(93)
101	100	73.7(18)	73.7(18)	71.3 (76)

Table 5.8: Final $\delta\langle r^2\rangle^{A,A'}$ results‡ determined from the weighted mean of the twelve analysed transitions.† indicates the $\delta\langle r^2\rangle^{A,A'}$ weighted mean not including the 298.8947nm transition results. The $\delta\langle r^2\rangle^{A,A'}$ results produced by Fricke et al.⋆[38] are also provided for comparison.

The Seltzer moments determined by Fricke et al.[38] were used to produce a King plot for each of the optical transitions measured during this work. The King plot was fitted by a linear regression method in order to determine values for the electronic factors F_i and M_i (tabulated in appendix A) and the uncertainty of each value. A combined optical and muonic atom value for the Seltzer moment, $\lambda_{o\mu}^{AA'}$, was then obtained using equation 5.4.1 with the extracted F and M values and the isotope shifts in table 5.3. The contributions of the higher order moments to the Seltzer moment were evaluated using muonic atom data published by Fricke et al.[38] and subtracted in order to determine $\delta\langle r^2\rangle^{A,A'}$ for each transition. The combined analysis values for $\delta\langle r^2\rangle^{A,A'}$ obtained for each measured laser spectroscopy transition are displayed in appendix A.

Table 5.8 contains the weighted mean value of $\delta\langle r^2\rangle^{A,A'}$ for the 12 transitions. On initial inspection of the $\delta\langle r^2\rangle^{A,A'}$ data presented in appendix A it would seem that the 298.8947nm transition data is notably different to the other transitions. However, per-

forming a standard t-test[40] reveals that the 298.8947nm transition $\delta\langle r^2\rangle^{A,A'}$ values are consistent with a distribution centred upon the weighted mean $\delta\langle r^2\rangle^{A,A'}$ values of the other eleven transitions. Table 5.8 also includes the weighted mean value of $\delta\langle r^2\rangle^{A,A'}$ for the eleven transitions other than the 298.8947nm transition. The two weighted mean values agree, considering errors, indicating that it is acceptable to include the 298.8947nm transition in the final weighted mean calculation of $\delta\langle r^2\rangle^{A,A'}$.

The error on the weighted mean of the full set of twelve transition values for $\delta\langle r^2\rangle^{A,A'}$ is an order of magnitude smaller than the error on Fricke's $\delta\langle r^2\rangle^{A,A'}$ values. Figure 5.10 below shows a King plot of the isotope shifts obtained from the 349.8942nm transition plotted against the MSCR obtained by Fricke et al. and also the final weighted mean $\delta\langle r^2\rangle^{A,A'}$ values obtained from this work. The χ^2 per degree of freedom of the line fit is more favourable for the plot versus the weighted mean obtained from this work. This suggests that the new weighted mean values are more accurate than the Fricke et al. values that are based upon only one optical transition. This is due in part to the large number of transitions that were used to evaluate the values in table 5.8 but is also because the isotope shift measurements obtained from laser spectroscopy measurements are considerably more accurate than those obtained from hollow-cathode experiments used by Fricke et al.

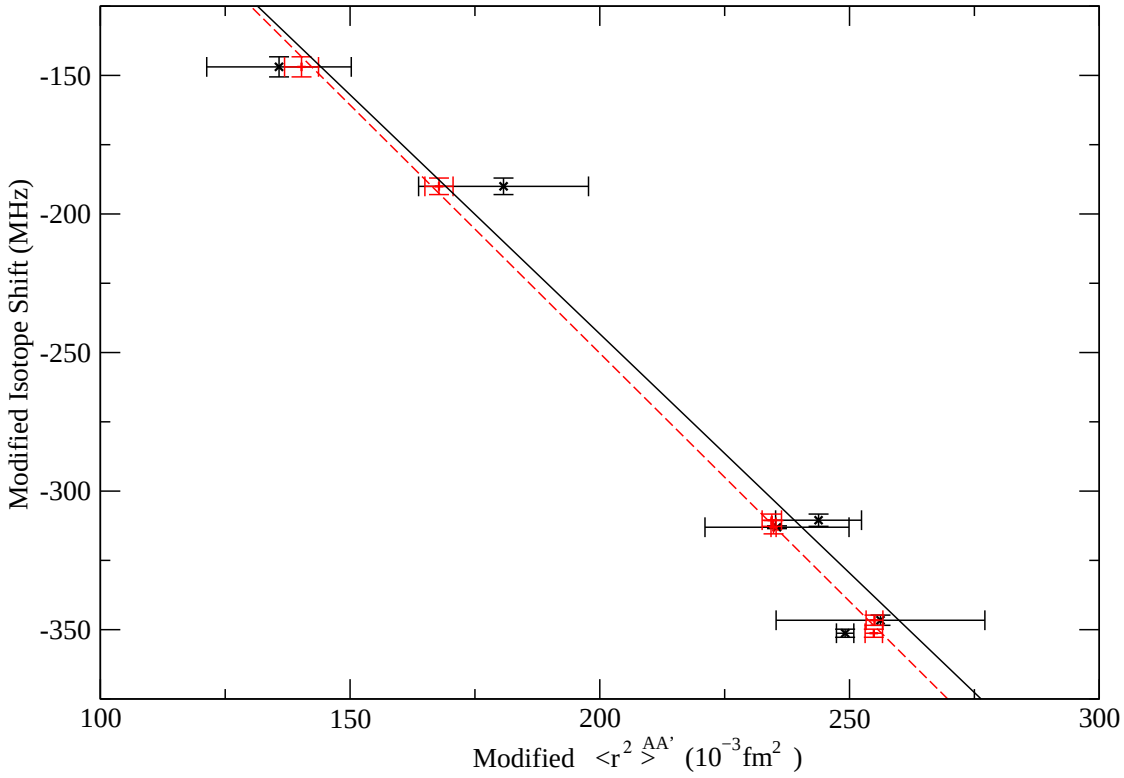

Figure 5.10: King plot of measured isotope shifts from the 349.8942nm transition plotted against $\delta\langle r^2\rangle^{A,A'}$ values from this work (+, dashed-red trace) and values published by Fricke et al.[38] (x, solid-black trace).

5.4.3 The R6G transitions

The isotope shifts displayed in table 5.3 do not include the majority of the transitions measured using R6G in the 296 – 310nm wavelength region. This is due to the fact that, as discussed previously in this chapter, the majority of these transitions exhibit extremely small isotope shifts resulting in very narrow spectra. As the spectra are very narrow many of the peaks are very close together and difficult to accurately resolve. This results in larger errors for the fitted isotope shifts than those displayed in table 5.3. The combination of small isotope shifts and large errors on those isotope shifts leads to relatively high percentage errors for these transitions. When plotted as a King plot the narrow spacing of data points and the large error bars makes it very difficult to determine reliable values for F_i and M_i. This effect is illustrated below for the 304.0314nm and 343.6736nm transitions. The data points in the 304.0314nm transition King plot, figure 5.11a, are considerably more bunched than those in the equivalent plot for the 343.6736nm (figure 5.11b), however, both plots have similar sized error bars.

For this reason it was not possible to extract sensible $\delta\langle r^2\rangle^{A,A'}$ values for the majority

of the transitions in the 296 – 310nm range. These transitions are therefore not included in the weighted-mean final $\delta\langle r^2\rangle^{A,A'}$ values presented in table 5.8.

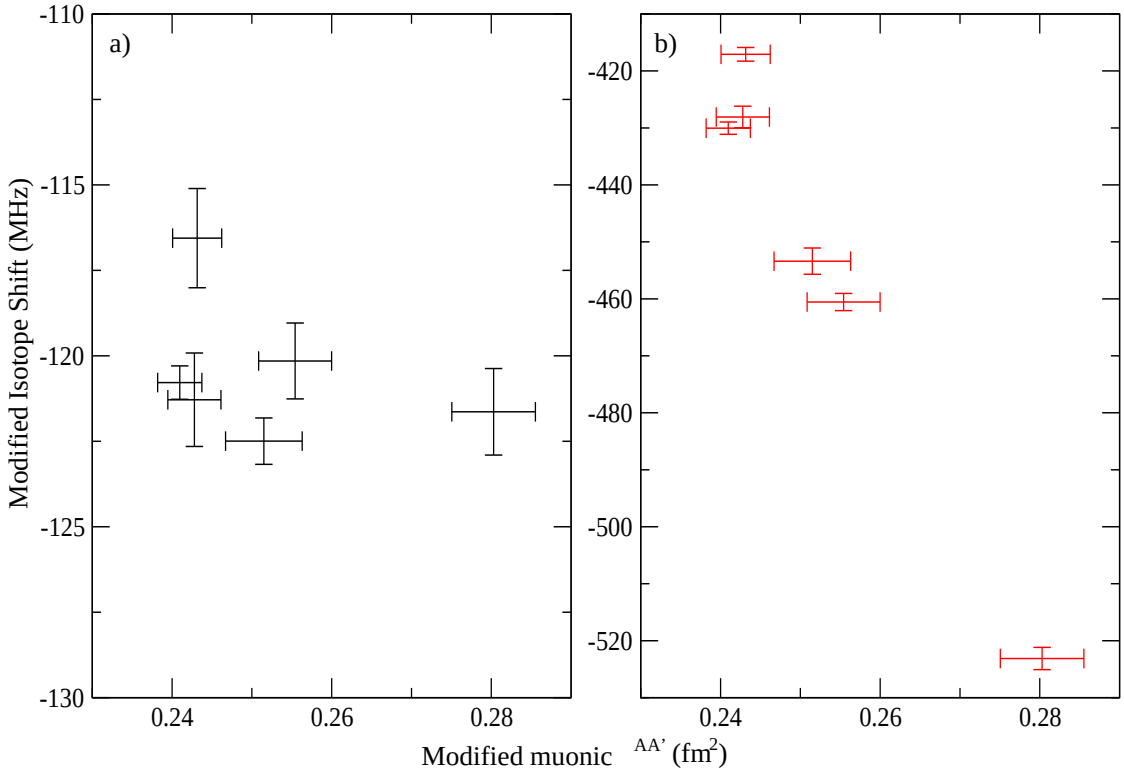

Figure 5.11: King plot of measured isotope shifts against muonic Seltzer moments, $\lambda_\mu^{AA'}$ for a) the 304.0314nm transition and b) the 343.6736nm transition. Note change of scale on y-axis.

Chapter 6

Interpretation of Results and Consequences for Future Work

Whilst crossed beam laser spectroscopy is ideal for the study of stable isotopes, collinear laser spectroscopy is more appropriate for the measurement of the ground and isomeric state properties of radioactive isotopes. As outlined in chapter 3, the collinear laser spectroscopy technique is able to successfully measure resonant spectra for small samples of atoms or ions and hence is ideal for the study of short-lived radioactive isotopes. This chapter will discuss the collinear laser spectroscopy method in more detail before assessing the consequences of the data obtained during this work for future measurements.

6.1 Collinear Laser Spectroscopy

As discussed in section 3.2.2, in collinear laser spectroscopy a beam of ions or atoms interacts with a laser beam travelling along a common axis. Collinear laser spectroscopy experiments are mainly performed at three experimental facilities around the world; JYFL (Finland), ISOLDE (CERN) and TRIUMF (Canada). Currently, only the IGISOL facility at JYFL is capable of producing beams of ruthenium atoms or ions. This is because the IGISOL radioactive beam production method is independent of the reactive or refractory nature of the element being produced[41, 42]. For other beam production methods the beam yield[43] is highly dependent upon these element properties and highly refractive elements such as ruthenium cannot be extracted. For this reason the equipment and techniques discussed during this chapter are specific to the JYFL experi-

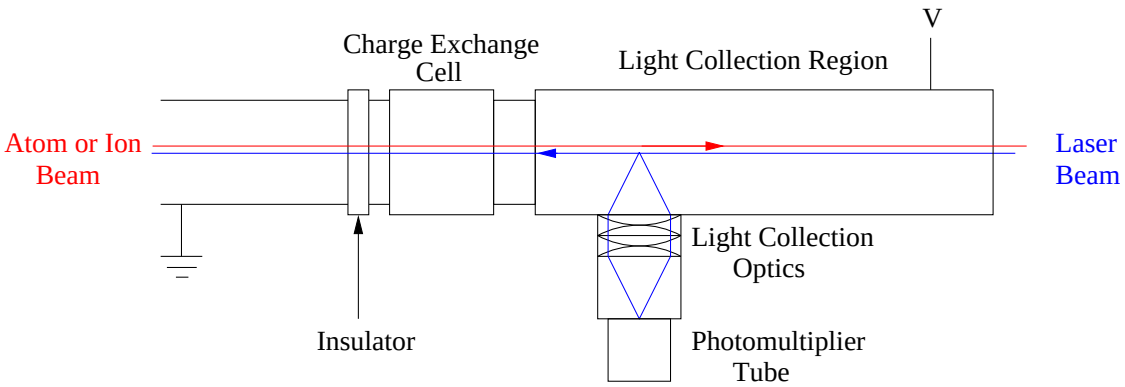

Figure 6.1: Schematic of a collinear laser spectroscopy line.

ment.

Figure 6.1 displays a schematic diagram of the charge exchange and light collection section of the collinear laser spectroscopy line, built by a collaboration between the University of Birmingham and the University of Manchester, at JYFL. Resonant photons emitted by atoms or ions travelling in front of the PMT are focused onto the PMT photocathode for detection. In order to measure a resonance spectrum it is necessary to scan the laser frequency observed by the ion or atom beam in a controlled manner. This is achieved by holding a section of the beam line, known as the light collection region (LCR), at high voltage which is used to electrostatically accelerate (or decelerate) the ion beam towards the laser. By ramping the acceleration voltage up and down the Doppler shifted laser frequency observed by the ion beam is also scanned in a controlled manner. The Doppler shifted laser frequency, ν, that is observed by the ion beam is related to the acceleration voltage, V, as follows,

$$\nu = \nu_L[1 + \alpha + \sqrt{\alpha^2 + 2\alpha}], \tag{6.1}$$

where $\alpha = \frac{eV}{Mc^2}$, M is the mass of the ion and ν_L is the unshifted laser frequency. When the Doppler shifted laser frequency matches the transition frequency of the ions resonance occurs and fluorescent photons are emitted.

6.1.1 Unwanted optical pumping effects

When the ion or atom beam is accelerated onto resonance with the laser beam stimulated absorption excites electrons from the transition lower state E_1 to the upper state E_2. Electrons in the upper state are then free to relax, by spontaneously emitting a photon,

to either E_1 or any other allowed state E_i. As discussed in section 4.4.1, the parity of E_1 and E_i must be the same and so further optical relaxation of an electron in state E_i to state E_1 is not allowed. An atom that relaxes into a lost state E_i can therefore no longer interact with the laser and produce fluorescent photons. Equation 6.2 allows the number of spontaneously emitted photons, N_γ, produced prior to falling into a lost state to be calculated,

$$N_\gamma = 1 + \frac{A_{21}}{\sum_{i\neq 1} A_{2i}}, \tag{6.2}$$

where (as in section 4.4.1) A_{21} is the rate of spontaneous emission from E_2 to E_1 and $\sum_{i\neq 1} A_{2i}$ is the sum of spontaneous emission rates from state E_2 to all accessible lost states E_i. If $\sum_{i\neq 1} A_{2i} \gg A_{21}$ the number of spontaneously emitted photons per atom or ion tends towards one. This has direct consequences for the efficiency of collinear laser experiments as if the atom or ion relaxes into a lost state prior to crossing in front of the PMT no fluorescent photons will be detected. In ionic beam experiments the acceleration voltage can be tuned so that the ion beam comes onto resonance in front of or very close to the PMT. This ensures that, even when $\sum_{i\neq 1} A_{2i}$ is high, fluorescent photons will be emitted by the ion beam as it crosses in front of the PMT.

This type of tuning cannot be performed for atomic beams. In order to perform collinear laser spectroscopy on atomic beams a charge exchange cell is positioned in the beam line before the LCR (see figure 6.1) to neutralise the incident ion beam. It is necessary to accelerate the ion beam to the atomic resonance velocity prior to entering the charge exchange cell as those ions that are neutralised into atoms can no longer be electrostatically accelerated. The atomic beam is therefore on resonance with the laser beam from the charge exchange cell onwards. If $\sum_{i\neq 1} A_{2i} \gg A_{21}$ there is a high probability that the majority of the atoms in the atomic beam will be optically pumped into a lost state prior to crossing in front of the PMT.

The negative effect of unwanted optical pumping upon detection efficiency has been experimentally observed at ISOLDE for investigations of atomic gallium[44]. The COLLAPS collinear experiment at ISOLDE has successfully measured the 0 – 30535.3cm^{-1} transition in copper[45] and 0 – 24788.6cm^{-1} in gallium[46]. Both transitions have high A-coefficients however the gallium transition initially suffered from poor efficiency.

The poor experimental efficiency of gallium can be understood by considering equa-

tion 4.13. Figure 6.2 displays the change in the number of photons emitted by an atom as it travels on resonance down the beam line for transitions in atomic gallium (Ga I) and copper (Cu I). The number of emitted photons per atom was calculated using equation 4.13 where N_2 was evaluated by numerically integrating the coupled equations 4.11 and 4.12 with respect to time. The time intervals were then converted to distance travelled by using typical acceleration voltages to calculate the beam velocity.

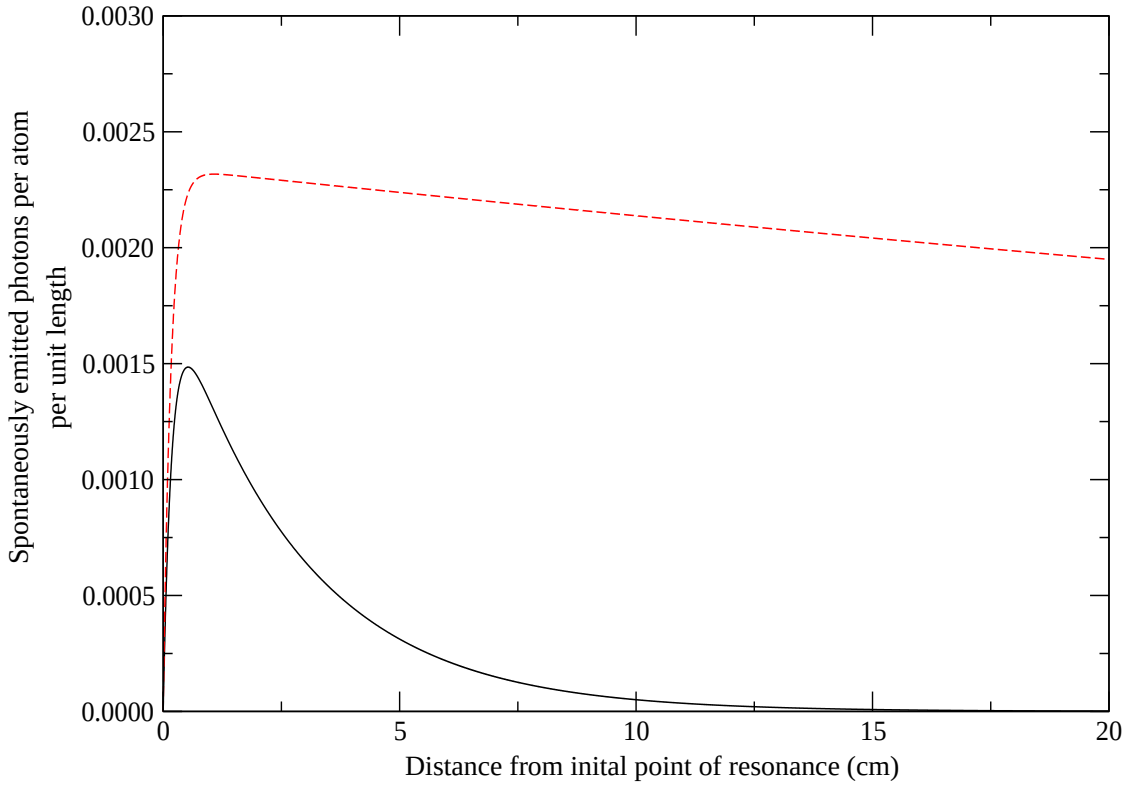

Figure 6.2: Graph comparing the calculated number of photons emitted per atom per length increment ($\simeq 0.0035$cm) as a function of distance travelled for the Cu I, 0 – 30535.3cm^{-1} (red dashed trace) and the Ga I, 0 – 24788.6cm^{-1} (black solid trace) transitions.

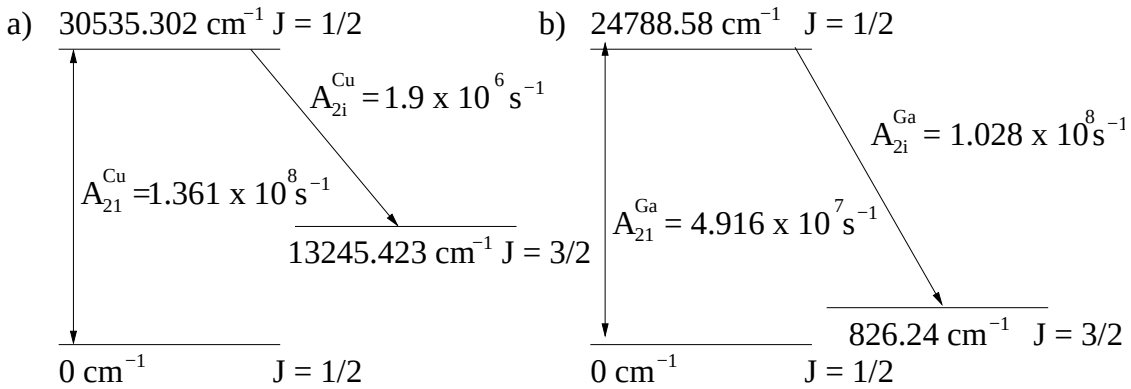

Figure 6.3: Energy level diagrams for a) Cu I, 0 – 30535.3cm^{-1} transition, b) Ga I, 0 – 24788.6cm^{-1} transition.

The Cu I 0 – 30535.3cm^{-1} transition (see figure 6.3a) has a high transition A-coefficient A_{21}^{Cu} = 1.361$\times$ 10^{8}s^{-1} and only one allowed lost state transition with A-coefficient A_{2i}^{Cu} = 1.9$\times$ 10^{6}s^{-1}. As A_{21}^{Cu} is two orders of magnitude greater than A_{2i}^{Cu} limited pumping occurs as the atom beam travels down the beam line. This results in a gradual reduction in the number of photons emitted per atom from the initial point of resonance onwards.

The gallium 0 – 24788.6cm^{-1} transition (see figure 6.3b) also has only one allowed lost state transition however its A-coefficient, A_{2i}^{Ga} (= 1.028$\times$ 10^{8}s^{-1}), is nearly twice the size of the transition A-coefficient A_{21}^{Ga} (= 4.916$\times$ 10^{7}s^{-1}). For this transition there is a high probability that the upper state will relax into the lost state. The longer the interaction time on resonance with the laser beam the more atoms will be pumped out of the ground state and therefore be unavailable for the production of fluorescent photons. For a charge exchange cell positioned approximately 20cm away from the PMT the Ga I transition will exhibit significant amounts of unwanted optical pumping into lost states prior to reaching the PMT. In fact a small fluorescent signal would be produced as confirmed by the experiments at ISOLDE[44]. In comparison, the Cu I transition suffers only moderate amounts of optical pumping and a significant fluorescent signal would be produced at the PMT.

Successful measurement of gallium was eventually achieved by reducing the power density of the laser beam (by reducing the laser power and expanding the width of the beam)[44]. Reducing the power density of the beam reduces the rate at which atoms are excited to the transition upper state and hence ensures that a significant number of atoms are available to produce fluorescent photons at the PMT. This is, however, a compromise as reducing the laser power will reduce the number of fluorescent photons produced whilst crossing the PMT. The effect of unwanted pumping into optical states should be considered when selecting a transition to use for a collinear experiment.

6.1.2 Locking the Laser Frequency

In a collinear laser spectroscopy experiment at JYFL the laser frequency is scanned by accelerating ions towards a laser of fixed frequency. In order to ensure that the spectrum measurements are accurate and reproducible it is necessary to ensure that the laser frequency is held fixed for the duration of a measurement. Due to the small radioactive

beam fluxes used, collinear laser spectroscopy measurements often take many hours to complete. It is therefore necessary to employ active frequency locking techniques in order to ensure that laser frequency drift is minimised. For experiments at the University of Jyväskylä (JYFL), this is achieved using two servo-loop systems that are capable of keeping the laser frequency "locked" to within 2MHz of the desired frequency for long periods of time [20].

The first servo loop is provided by the Spectra-Physics Stabilok device. The Stabilok consists of a "reference" etalon and a "slave" etalon with FSR's of 500MHz and 8GHz respectively. The "reference" and "slave" etalons are tuned so that the laser frequency is aligned with a transmission peak in each etalon. The "reference" etalon is tuned so that the laser frequency is aligned at approximately half the maximum of a transmission profile whereas the "slave" etalon is aligned to approximately a third of the maximum transmission profile. The light transmitted through each etalon is measured using a photodiode. If the laser frequency drifts, the intensity of the light transmitted through the etalons will increase or decrease depending on which way the frequency is changing (see figure 6.4).

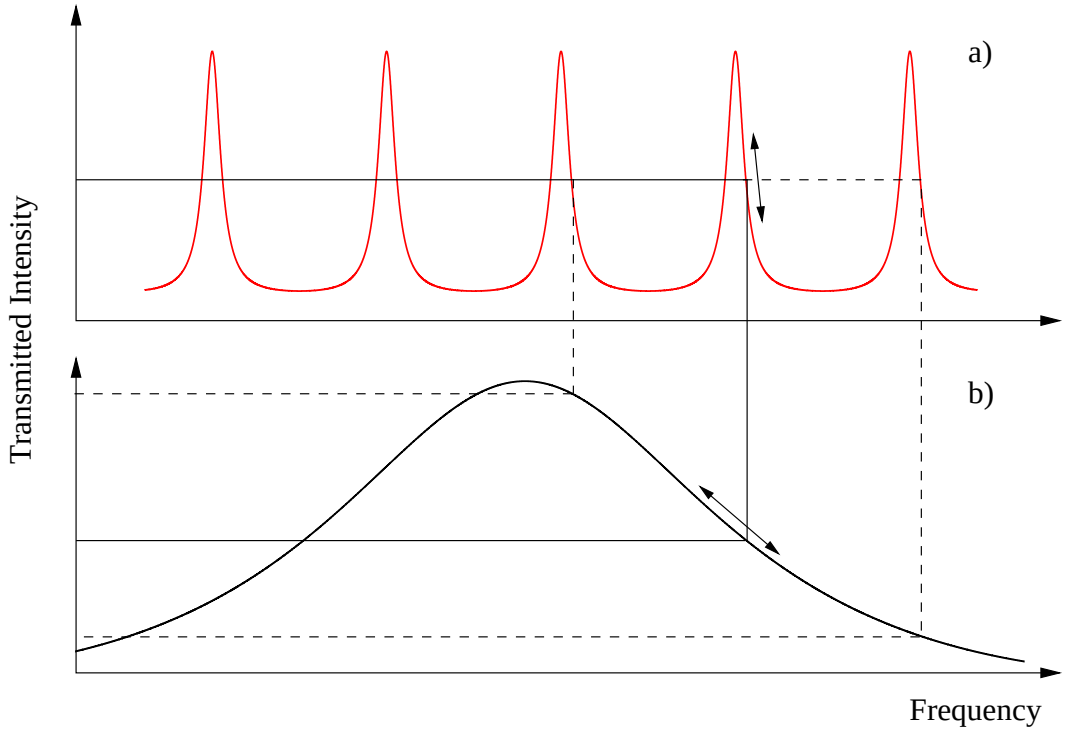

Figure 6.4: The transmission profiles for the Stabilok a) "reference" and b) "slave" etalons showing the desired laser frequency (vertical solid line) and the laser frequency following a mode hop (vertical dashed line).

The locking system then acts to drive the laser frequency back to the half-maximum

position on the "reference" etalon. If a mode hop occurs such that the laser leaves the transmission peak of the "reference" etalon, the "slave" etalon is used to retrieve the laser frequency. This is possible due to the large FSR and low finesse of the "slave" etalon which makes it highly unlikely that the laser will hop off the selected transmission peak (see figure 6.4). The Stabilok provides a frequency lock that is limited by the stability of the transmission peaks of the etalon. However, the etalon peaks are prone to drifting over long periods of time according to temperature and atmospheric fluctuations. If the FSR of the etalons varies then the laser frequency will drift even if it maintains the same position on the etalon transmission profiles. The second servo loop eliminates this limitation by comparing the laser frequency to an absorption line in molecular iodine that provides an absolute frequency reference.

The laser frequency is tuned to the minimum of an iodine absorption line. When the Stabilok is activated, a glass plate in the centre of the "reference" etalon oscillates and so changes the optical length of the etalon. This changes the FSR of the "reference" etalon which causes the transmitted intensity of the laser to oscillate. The Stabilok locking system then adjusts the laser frequency to correct for the change in transmission intensity. This results in the laser frequency oscillating about the minimum of the iodine line by $\sim$ 1 MHz. The iodine cell transmission profile is then compared to the oscillation frequency of the laser in a phase sensitive detector (PSD) in a manner comparable to that illustrated in figure 4.11. If the laser frequency deviates from the base of the iodine line an error signal is generated and sent to the "reference" etalon so as to correct the laser frequency. Molecular iodine is chosen as it possesses a large number of absorption lines over a wide range of wavelengths. This ensures that for the majority of transitions in the element being studied there is a suitable iodine line nearby that can be used as a frequency reference for locking.

6.1.3 Atomic or Ionic Laser Spectroscopy

Collinear laser spectroscopy can be performed using either atomic or ionic beams provided that an appropriate optical transition can be found in the chosen beam type. The electric dipole transitions stimulated during laser spectroscopy require that there is a change in parity between the transitions' lower and upper energy levels. For atomic ruthenium, the ground state multiplet of energy levels have even parity and the lowest

energy odd parity state is at 25214cm^{-1}[47]. The resulting allowed electric dipole transitions from the ground state multiplet have a range of wavelengths from 207 – 412nm. This work has demonstrated that a large number of these transitions can be measured by a dye laser and a frequency doubling crystal.

For ionic ruthenium, the energy levels in the ground state multiplet also have even parity, however the lowest energy odd parity state is at 46471cm^{-1}[47], a considerably higher energy than the equivalent in atomic ruthenium. As a result the allowed electric dipole transitions in ionic ruthenium have the wavelength range 147 – 202nm. These wavelengths are very challenging to produce, with the power and line widths required for efficient high resolution laser spectroscopy. Also, for sub-200nm UV wavelengths absorption of the laser beam by air molecules becomes significant which would cause considerable laser beam losses during steering from the dye-laser cavity to the ion beam line.

At thermal energies only the ground state multiplet of a ruthenium atom or ion is sufficiently populated for use in laser spectroscopy experiments. However, previous collinear experiments[8, 48] have utilised optical pumping techniques to enable the successful measurement of transitions from high-lying metastable energy levels. Optical pumping uses a tunable laser to excite electrons from the thermally populated ionic/atomic low-lying energy levels into a high-lying energy state. The high-lying energy state then relaxes to a number of intermediate states and enhances their population. Laser spectroscopy can then be performed from these newly populated states. A more detailed description of this process is given by B. Cheal[8] and in the PhD thesis of K. A. Baczynska[49]. In ionic ruthenium optical pumping would prove challenging as the initial pump stage would still require a pump laser beam capable of producing decent amounts of power in the 147 – 202nm wavelength range. For this reason any future work involving ruthenium is likely to be carried out on atomic ruthenium which makes the data measured for this work even more significant.

6.2 Suitable transitions for collinear spectroscopy

As discussed in section 3.2.2 collinear laser spectroscopy experiments require large and complex equipment that is often located at international experimental facilities. Prior to conducting a collinear experiment with radioactive beams at such a facility it is usual

to perform a number of optical tests using stable ionic or atomic beams to determine the optimum optical transitions and experimental set-up required for a successful measurement. These tests, known as offline runs, can be time consuming. During this work a significant number of the transitions in stable atomic ruthenium have been measured using crossed-beam spectroscopy (see table 4.3). This data can be used to select efficient optical transitions and the necessary laser conditions required to measure them. This removes the need for significant offline testing and in doing so saves a considerable amount of time that can be used for online radioactive experiments.

Before this work, an initial assessment of the transition properties outlined in table 4.3 suggests that the atomic ruthenium transitions in the 295 – 310nm wavelength region seem ideal for use in collinear laser spectroscopy work as they have high ($\sim 10^7 \mathrm{s}^{-1}$) transition strengths. These transitions also coincide with the output wavelength range of the frequency doubled laser dye rhodamine-6G (R6G). R6G is commonly used in laser spectroscopy experiments due to its ability to produce beams with good power over a wide range of wavelengths from 560 – 650nm (or 280 – 325nm after frequency doubling). However, the study of these transitions in the R6G region for this work has revealed that they exhibit extremely narrow spectra with small optical isotope shifts (all measured spectra are displayed in appendix C) which prevented the extraction of nuclear parameters. Collinear laser spectroscopy measurements are able to use mass selected ion beams so that they can measure the structure associated with each isotope separately. This would enable, particularly for odd isotopes, the isotope shifts to be determined more easily than from atomic beam measurements where all isotopes are measured simultaneously which can result in the masking of weak structures. Despite this, the isotope shifts of these transitions are small and therefore unsuitable for forming King plots and extracting accurate $\delta\langle r^2 \rangle$ values (as discussed in section 5.4.3).

The other transitions measured for this work in the wavelength range 315 – 360nm all exhibit much more suitable isotope shifts for the extraction of $\delta\langle r^2 \rangle$ values (see table 5.3). Each of these transitions therefore could potentially be used in a collinear experiment. Transitions with a lower state other than the ground state would require some offline testing to check that they are sufficiently populated, after passage through the charge exchange cell, in order to generate a measurable quantity of resonant photons.

The 349.8942nm transition is the most promising transition for use in collinear work as its upper state only relaxes back to the ground state i.e. there are no allowed lost state

transitions from the upper state. The absence of lost state transitions means that an atom is free to recycle without loss between the transition states when passing through the laser beam at resonant velocity. Each atom therefore has the potential to produce several resonant photons for detection as it traverses the LCR. This transition therefore has the potential to be very efficient which enables the use of extremely weak atomic beams.

Conventionally, the transitions used for collinear laser spectroscopy experiments are often chosen so that the spins of the transition levels are as small as possible. This ensures that there are fewer hyperfine structure components to measure. Many of the transitions studied during this work, including the 349.8942nm transition, have high J values due to the high spin of the atomic ruthenium ground state multiplet. However, as the HF parameters for the transition lower states are known[36] and have been measured during this work for the upper states, the frequency of each hyperfine component can be estimated. This enables the acceleration voltages required to measure these components to be predicted (see section 6.2.2).

6.2.1 Suitable iodine locks for the 349.8942nm transition

Locking is performed using the fundamental output beam from the dye laser rather than the frequency doubled UV output beam. Therefore, in order to successfully use the 349.8942nm transition in a collinear experiment, suitable iodine absorption lines are required close to the fundamental laser wavelength of $\sim$699nm. An iodine atlas[30] can be used to search for suitable iodine absorption lines. The iodine atlas lists transitions according to wavenumber and uses units of cm^{-1}. It is therefore convenient to calculate the required locking frequency in terms of wavenumber. The 349.8942nm transition has wavenumber 28571.89cm^{-1} which corresponds to a fundamental wavenumber of 14285.945cm^{-1}.

Figure 6.5 displays a section of the iodine atlas[30] around 14285.945cm^{-1}. The dashed lines represent the locking wavenumber required in order for typical acceleration voltages to Doppler shift the ^{104}Ru isotope onto resonance. These values were calculated using equation 6.1 where ν_L is the laser locking wavenumber and ν is the transition resonance wavenumber. The iodine atlas lists six potential absorption lines that could be used as locking peaks with acceleration voltage around 30kV$\leq$V$\leq$40kV. These locking lines are listed in table 6.1 below.

	Voltage (V)		
Wavenumber(cm^{-1})	A=94	A=104	A=110
14273.07	35618	39407	41680
14273.65	32455	35907	37979
14273.97	30772	34045	36010
14274.05	30360	33589	35527
14274.55	27894	30861	32642
14274.83	26521	29343	31036

Table 6.1: Iodine absorption lines within 30 – 40kV acceleration voltage of the 349.8942nm transition resonance frequency along with the acceleration voltages for each line for different isotopes.

Also displayed in table 6.1 are the acceleration voltages required to kinematically Doppler shift various ruthenium isotopes, with mass number A, onto resonance with the locking lines. These voltages were calculated using the following equation,

$$\alpha = \frac{eV}{Mc^2} = \frac{(\nu - \nu_L)^2}{2\nu\nu_L}. \tag{6.3}$$

where, as for equation 6.1, ν is the transition frequency, ν_L is the locked laser frequency and M is the isotope mass.

Offline testing is required to test that the lines listed in table 6.1 are strong enough to be used for locking purposes. For wavelengths longer than 660nm the iodine absorption lines become progressively weaker and spaced further apart. For the crossed beam work conducted for this thesis the absorption profile of molecular iodine was used for frequency navigation (see section 4.3.1). For wavelengths >660nm the absorption lines were observed to be very weak but still visible using an oscilloscope. However, previous collinear laser spectroscopy measurements of yttrium[6, 27] at a wavelength of 363.3nm, suggests that it is possible to successfully lock to the iodine lines listed in table 6.1 in the vicinity of the shorter wavelength 349.8942nm ruthenium transition.

6.2.2 Predicting the position of radioactive isotopes' spectral lines

During collinear laser spectroscopy experiments the observed laser frequency is scanned over a range determined by the change in acceleration voltage. The acceleration voltage is ramped across a user specified range and a single spectrum measurement consists

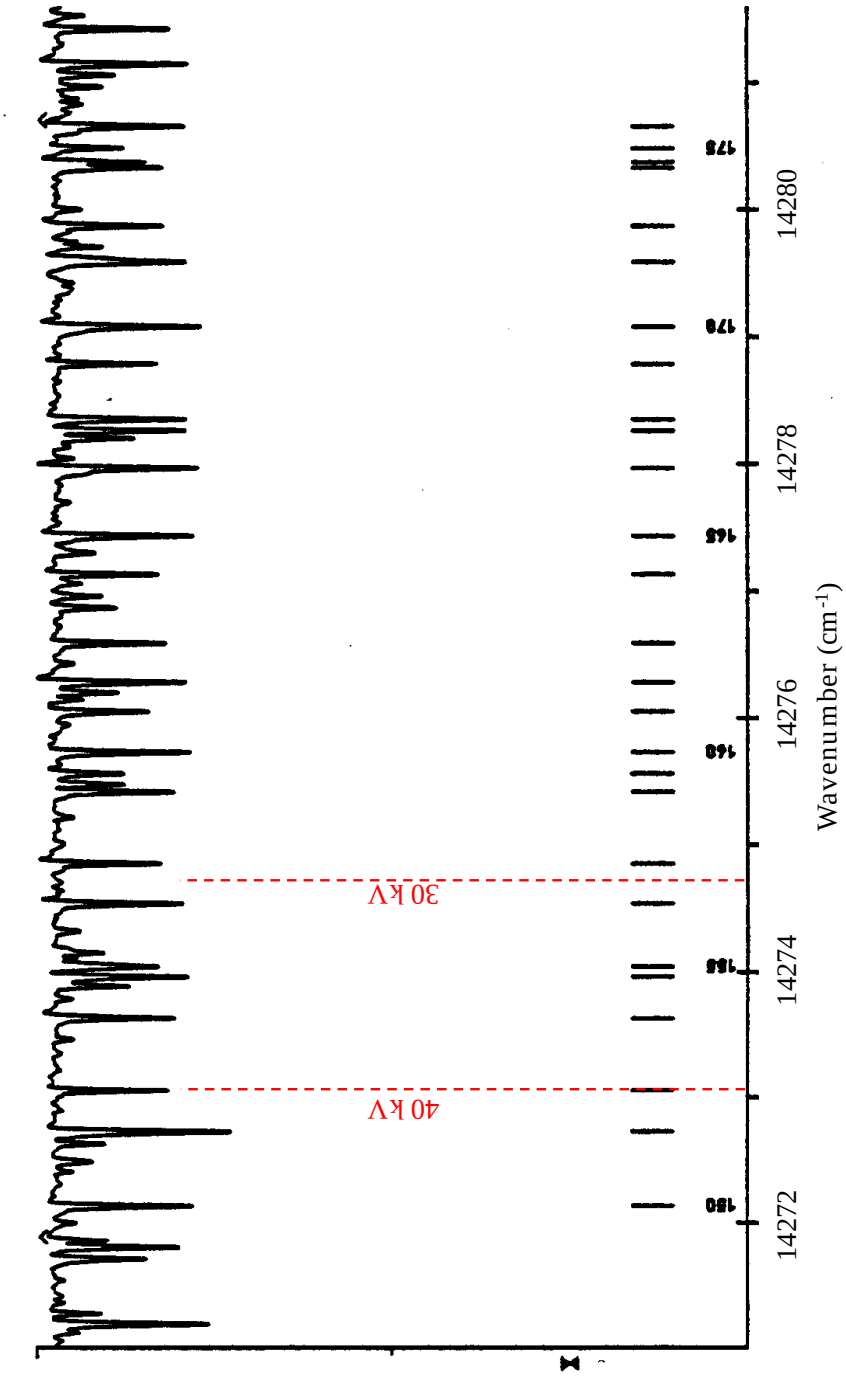

Figure 6.5: The absorption spectrum of molecular iodine in the vicinity of the 349.8942nm transition from *Atlas du Spectre D'Absorption de la Molecule d'Iode*[30]. The dashed lines show the locking laser frequency required for 40 kV and 30 kV acceleration voltages for ^{104}Ru.

of many repeat scans of the selected region. The stable isotopes can be produced in sufficiently large quantities that the fluorescence signal can be observed simply using a ratemeter. This enables the acceleration voltages of the stable isotopes to be easily determined for a given lock. However, the radioactive isotopes are produced in considerably smaller quantities and so do not produce sufficient fluorescent photons to be monitored in this manner. The acceleration voltages required to Doppler shift the unstable isotopes onto resonance can be determined by trial and error by performing scans over large regions ($\simeq$ 100V) in acceleration voltage space. However, such scans are time consuming and are likely to have poor resolution. Better quality scans are produced by scanning over smaller voltage regions ($\simeq$ 50V), however these type of measurements make it difficult to locate the unstable isotope resonances by trial and error. It is therefore extremely useful to predict the frequency at which the unstable isotopes occur relative to the stable isotopes prior to an experimental run. Good frequency predictions enable the acceleration voltages to be identified much more quickly.

An initial estimate for the acceleration voltage required to Doppler shift an unstable isotope onto resonance is obtained by calculating the kinematic shift using equation 6.3. This provides the acceleration voltage for an isotope assuming no isotope shift or hyperfine splitting. In reality this is not the case and a more accurate prediction is obtained by estimating the magnitude of the isotope shift and, for odd isotopes, the hyperfine structure. For ruthenium, the various atomic parameters measured during this work can be used to estimate the size of these effects.

The isotope shift, $\delta\nu_{IS}^{A,A'}$, can be calculated (see section 2.1) using equation 2.28 which is repeated below for convenience.

$$\delta\nu_{IS}^{A,A'} = \frac{A'-A}{AA'}M_i + F_i\delta\langle r^2\rangle^{A,A'} \tag{6.4}$$

During this work, values for the field and mass factors, F_i and M_i respectively, have been determined for a number of transitions (see table A.3). Therefore, in order to estimate the isotope shift for an unstable isotope A using equation 6.4 the only unknown parameter is the change in mean-square charge radius (MSCR), $\delta\langle r^2\rangle^{A,A'}$. Values for $\delta\langle r^2\rangle^{A,A'}$ can be estimated by considering the charge radii systematics of the element and also neighbouring elements. For ruthenium, new accurate measurements of $\delta\langle r^2\rangle^{A,A'}$ for the stable isotopes have been determined during this work via the combined analysis method

(see table 5.8). These values, rearranged to give the change in MSCR relative to the 104 isotope (N=60), are plotted against neutron number N in figure 6.6. The increase in $\delta\langle r^2\rangle^{60,N}$ with neutron number is approximately linear across the stable ruthenium isotopes with odd-even staggering (OES) observed between adjacent isotopes. Assuming a linear relationship between $\delta\langle r^2\rangle^{A,A'}$ and A enables $\delta\langle r^2\rangle^{A,A'}$ values to be estimated for the unstable isotopes near or in between the stable isotopes. Fitting a linear relationship does not allow the effect of OES in $\delta\langle r^2\rangle^{A,A'}$ to be predicted. However for ruthenium the magnitude of this effect is small and contributes only a small change to the applied acceleration voltage. For example, for the 349.8942nm transition OES causes the 101 isotope shift (relative to the 104 isotope) to differ from that predicted by a linear regression by $\simeq$ 82 MHz. This corresponds to a change in acceleration voltage of $\simeq$ 8 V which is within a typical experimental scan region.

In order to check the accuracy of isotope shift predictions for high-N unstable isotopes it is useful to compare the $\delta\langle r^2\rangle^{N',N}$ to neighbouring elements. For ruthenium the closest element with a large measured chain of $\delta\langle r^2\rangle^{N',N}$ is molybdenum, $Z = 42$. The known $\delta\langle r^2\rangle^{60,N}$ values for molybdenum[9] are plotted in figure 6.6. Like ruthenium, the $\delta\langle r^2\rangle^{60,N}$ of molybdenum increases linearly, except for some OES, across the $N = 50$ – 60 region. For $N > 60$ the $\delta\langle r^2\rangle^{60,N}$ of molybdenum begins to level off with increasing N, however the charge radii systematics of molybdenum are similar to the ruthenium linear extrapolation in this region. This similarity between experimental data and the linear extrapolation justifies the use of the extrapolation method for predicting isotope shifts in unstable ruthenium isotopes.

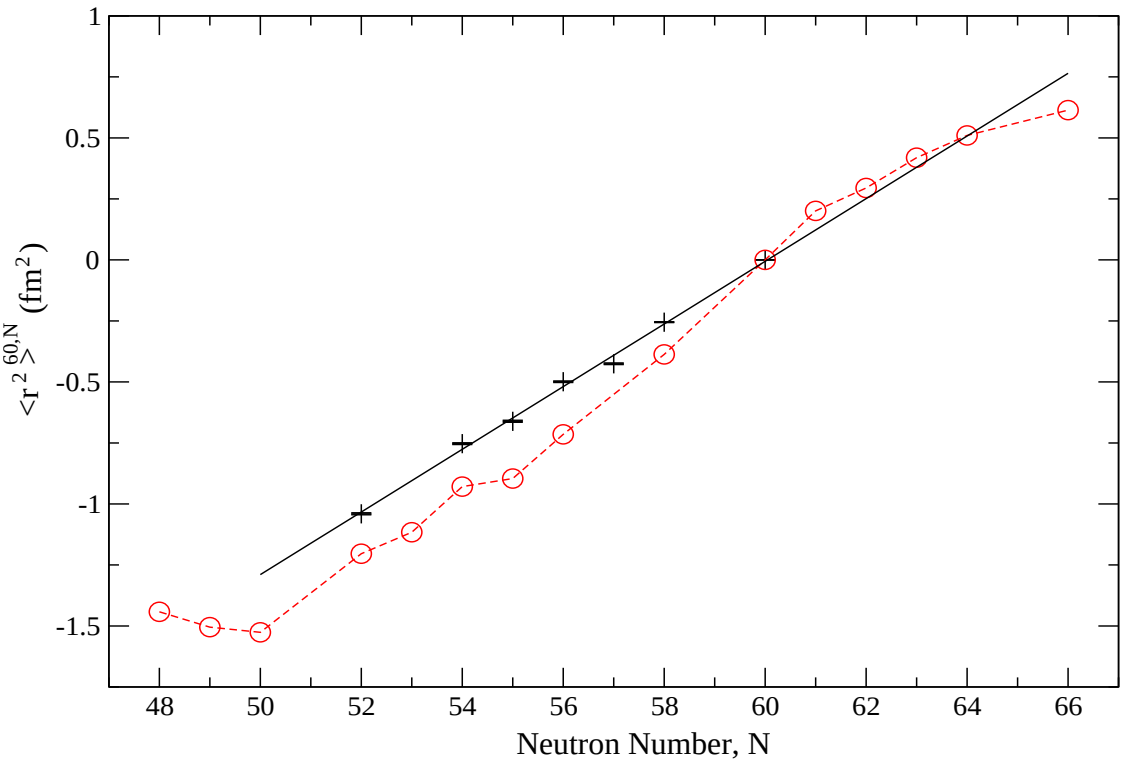

Figure 6.6: Change in $\langle r^2 \rangle$ systematics for ruthenium (+). The solid black line indicates a linear fit to the ruthenium data points. Also displayed is $\delta\langle r^2 \rangle^{60,N}$ for the neigbouring molybdenum isotope chain (o, red dashed line). Error bars are smaller than data points.

Odd mass number isotopes exhibit hyperfine structure which splits the spectrum line into a series of peaks (see section 2.2). Each hyperfine structure (HFS) line is related to the isotope centroid by equation 2.70. The isotope centroid can be estimated using the steps for predicting the isotope shift described above. In order to estimate the position of a HFS peak using equation 2.70 it is necessary to know the hyperfine parameters of the transition states. For the stable isotopes, ^{99}Ru and ^{101}Ru, the parameters for the ground state multiplet are known[36].The upper state parameters for several transitions have also been measured during this work and are displayed in table 5.4. The transition upper (U) and lower (L) state HF parameters of an unstable isotope (with mass number x) can be calculated using the standard scaling relations (outlined in section 2.4) as follows,

$$A^x_{U,L} = A^{99,101}_{U,L} \frac{(\mu/I)_x}{(\mu/I)_{99,101}}, \tag{6.5}$$

$$B^x_{U,L} = B^{99,101}_{U,L} \frac{Q_x}{Q_{99,101}}, \tag{6.6}$$

provided that the nuclear spin I_x, magnetic dipole moment μ_x and electric quadrupole moment Q_x of isotope x are known. Table 6.2 lists the currently measured[50] electro-

magnetic multipole moments for ruthenium. The magnetic dipole moments are known for four unstable isotopes however the signs are either unknown or tentatively assigned. By assuming that the unstable isotopes have the same negative sign as the stable 99 and 101 isotopes these values can be used in equation 6.5 to estimate the unstable isotope HF A-parameters.

A	I^{π}	μ (nm)	Q (b)
95	5/2+	0.861(7)	
97	5/2+	(-)0.787(8)	
99	5/2+	-0.641(5)	+0.079(4)
101	5/2+	-0.719(6)	+0.46(2)
103	3/2+	0.200(7)	(+)0.62(2)
105	3/2+	(-)0.32(8)	

Table 6.2: Nuclear spin, parity, magnetic dipole moments and electric quadrupole moments for ruthenium compiled by N. Stone[50]. For the EM multipole moments, +/- signs in brackets indicate a tentative sign assignment. The lack of a +/- sign indicates that the sign is unknown.

The electric quadrupole moments are mostly unknown for the unstable ruthenium isotopes. This makes it difficult to accurately estimate the magnitude of the electric quadrupole parameter, B. However, as discussed in section 5.3, the electric quadrupole interaction has a considerably smaller effect upon the position of a spectral HFS structure line than the magnetic dipole interaction. It is therefore possible to generate a sufficiently accurate prediction of the frequency of a HFS line by neglecting the electric quadrupole interaction. Once the frequency of a HF spectral line has been estimated the corresponding acceleration voltage can be calculated using equation 6.3.

For unstable isotopes with $A \leq 95$ and $A \geq 105$ the nuclear spins are only tentatively known[35] and no electromagnetic multipole data is available. For these isotopes it is not possible to estimate the position of hyperfine structure lines relative to the transition centroid. However, rough acceleration voltage estimates for the transition centroids can still be made using kinematic and isotope shifts only.

Chapter 7

Conclusion

Crossed beam laser spectroscopy has been used to measure nineteen optical transitions in atomic ruthenium across a wavelength range of 296 – 360nm. Of these transitions, twelve exhibit significant isotope shifts which are displayed in table 5.3. These isotope shifts have been used with muonic atom spectroscopy Seltzer moment data[38] to produce, via a combined analysis technique, new values for the change in mean-square charge radius, $\delta\langle r^2\rangle^{A,A'}$, between the seven stable ruthenium isotopes. The $\delta\langle r^2\rangle^{A,A'}$ values obtained for each of these transitions are displayed in appendix A. The weighted mean values for $\delta\langle r^2\rangle^{A,A'}$ obtained during this work (see table 5.8) exhibit up to an order of magnitude improvement in accuracy compared to previously published MSCR data[38]. These values therefore provide the best set of charge radii systematics currently available for stable ruthenium.

The isotope shift, hyperfine structure parameters and electronic factors F_i and M_i presented in this thesis are also of value to theorists in a number of physics fields. For example, the transition isotope shifts and values for F_i and M_i (displayed in appendix A) can be used to evaluate the specific mass shift and to test the accuracy of electronic wavefunction calculations[2]. The isotope shift values along with the hyperfine A and B parameters are also of interest to astrophysicists when identifying spectral lines in stars[51]. The 343.6736nm and 349.8942nm transitions in particular are used as good indicators of the solar abundance of ruthenium[52].

Figure 7.1 displays the charge radii systematics for ruthenium along with those of the elements $36 \leq Z \leq 42$. This region of the nuclear chart is well known for exhibiting a sudden-onset of deformation at $N = 60$. The sudden-onset of deformation first occurs in

the rubidium ($Z = 37$)[4] chain. It then gets progressively larger with increasing Z before reaching a maximum in the yttrium ($Z = 39$)[6] chain. For $Z > 39$ the step change in the deformation decreases until it seems entirely washed out in the molybdenum chain ($Z = 42$)[9].

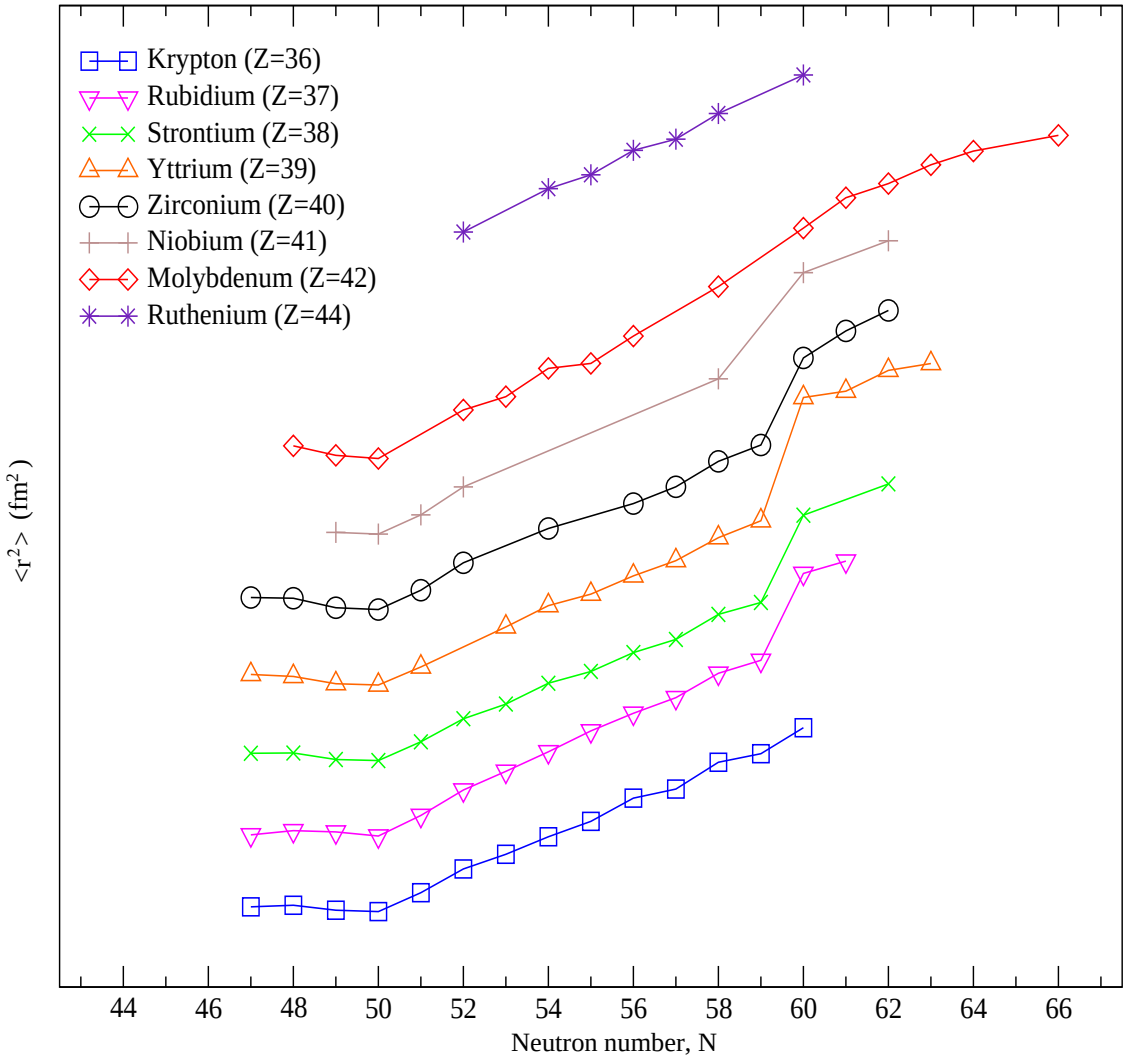

Figure 7.1: Change in mean-square charge radii, $\delta\langle r^2\rangle$ for Kr[3], Rb[4], Sr[5], Y[6], Zr[7], Nb[8] and Mo[9]. Also displayed are the ruthenium $\delta\langle r^2\rangle$ values obtained during this work. Each isotope chain has been offset in the y-axis from the previous chain by an arbitrary amount for clarity.

Figure 7.2 displays the charge radii systematics, $\delta\langle r^2\rangle$, for the even Z elements in the $N = 60$ region of the nuclear chart. In this figure no offset has been applied to the individual element chains so that the differences between the element chains are clearer. The krypton chain shows a linear increase in $\delta\langle r^2\rangle$, with the exception of odd-even isotope staggering, across $N = 60$. The zirconium and strontium chains both exhibit sudden increases in charge radii at $N = 60$. The molybdenum and ruthenium charge radii systematics are similar up until $N = 58$. At $N = 60$ the ruthenium deformation is only

slightly larger than that shown in the krypton chain indicating that for $Z \geq 44$ at $N = 60$ there is no sudden onset of deformation observed. Interestingly, the molybdenum deformation at $N = 60$ increases by a greater amount than that of ruthenium and eventually at $N > 60$ obtains a similar level of deformation to that seen in the zirconium and strontium chains. This implies a behaviour that is significantly different to the ruthenium chain suggesting that the molybdenum isotopes are still influenced by the $N = 60$ onset of deformation. To confirm the behaviour of the ruthenium isotope chain for $N > 60$ it would be useful to perform laser spectroscopy measurements on radioactive neutron-rich ruthenium isotopes.

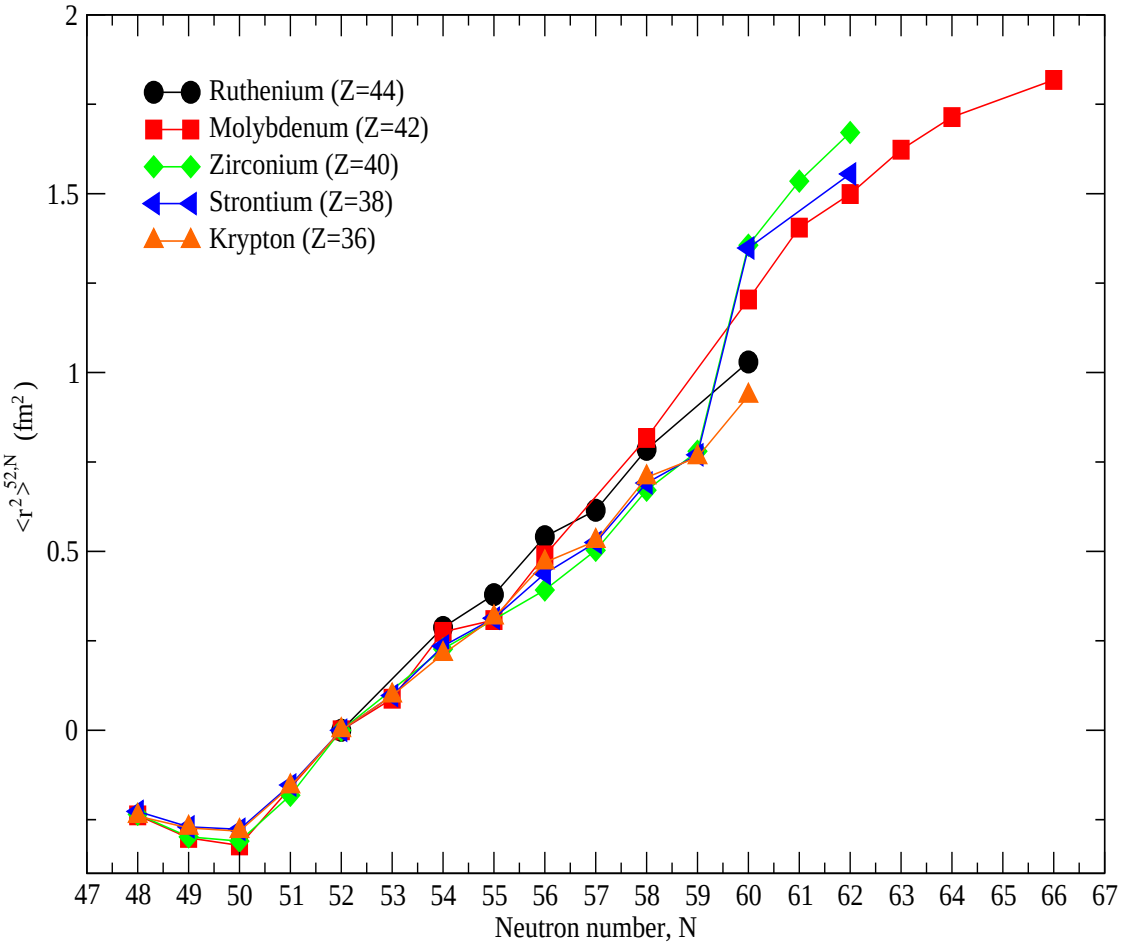

Figure 7.2: Change in mean-square charge radii relative to the $N = 52$ isotope, $\delta\langle r^2\rangle^{52,N}$ for elements Kr[3], Sr[5], Zr[7], Mo[9] and Ru. Only the even Z elements are displayed for clarity. Error bars are smaller than the size of the data points.

In order to measure the properties of radioactive ruthenium it is necessary to perform collinear laser spectroscopy measurements at a radioactive ion beam facility. Currently the only ion beam facility able to produce a beam of ruthenium is the IGISOL facility at JYFL. As discussed in chapter 6 this is because other ion beam production methods

are dependent upon the chemical properties of the element and cannot extract highly refractive elements such as ruthenium[43]. It is also necessary to perform laser spectroscopy on atomic ruthenium as the optical transitions in ionic ruthenium cannot be used with the laser currently available at JYFL. The optical transitions in atomic ruthenium measured during this work therefore fulfil a large portion of the preliminary tests usually performed prior to conducting a collinear laser spectroscopy experiment. The 349.8942nm, $0 \longrightarrow 28571.890\text{cm}^{-1}$, transition in particular exhibits high experimental efficiency due to the absence of available lost state transitions to depopulate the atomic beam prior to crossing in front of the PMT. Figure 7.3 displays the calculated number of photons emitted per atom as a function of distance from the initial point of resonance for three of the transitions measured during this work. The data in the graph were calculated using the same method described in section 6.1.1 to produce graph 6.2.

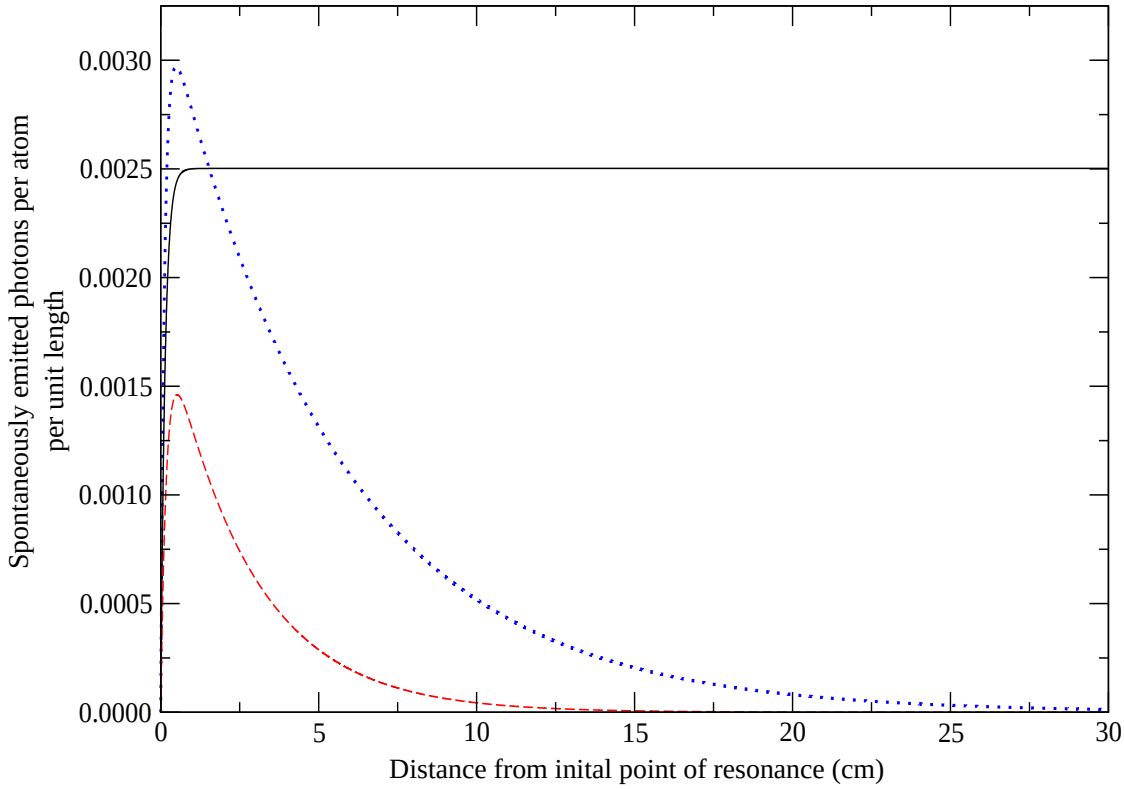

Figure 7.3: Graph comparing the calculated number of photons emitted per atom per length increment ($\simeq$ 0.0027cm) as a function of distance travelled for the 343.6736nm (dashed red trace), the 349.8942nm transition (solid black trace) and the 358.9213nm (dotted blue trace) transitions in atomic ruthenium.

The 349.8942nm transition exhibits no drop in photon production as the atom beam travels on resonance down the beam line due to the absence of allowed lost state transitions. This transition is therefore likely to possess good experimental efficiency as all

of the atoms in the beam have the potential to produce resonant photons whilst crossing in front of the PMT. In contrast, the 343.6736nm and 358.9213nm transitions suffer a drop in photon production due to the laser pumping atoms into lost states. For the typical case where the charge exchange cell is ∼30cm from the PMT very few resonant photons would be produced by the atom beam via the 343.6736nm and 358.9213nm transitions whilst passing in front of the PMT. The calculations used to produce figure 7.3 assumed a laser power of 1mW, a laser beam diameter of 1mm and perfect overlap between the atomic and laser beam. In order to measure the 343.6736nm and 358.9213nm transitions effectively figure 7.3 suggests that it would be necessary to reduce the laser beam power density to decrease the pump rate into lost states. Whilst ensuring that more atoms reach the PMT without being pumped into a lost state, reducing the power density also reduces the production rate of photons whilst the beam is passing in front of the PMT. The efficiency of these transitions is therefore still likely to be poorer than the 349.8942nm transition.

The isotope shift data and hyperfine parameters of the transition states displayed in tables 5.3 and 5.4 respectively can be used to predict the resonance frequency for radioactive ruthenium isotopes. These predictions can be used to calculate the acceleration voltages required to measure these isotopes via collinear laser spectroscopy. The procedure required to make these prediction was discussed at length in section 6.2.2.

In summary, this thesis has presented improved values for the change in mean-square charge radius between the stable isotopes of ruthenium. Comparing these values to the neighbouring element isotope chains indicates that ruthenium behaves differently at $N = 60$ to the other elements $37 \leq Z \leq 42$ with no sudden onset of deformation observed. In order to investigate this trend further it would be advantageous to study the radioactive neutron-rich ruthenium isotopes. The work conducted for this thesis provides a valuable set of offline test data that can be used to assist in the planning of future experiments at a radioactive ion beam facility. One atomic transition in particular has been identified as particularly promising for collinear laser spectroscopy work and the necessary experimental conditions have been considered. The MSCR values obtained during this work can be used in conjunction with future isotope shift measurements to provide accurate model-independent values for the MSCR of neutron-rich ruthenium isotopes. Extending the charge radii systematics of ruthenium beyond $N = 60$ in this way offers the opportunity to firmly establish the upper atomic number boundary for the

sudden onset of deformation in this interesting region of the nuclear chart.

Appendix A

Mean-Square Charge Radii Values and King Plot Parameters

This appendix contains a series of data tables for the twelve transitions used to produce the weighted mean values for $\delta\langle r^2\rangle^{A,A'}$ displayed in table 5.8. Tables A.1 and A.2 display the values of $\delta\langle r^2\rangle^{A,A'}$ obtained for the individual transitions used to produce the final weighted mean $\delta\langle r^2\rangle^{A,A'}$ values.

Table A.3 contains the field shift parameter, F_i and scaled mass shift parameter $\mu_{ref}M_i$ obtained from King plots of isotope shifts (measured during this work) plotted against Seltzer moments (tabulated by Fricke et al.[2]). The reference parameter μ_{ref} was calculated using equation

$$\mu_{ref} = \frac{A_{ref} - A'_{ref}}{A_{ref}A'_{ref}}, \tag{A.1}$$

with $A = 104$ and $A' = 102$.

		Transition λ (nm)					
A'	A	298.8947	315.9929	318.6043	318.9979	319.6605	329.4112
98	96	274.4(76)	288.6(67)	288.7(68)	288.7(73)	288.5(70)	289.4(68)
100	98	279(19)	253.1(67)	252.7(71)	254.7(67)	252.6(76)	254.1(73)
102	100	241(19)	245.0(79)	244.1(83)	246.9(73)	243.2(86)	245.2(88)
104	102	256.9(66)	255.2(56)	255.1(59)	255.9(52)	254.9(60)	253.7(60)
99	98	104(12)	91.1(50)	90.1(52)	92.0(45)	90.0(58)	91.2(53)
101	100	69(14)	73.8(57)	74.1(60)	73.8(50)	73.8(62)	74.3(63)

Table A.1: Extracted $\delta\langle r^2\rangle^{A,A'}$ values for the 298-330nm transitions.

		Transition λ (nm)					
A'	A	330.1594	343.6736	349.8942	358.9213	359.3018	359.6178
98	96	287.6(62)	289.9(75)	288.4(68)	287.1(68)	285.9(54)	291.5(81)
100	98	254.9(64)	251.6(80)	253.1(73)	245.0(72)	258.2(56)	248.3(88)
102	100	243.4(78)	244.1(95)	244.2(88)	243.9(85)	245.7(70)	237(10)
104	102	255.6(54)	253.4(65)	254.0(60)	255.8(61)	254.5(46)	255.1(71)
99	98	91.9(47)	89.9(60)	90.9(54)	89.5(55)	94.6(40)	93.3(69)
101	100	73.4(56)	74.6(69)	74.2(64)	74.1(62)	73.1(51)	71.8(81)

Table A.2: Extracted $\delta\langle r^2\rangle^{A,A'}$ values for the 330-360nm transitions.

λ (nm)	F_i (MHzfm^{-2})	$\mu_{ref}M_i$ (MHz)
298.8947	-136(9)	-104(2)
315.9929	-609(59)	-48(14)
318.6043	-623(65)	-48(15)
318.9979	-376(32)	-82(8)
319.6605	-533(57)	-59(13)
329.4112	-2584(277)	210(65)
330.1594	-2637(253)	208(60)
343.6736	-2775(332)	231(79)
349.8942	-1826(200)	105(48)
358.9213	-2764(296)	209(70)
359.3018	-2737(231)	222(55)
359.6178	-1180(155)	14(37)

Table A.3: King plot values of F_i and $\mu_{ref}M_i$ for each transition.

Appendix B

Chi-squared surface plot

When fitting a spectrum using the routine described in section 5.2 it is necessary to provide the chi-squared minimisation routine with initial values for the fit parameters. Section 5.2.2 explains the methods used to identify the peaks in a measured spectrum however for some spectra it is difficult to definitively identify spectral peaks. For these spectra it is useful to map the chi-squared surface for the fitting parameters in order to identify the true fit values.

Figure B.1 displays an example of a chi-squared surface plot for a measurement of the 359.6178nm transition. The plot was formed using the data obtained from a specially modified version of xmgrace using the following procedure:

1. Initial values for the isotope centroids were inputted.

2. The relative intensities of the different isotopes were scaled to a selected isotope according to atomic abundances.

3. The hyperfine parameters of the transition lower state, A_L andB_L, were fixed to the values given by Büttgenbach[36] for both ^{99}Ru and ^{101}Ru.

4. The transition upper state hyperfine parameters, A_U and B_U, of ^{99}Ru were scaled to those in ^{101}Ru according to the ratio between the lower state HF parameters (see section 5.2.2).

5. An initial guess for the values of A_U and B_U of ^{101}Ru were then entered into the programme. The fitting routine then varied the free line function parameters in order to obtain the best possible fit to the spectrum whilst keeping A_U and B_U for ^{101}Ru fixed to the guess values entered by the user.

6. The χ^2 of the fit for the fixed A_U^{101} and B_U^{101} values was then recorded.

7. The values for A_U^{101} and B_U^{101} were then increased by a user specified amount and the other fit parameters (such as isotope centroids) reset to their original user specified values. The fitting routine then obtained a new value of χ^2 for the new A_U^{101} and B_U^{101} values.

8. This process was repeated for many sets of values of A_U^{101} and B_U^{101}.

9. The obtained χ^2 values were then plotted against the values for A_U^{101} and B_U^{101} used during each fit to create a χ^2 surface plot such as that displayed in figure B.1.

Figure B.1 is a typical example of a chi-squared plot for many of the transitions measured during this work. A clear chi-squared minimum value for the hyperfine parameter A_U^{101} is evident at $\simeq$129MHz. For B_U^{101} there is a range of possible values which produce similarly small values for chi-squared. The global minimum value is not clear. This is because the electric quadrupole interaction has a smaller perturbative effect upon an atomic energy level than the magnetic dipole interaction. The position of a spectral line is therefore less sensitive to the hyperfine B parameter than the hyperfine A parameter. This results in the characteristic broad furrow in the chi-squared surface and also leads to larger experimental uncertainties for the extracted B values (as mentioned in section 5.3). Regardless of this fact, mapping the chi-squared surface can be a useful method of obtaining initial values for the hyperfine parameters to input into the fitting routine.

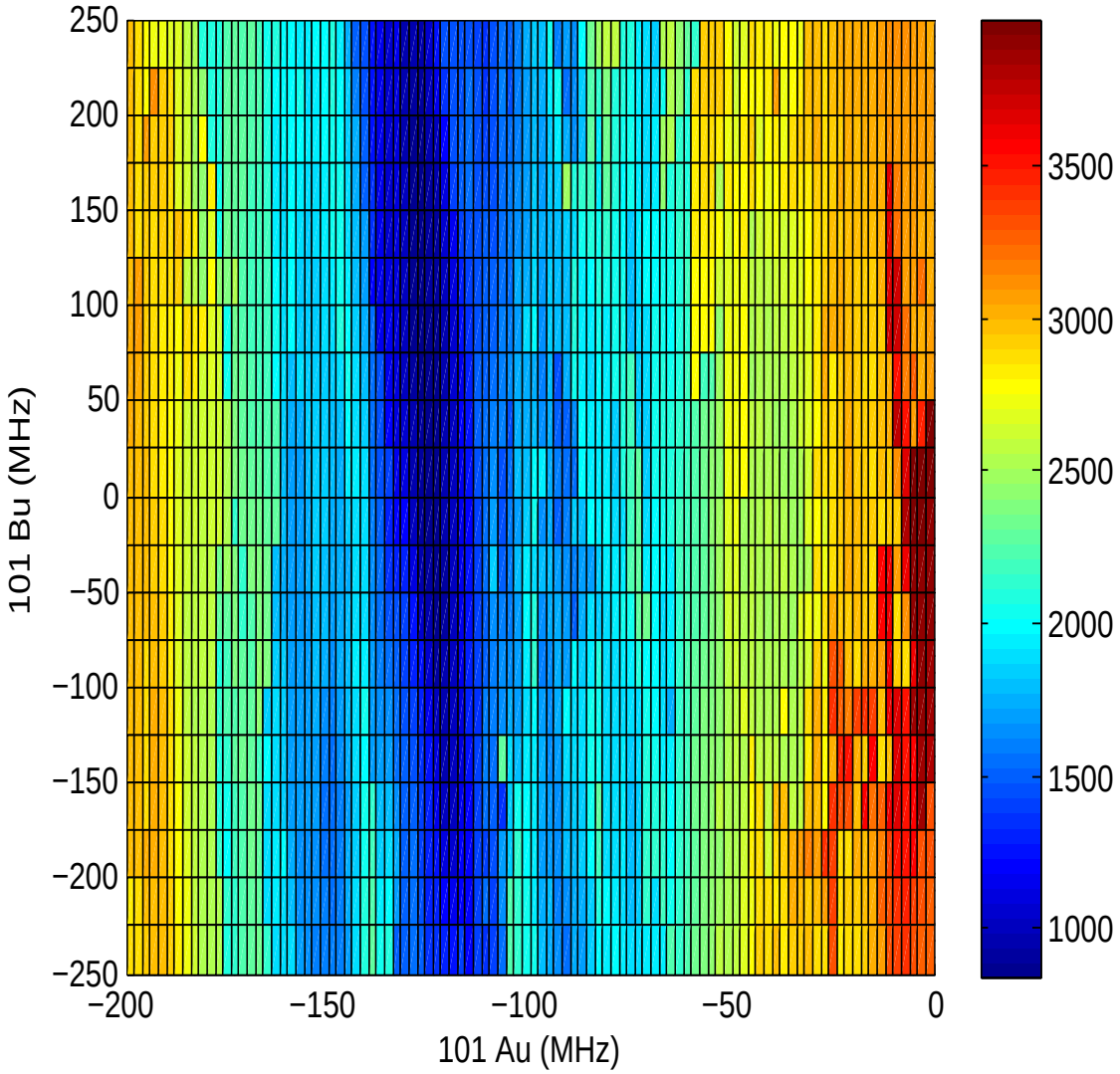

Figure B.1: A chi-squared surface plot for a spectrum measurement of the 359.6178nm transition. The colour-scale indicates the value of χ^2.

Appendix C

Spectrum Catalogue

This appendix contains a spectrum for each of the optical transitions measured during this work (as listed in table 4.3). The 315.9929nm, 318.6043nm, 318.9979nm and 319.6605nm transitions were measured by E. Cochrane in 1999 but the spectra were analysed and fitted by the author of this work. Each spectrum has been calibrated according to the procedures described in section 5.1. Each spectrum has been fitted with a line function using the programme xmgrace and the various methods discussed in section 5.2. This catalogue of spectra provides a useful guide for future laser spectroscopy measurements of atomic ruthenium.

The isotope shifts and hyperfine parameters obtained from the fitting routine for those transitions that were used to generate new ruthenium mean-square charge radii values are displayed in the main thesis in tables 5.3, 5.4 and 5.5 respectively. As discussed in sections 4.4.3 and 5.4.3, the majority of the $4d^7 5s$ to $4d^6 5s5p$ type transitions exhibit incredibly narrow spectra. These transitions proved difficult to fit as a number of hyperfine structure component are screened by the larger even isotopes. Tentative values for the hyperfine parameters and isotope shifts observed in these spectra are displayed in tables C.1 and C.3 respectively, below. These values provide the only known isotope shift measurements for these transitions in atomic ruthenium and the only known values of the hyperfine parameters for these high-lying atomic states. As a point of interest, the 297.6925nm transition exhibits almost no isotope shift indicating that the mass and field shift components nearly perfectly cancel each other out.

The 301.7235nm and 342.8318nm transitions could not be fitted. Due to the small isotope shifts exhibited by these transitions it was decided that it was unnecessary to

commit large amounts of time to the fitting process as these transitions would not be used to extract values for the mean-square charge radius of ruthenium. The unfitted spectra for these transitions are also presented in this appendix for reference.

			99		101	
λ (nm)	E_u (cm^{-1})	J	A_u	B_u	A_u	B_u
296.5166	35806.620	3	-108.9(9)	25.8(22)	-123.1(4)	150(13)
297.6925	34772.550	5	-197.5(4)	84.3(29)	-221.4(4)	491(17)
299.4968	35471.150	4	-131.6(2)	46.4(7)	-147.4(2)	270.8(41)
300.6586	35963.870	2	-73.2(6)	14.4(6)	-81.7(7)	81.6(36)
301.7235	36238.770	1	*	*	*	*
302.0873	35806.620	3	-111.9(3)	33.5(65)	-123.9(4)	136.2(80)
304.0314	34072.410	3	-204.7(3)	3.0(11)	-229.5(3)	17.6(66)
304.2478	35963.870	2	-73.8(3)	16.9(17)	-82.4(4)	95.6(95)
304.8788	34881.920	2	-144.8(3)	-8.7(11)	-162.3(4)	-50.5(63)
309.9280	33446.840	4	-156.1(6)	0.5(20)	-175.0(6)	2(12)
342.8318	29160.460	6	*	*	*	*

Table C.1: Measured hyperfine structure parameters (MHz) of the transition upper states for both ^{99}Ru and ^{101}Ru. * signifies that this transition could not be fitted.

	99		101	
λ (nm)	A_L	B_L	A_L	B_L
304.2478	108.6(26)	7.1(13)	121.3(29)	40.2(71)

Table C.2: Measured hyperfine structure parameters (MHz) of the 3105.49cm^{-1} state for both ^{99}Ru and ^{101}Ru. The values are in agreement with those found in table 5.5.

λ (nm)	102	101	100	99	98	96
296.5166	79.5(16)	102.8(38)	168.2(28)	193.1(48)	264.6(25)	341.0(40)
297.6925	-10.6(81)	-36.8(82)	-5(15)	7.3(79)	44(16)	27(27)
299.4968	45.6(53)	43.8(31)	109.9(44)	110.6(52)	174.9(31)	219.0(32)
300.6586	124.3(75)	169.3(96)	246.5(31)	301(13)	359.5(39)	498.0(72)
301.7235	*	*	*	*	*	*
302.0873	86.3(6)	106.8(26)	179.0(15)	213.6(8)	293(12)	365.8(18)
304.0314	123.6(10)	145.5(30)	254.8(22)	315.7(19)	393.1(28)	513.0(17)
304.2478	122.4(8)	180.1(36)	247.2(24)	308.3(32)	363.8(36)	513.8(15)
304.8788	154.7(31)	250.0(39)	303.6(16)	408.4(36)	472.6(58)	657.4(46)
309.9280	139.3(39)	219.7(86)	283.7(65)	360(15)	419.2(85)	606.4(76)
342.8318	*	*	*	*	*	*

Table C.3: Measured isotope shifts (MHz) relative to ^{104}Ru. * signifies a transition that could not be fitted by the fitting programme.

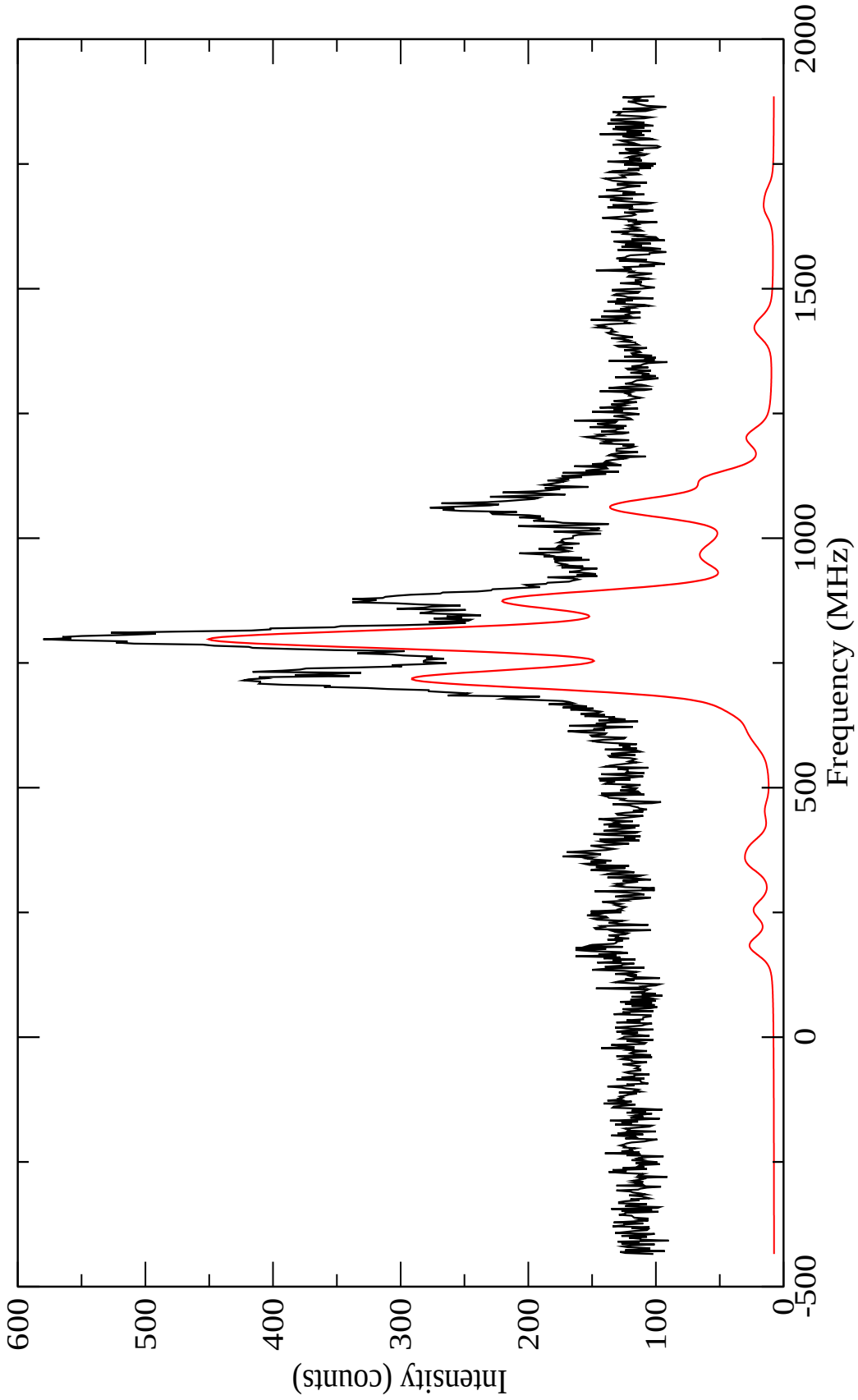

Figure C.1: 296.5166nm transition: 2091.540 (J=3) $\rightarrow$ 35806.620cm^{-1} (J=3).

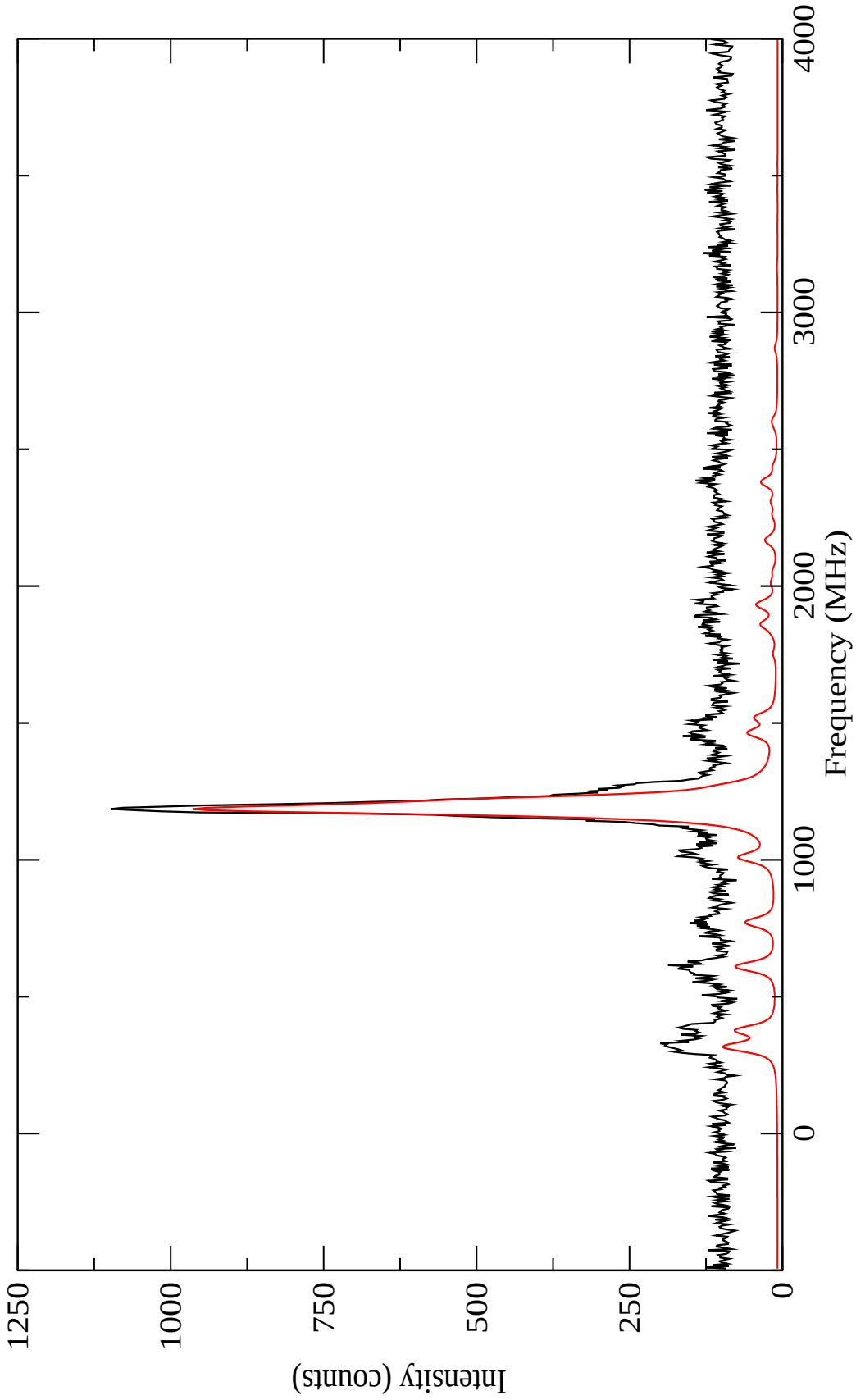

Figure C.2: 297.6925nm transition: 1190.64 (J=4) $\rightarrow$ 34772.550cm^{-1} (J=5).

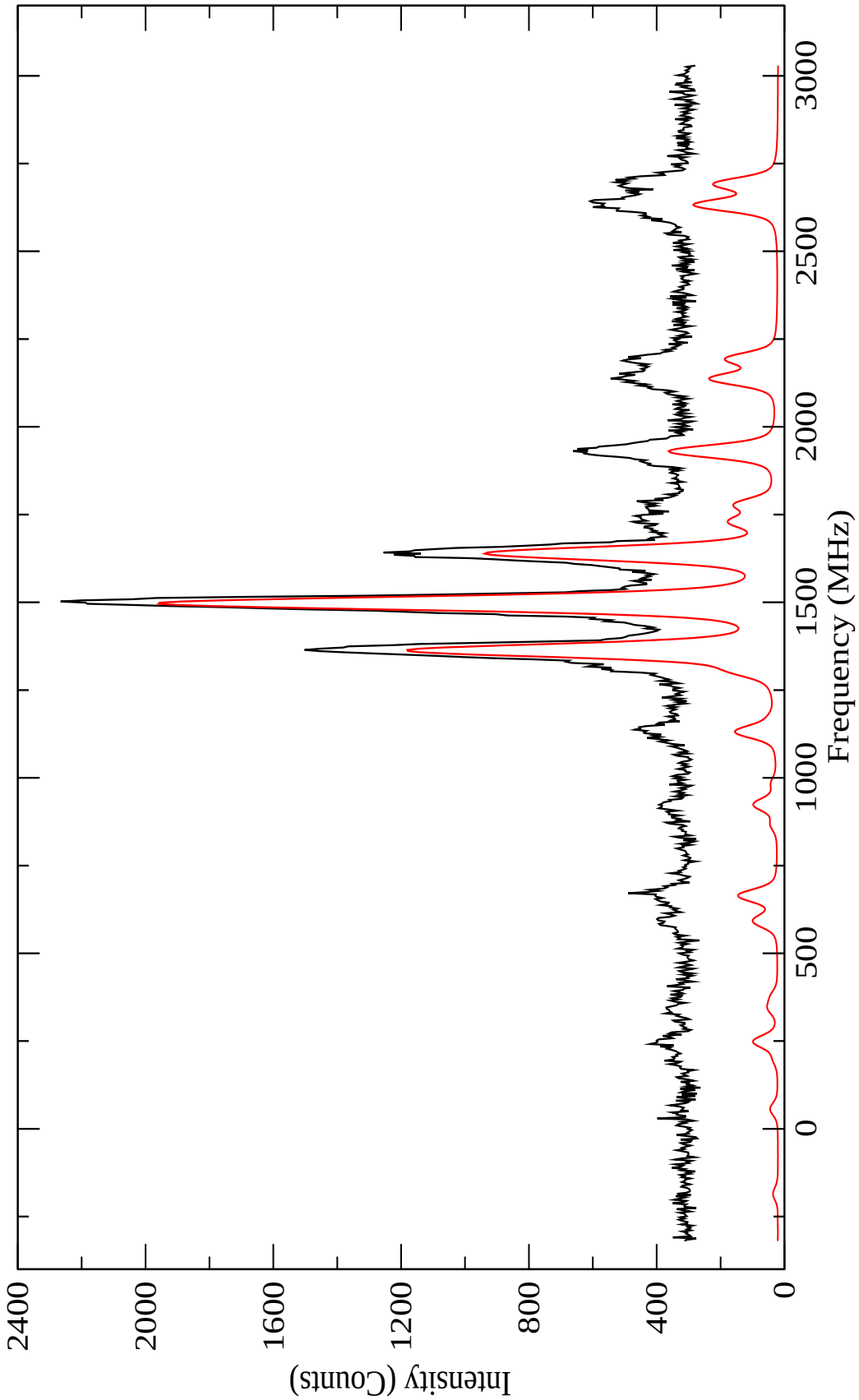

Figure C.3: 298.8947nm transition: 0.000 (J=5) $\rightarrow$ 33446.840cm^{-1} (J=4).

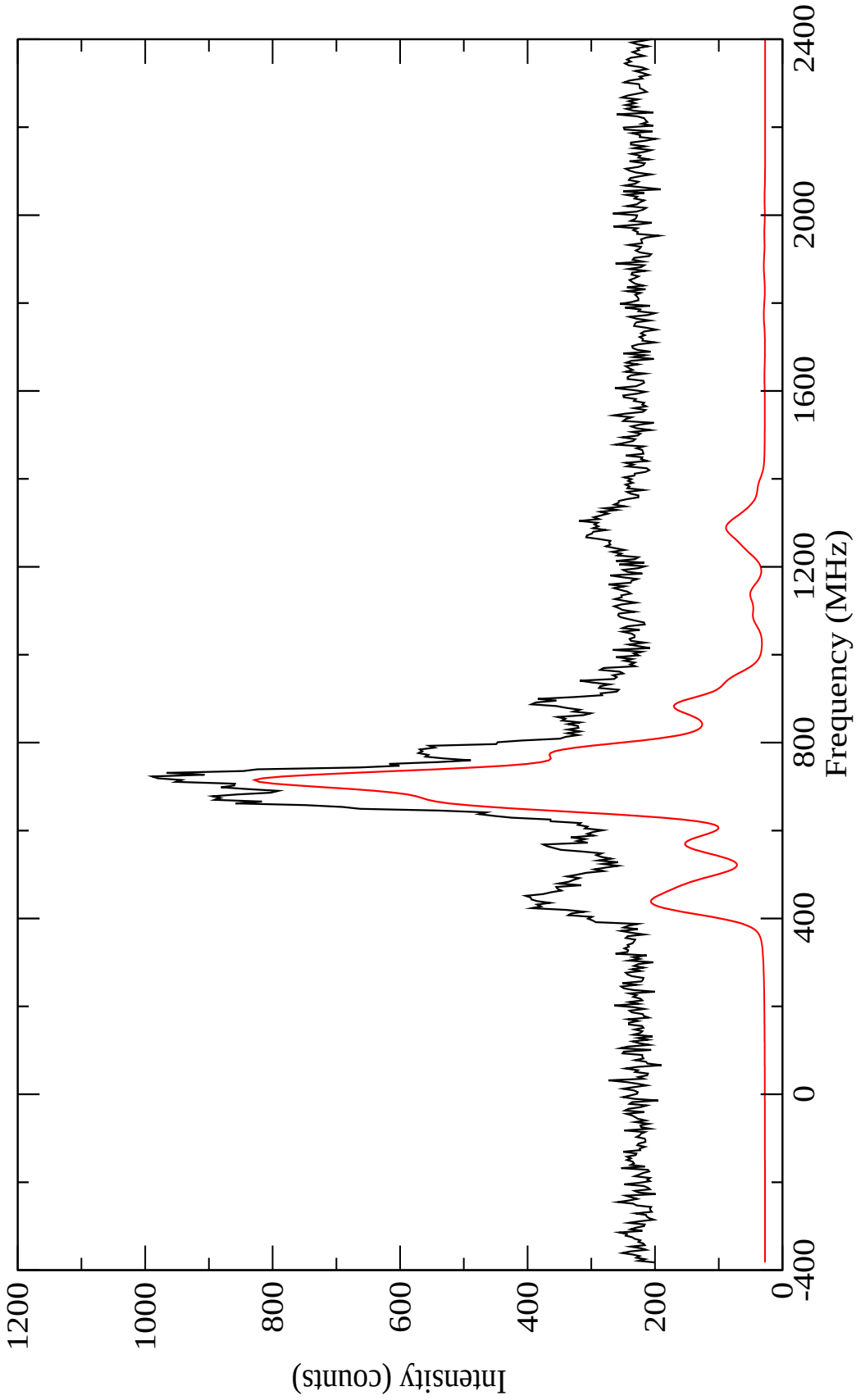

Figure C.4: 299.4968nm transition: 2091.540 (J=3) $\rightarrow$ 35471.150cm^{-1} (J=4).

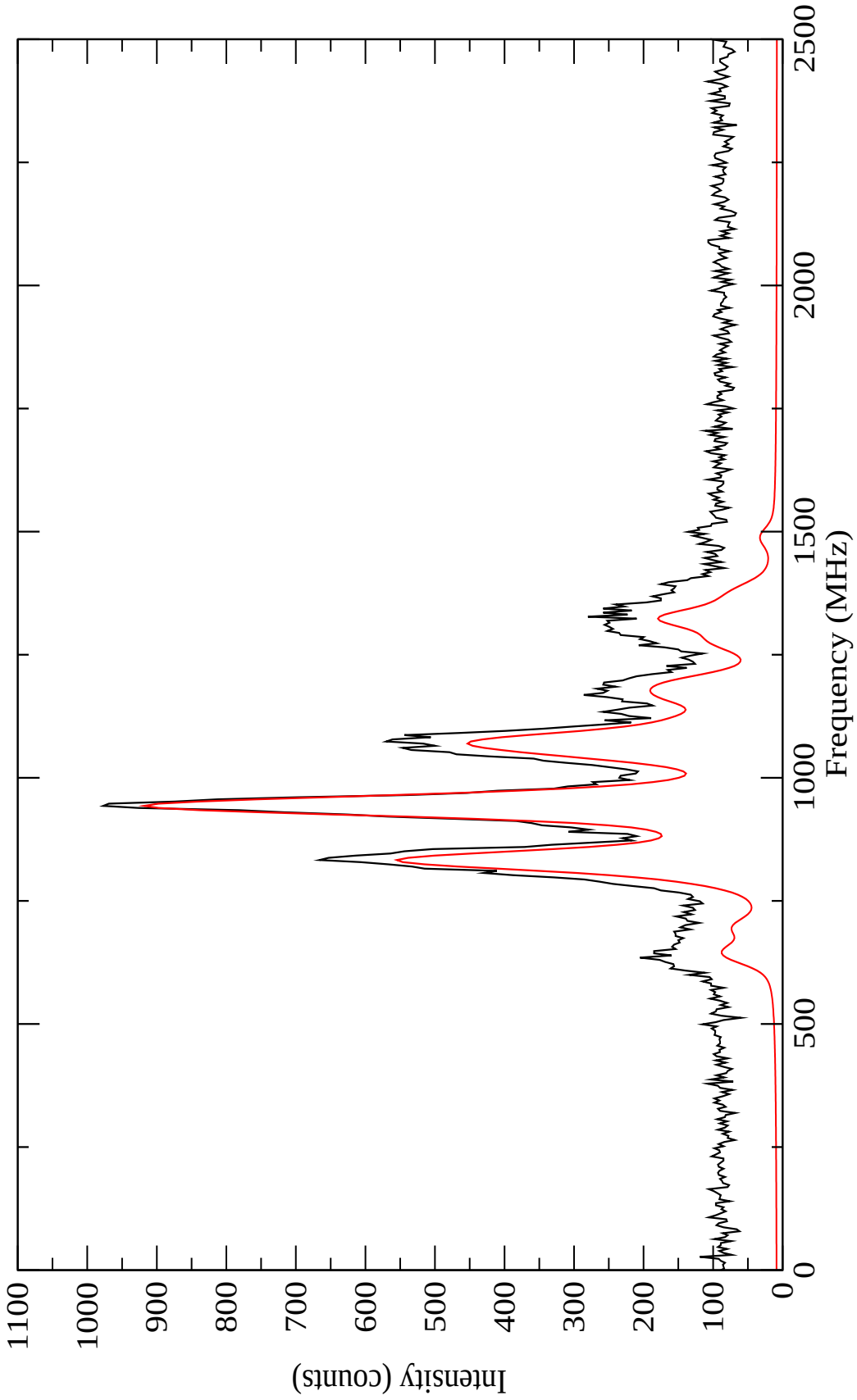

Figure C.5: 300.6586nm transition: 2713.240 (J=2) $\rightarrow$ 35963.870cm^{-1} (J=2).

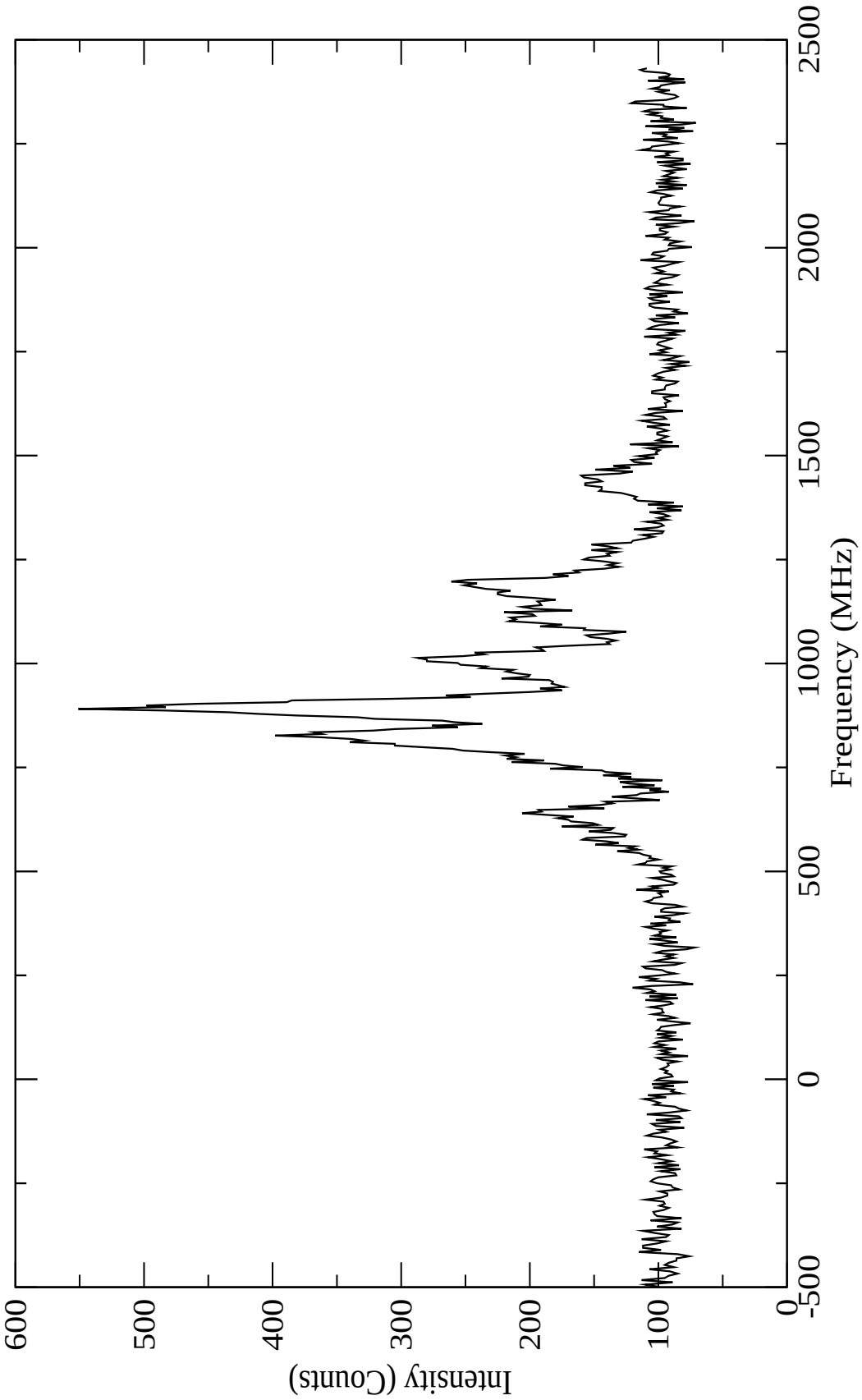

Figure C.6: 301.7235nm transition: 3105.490 (J=1) $\rightarrow$ 36238.770cm^{-1} (J=1).

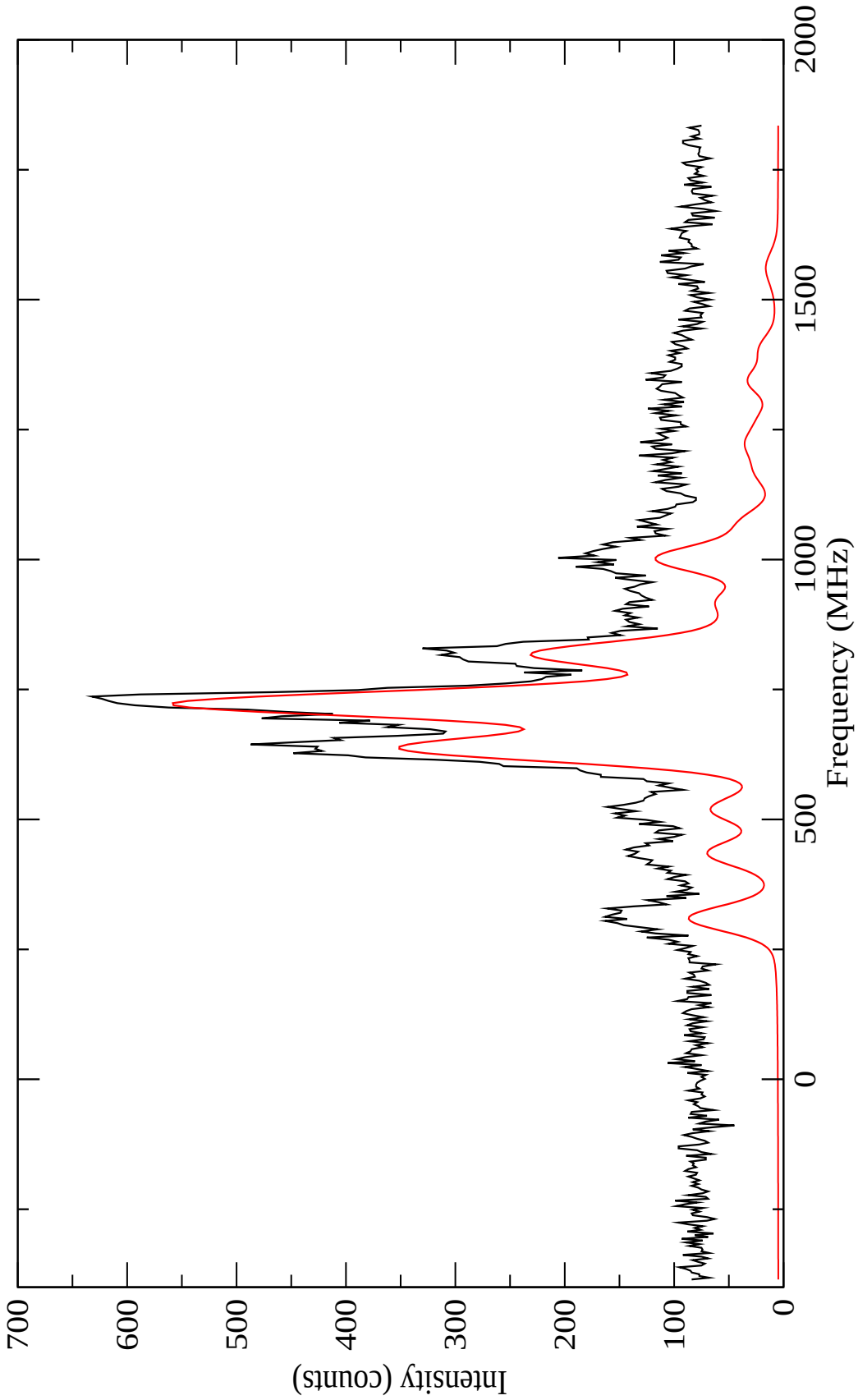

Figure C.7: 302.0873nm transition: 2713.240 (J=2) $\rightarrow$ 35806.620cm^{-1} (J=3).

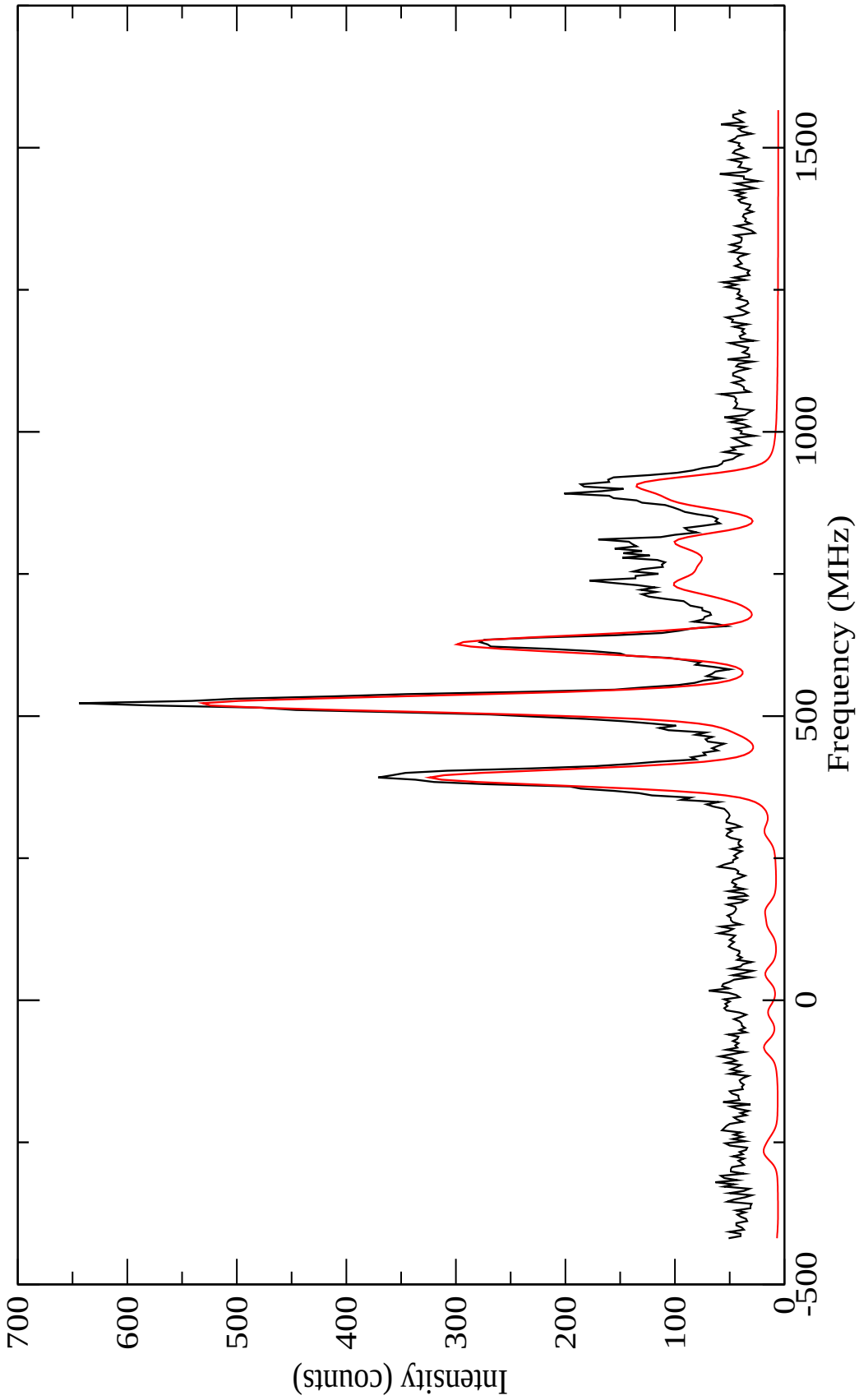

Figure C.8: 304.0314nm transition: 1190.640 (J=4) $\rightarrow$ 34072.410cm^{-1} (J=3).

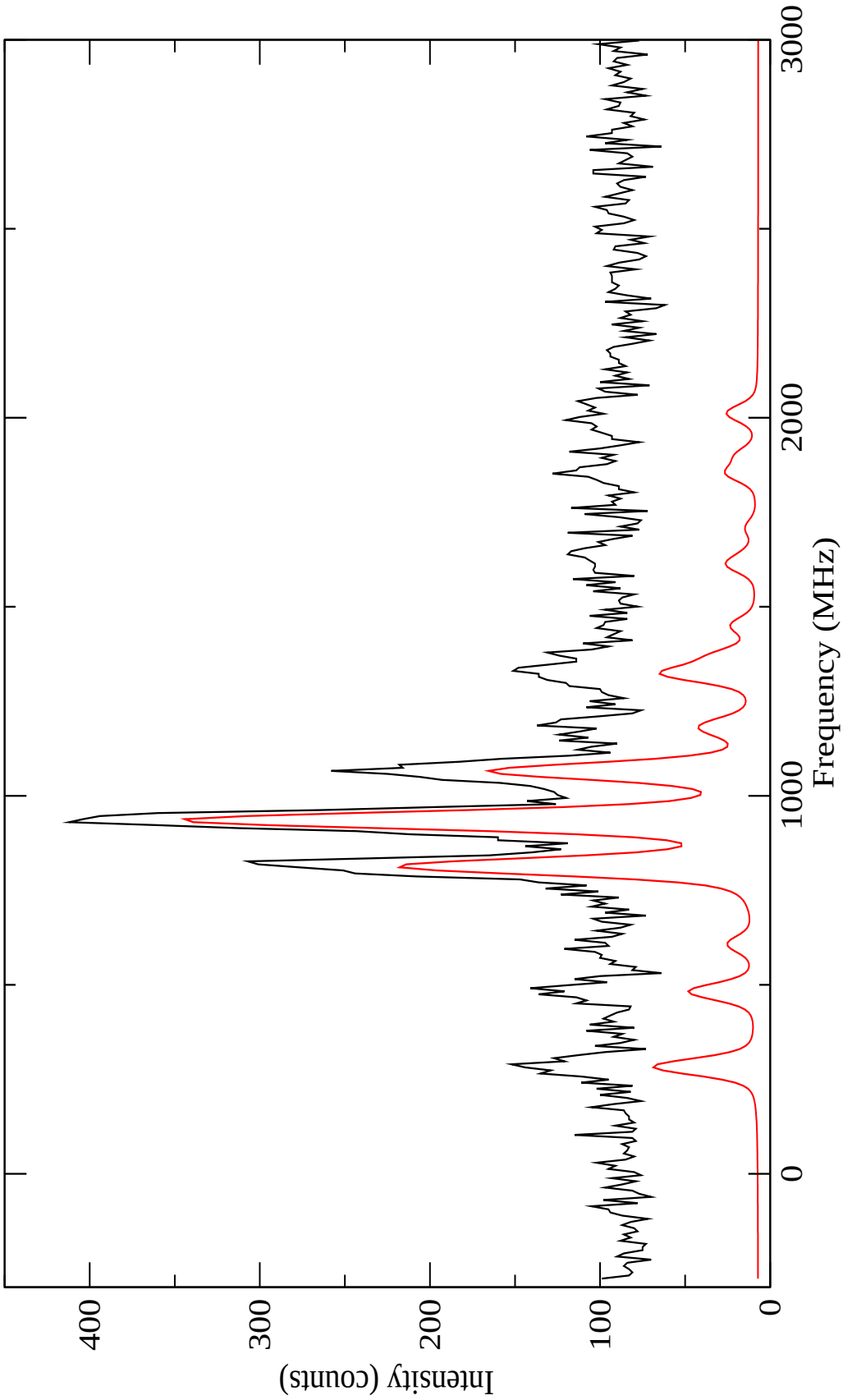

Figure C.9: 304.2478nm transition: 3105.490 (J=1) $\rightarrow$ 35963.870cm^{-1} (J=2).

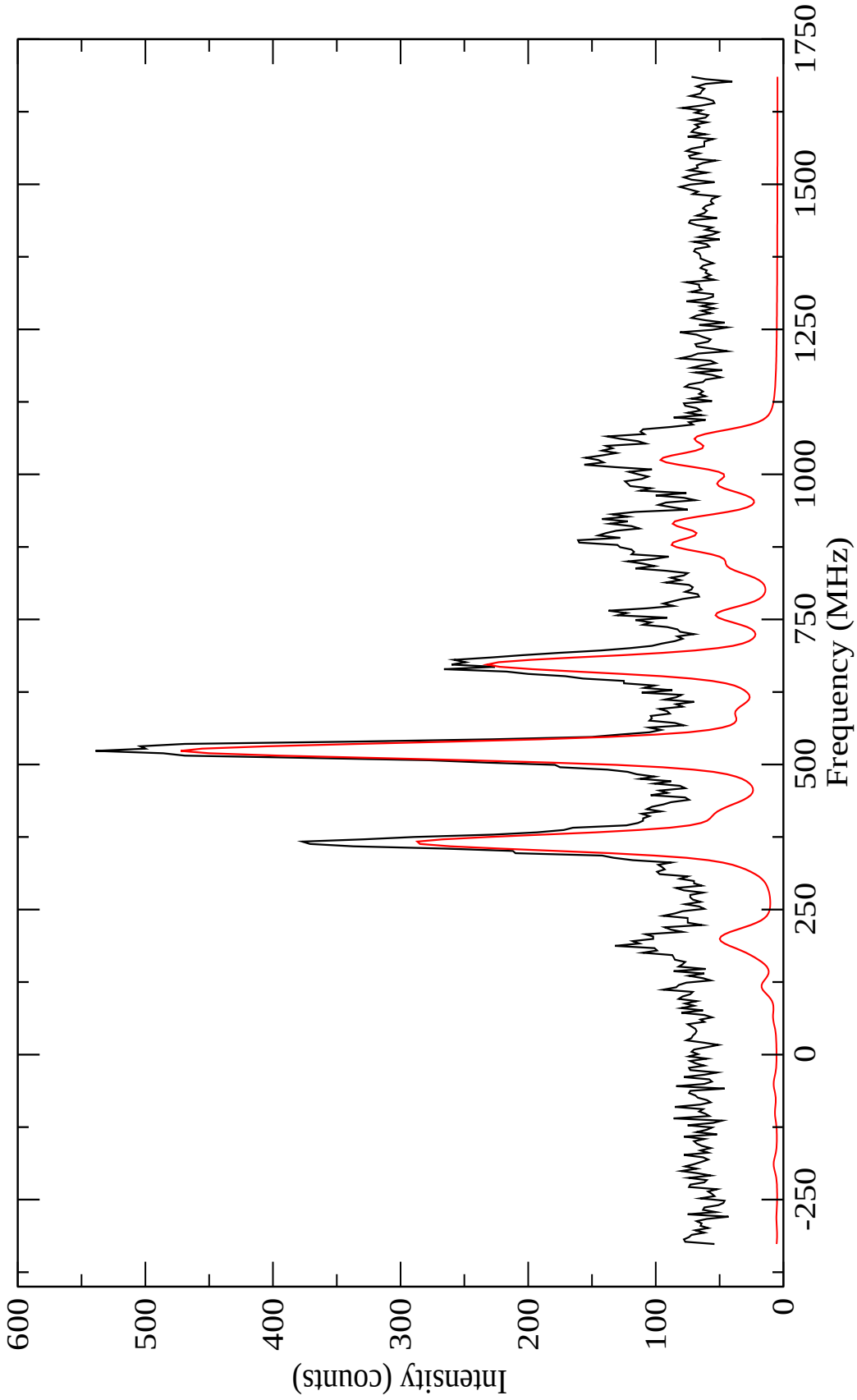

Figure C.10: 304.8788nm transition: 2091.540 (J=3) $\rightarrow$ 34881.920cm^{-1} (J=2).

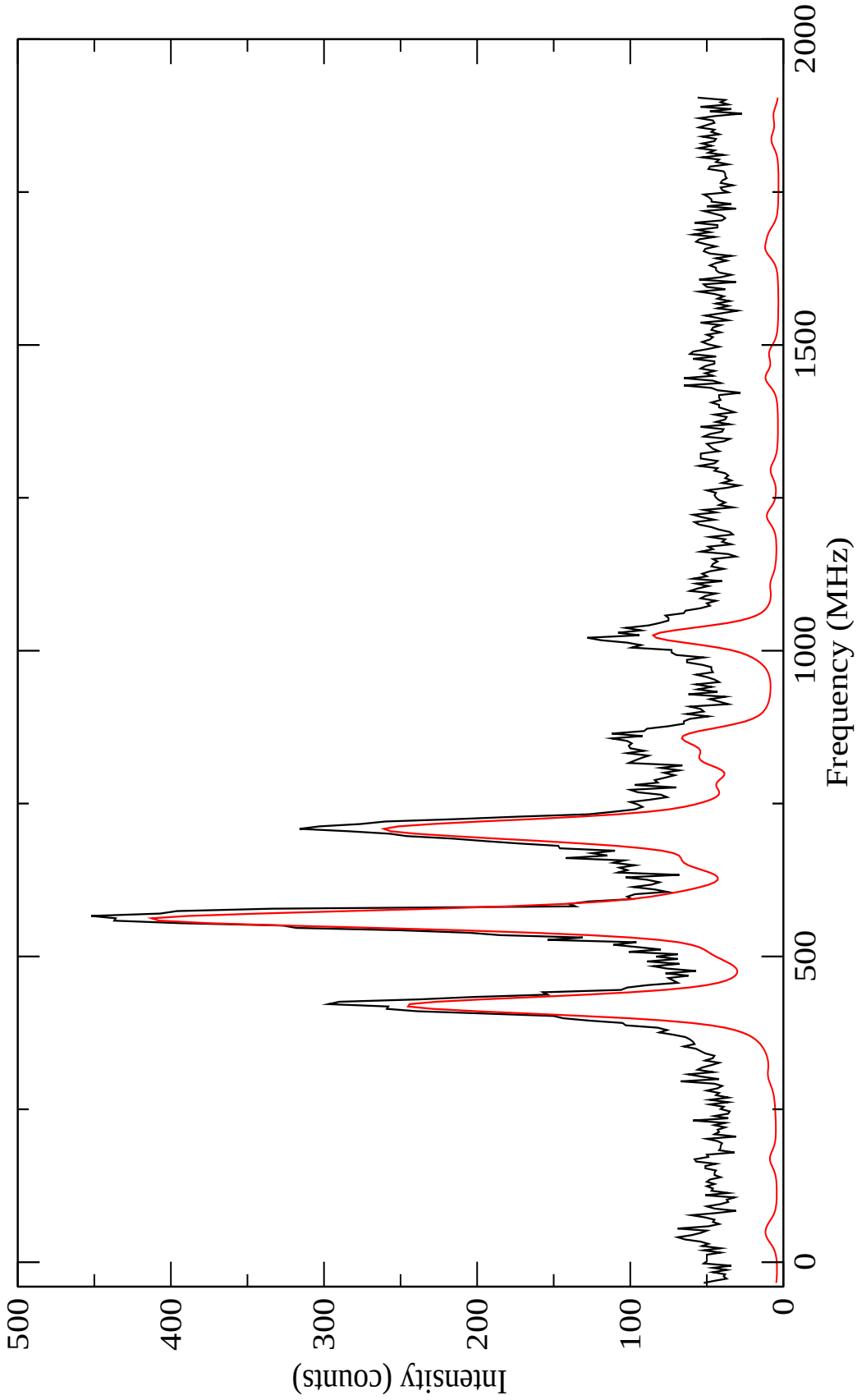

Figure C.11: 309.9280nm transition: 1190.640 (J=4) $\rightarrow$ 33446.840cm^{-1} (J=4).

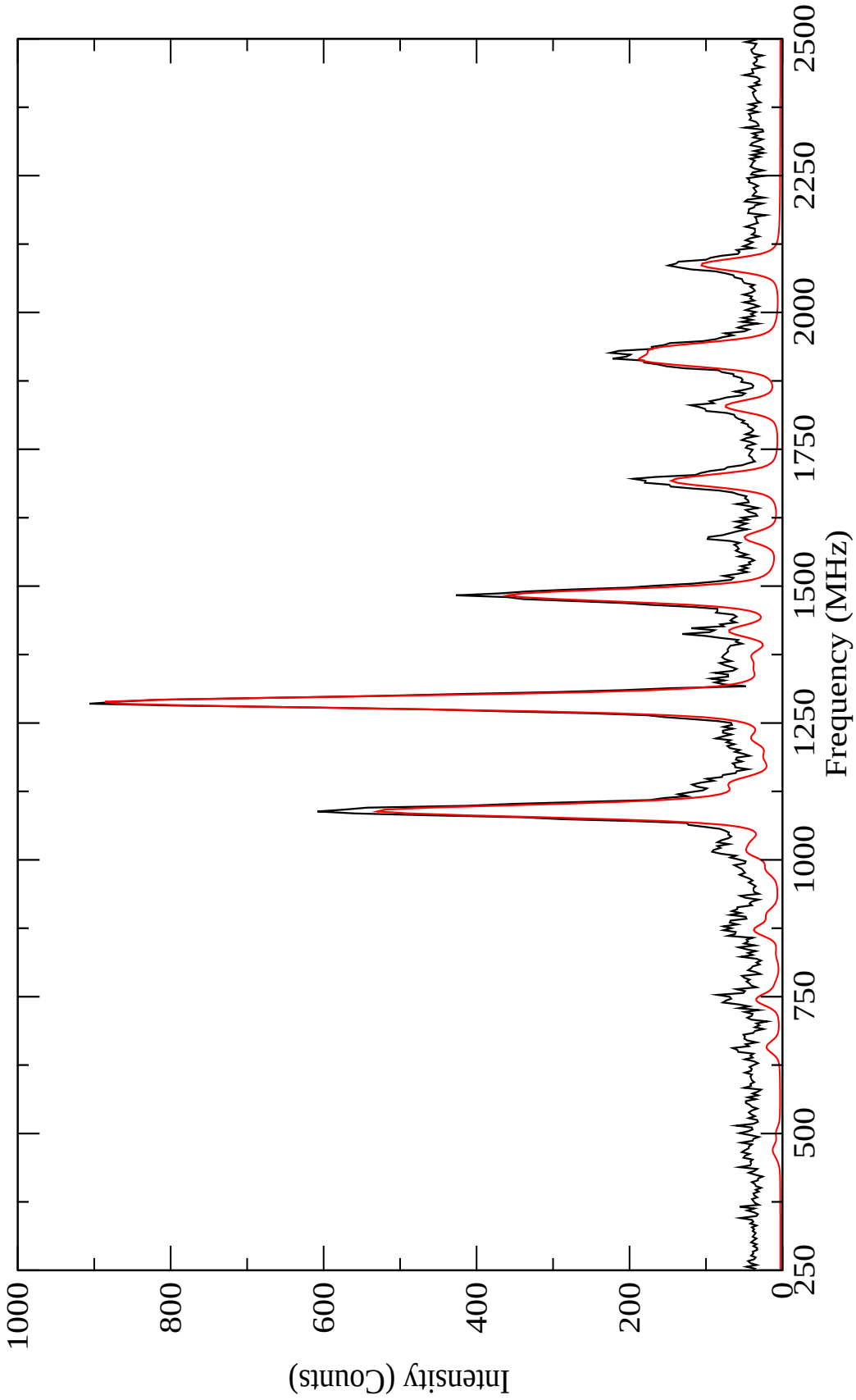

Figure C.12: 315.9929nm transition: 2091.540 (J=3) $\rightarrow$ 33728.660cm^{-1} (J=2).

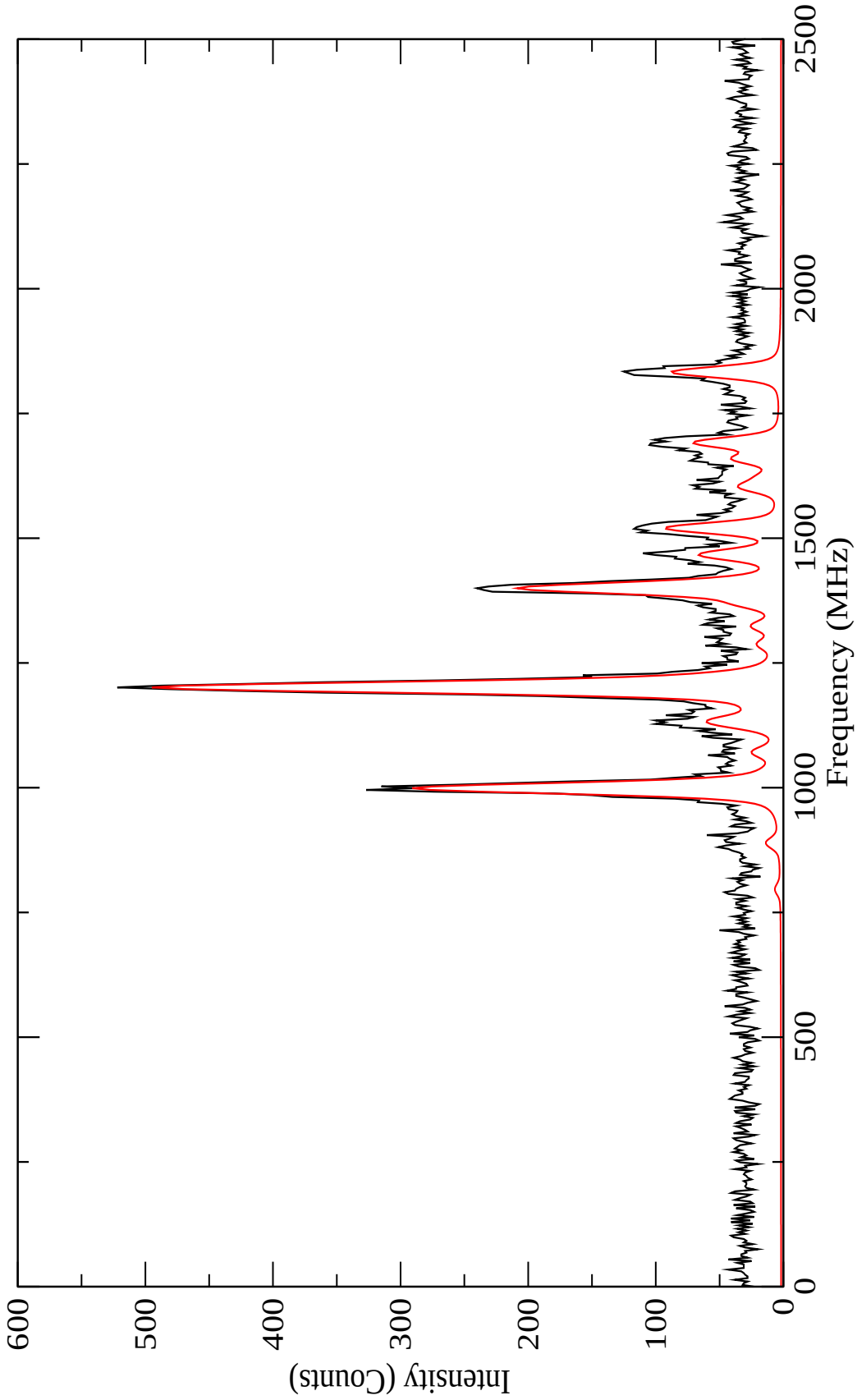

Figure C.13: 318.6043nm transition: 2713.240 (J=2) $\rightarrow$ 34091.060cm^{-1} (J=1).

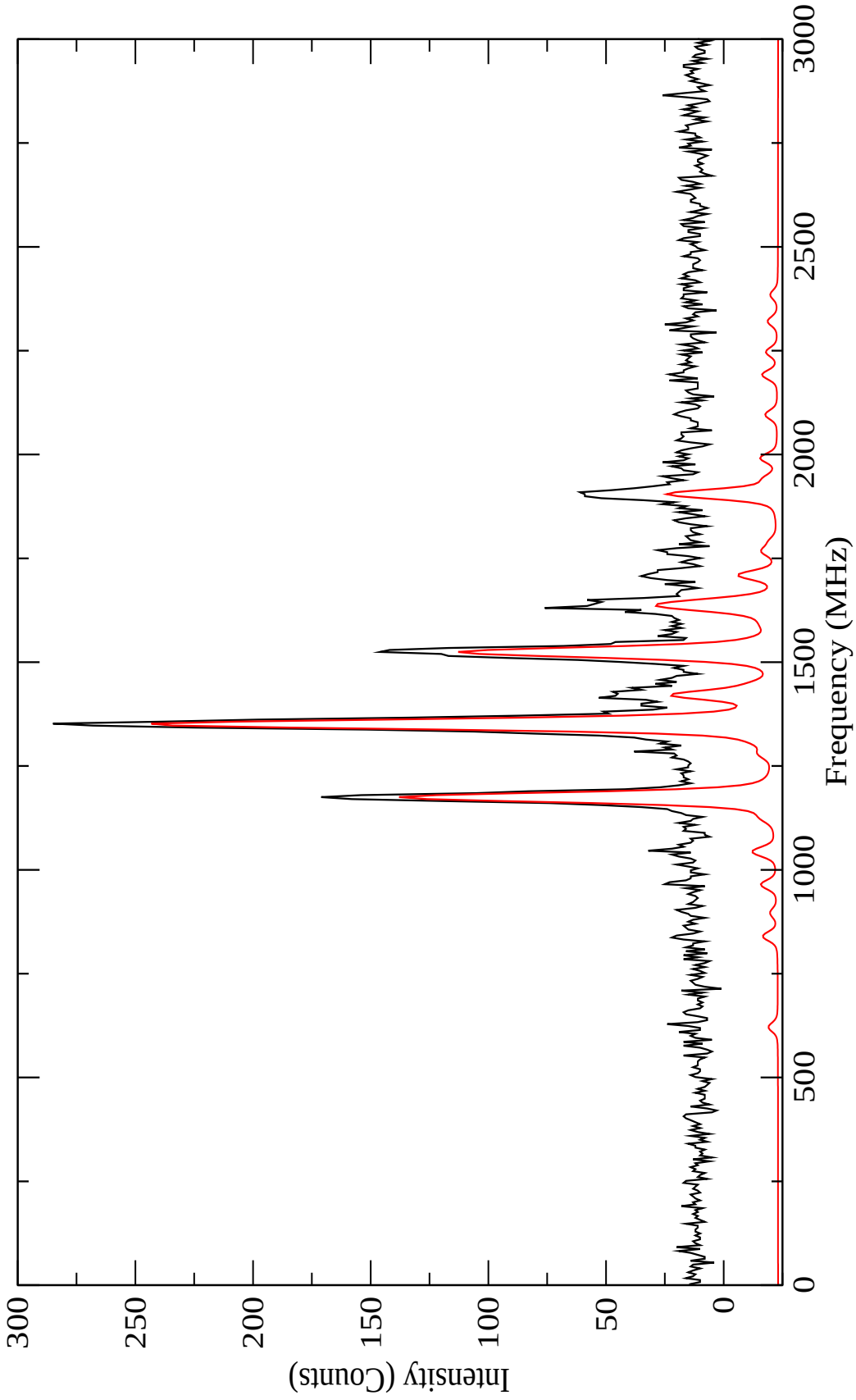

Figure C.14: 318.9979nm transition: 2091.540 (J=3) $\rightarrow$ 33430.650cm^{-1} (J=3).

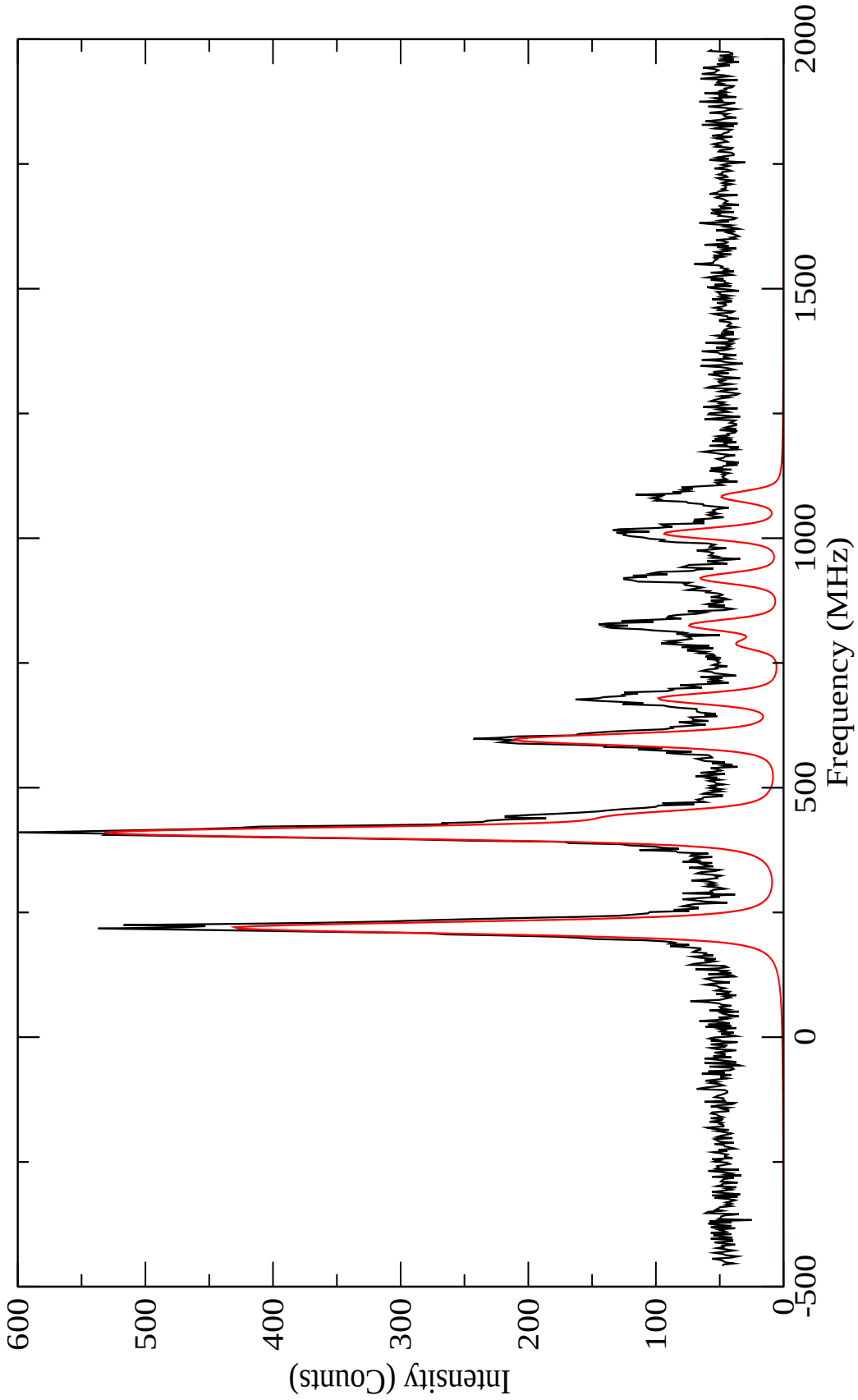

Figure C.15: 319.6605nm transition: 3105.490 (J=1) $\rightarrow$ 34379.640cm^{-1} (J=0).

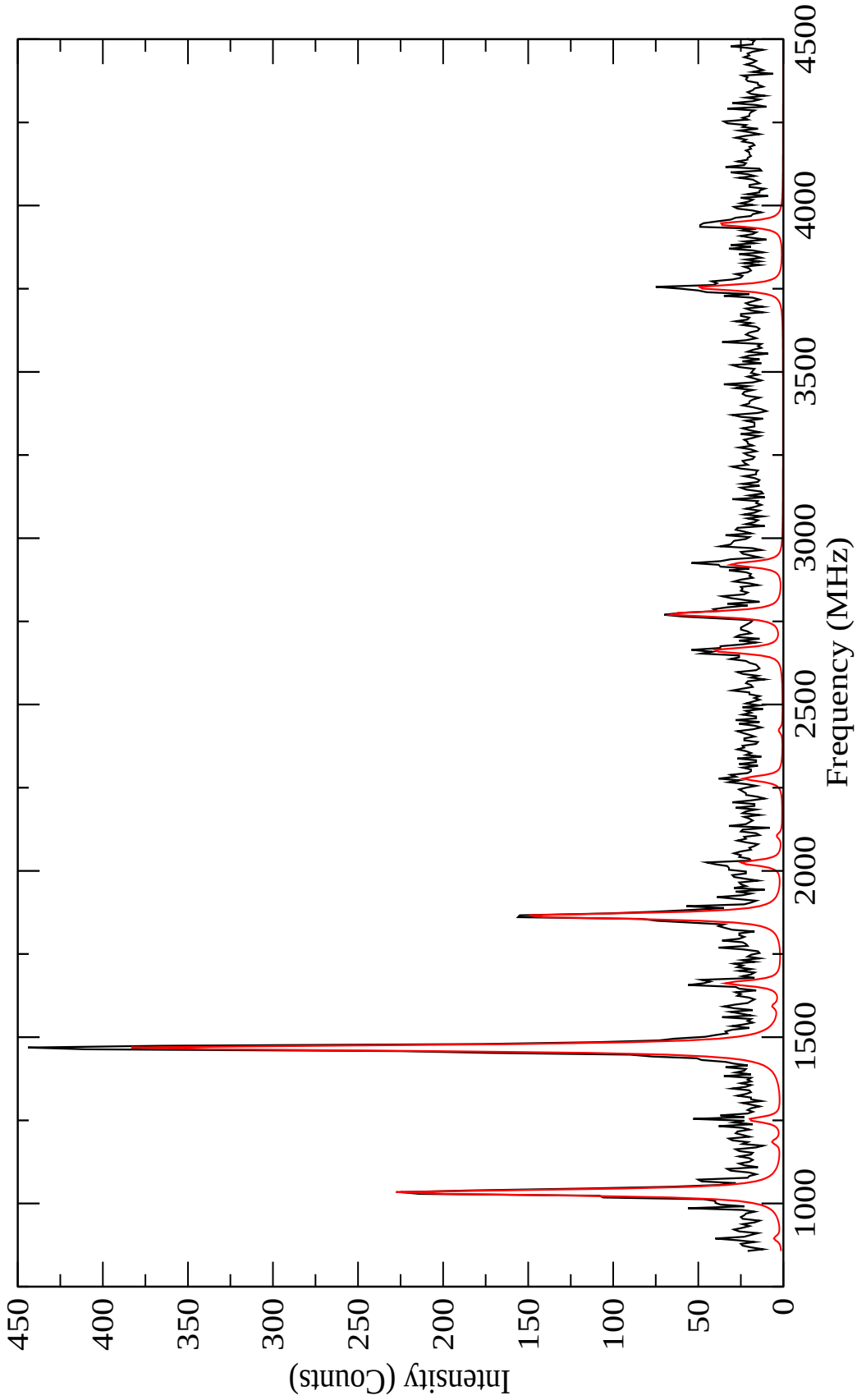

Figure C.16: 329.4112nm transition: 0.000 (J=5) $\rightarrow$ 30348.450cm^{-1} (J=4).

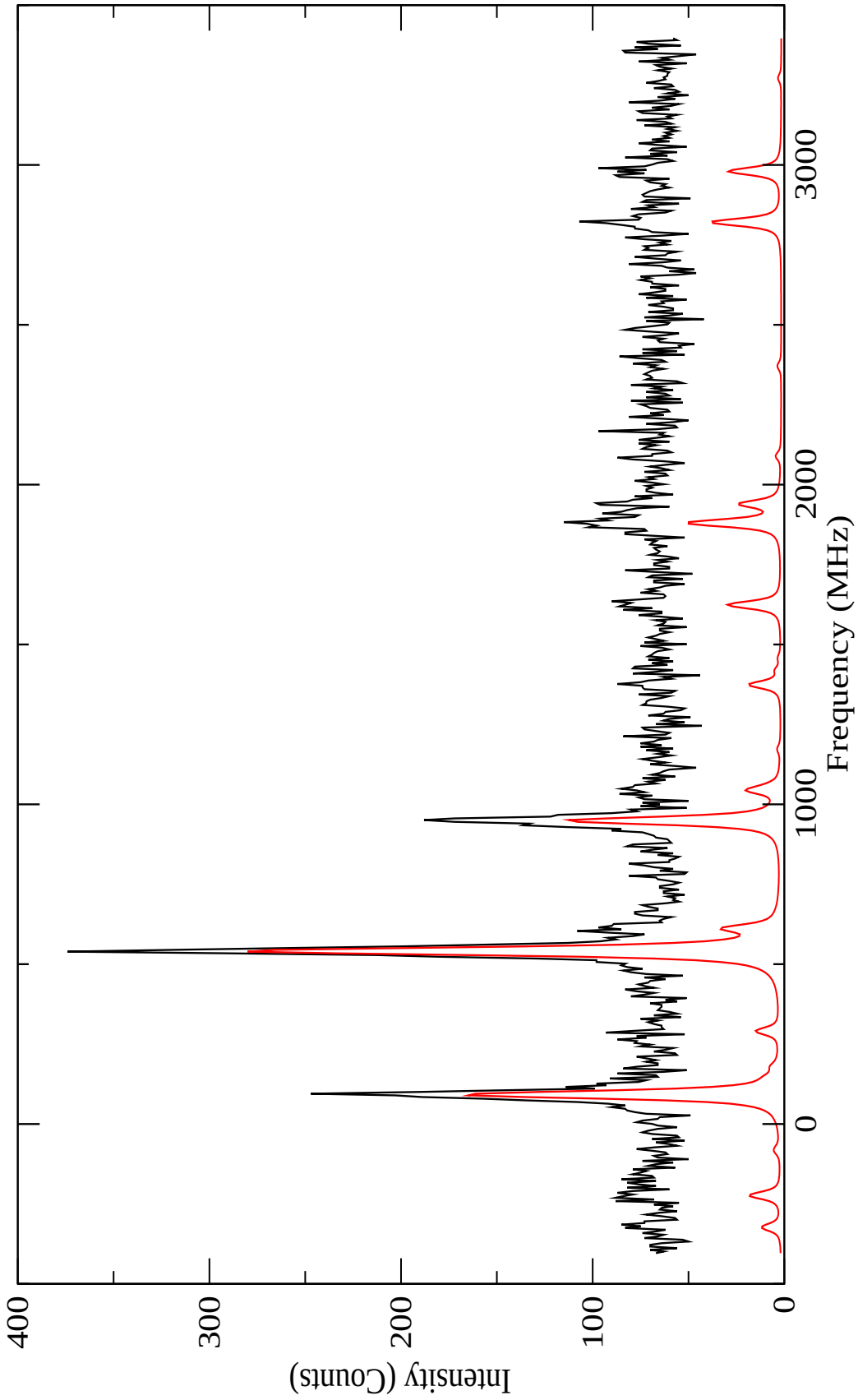

Figure C.17: 330.1594nm transition: 0.000 (J=5) $\rightarrow$ 30279.680cm^{-1} (J=5).

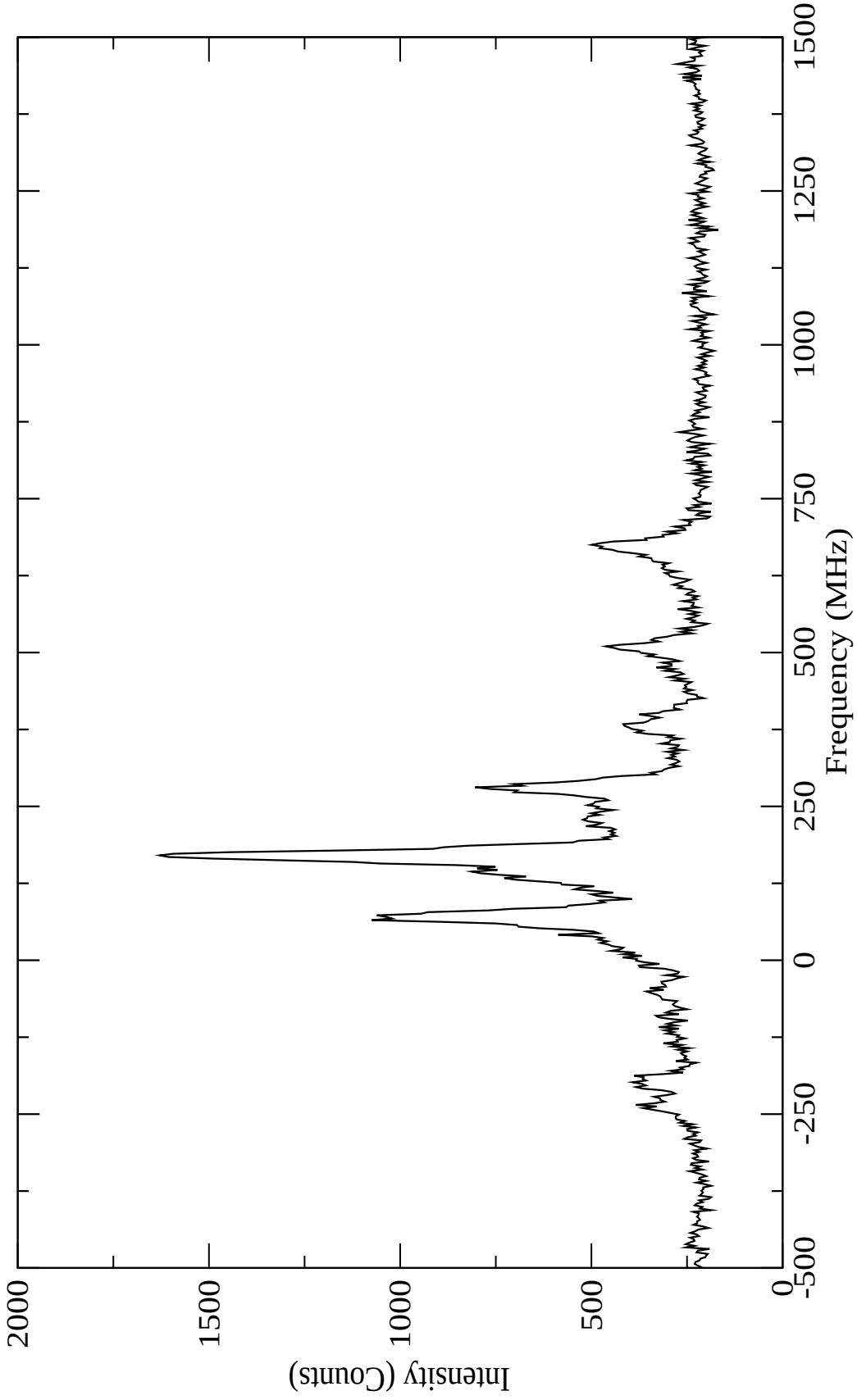

Figure C.18: 342.8318nm transition: 0.000 (J=5) $\rightarrow$ 29160.460cm^{-1} (J=6).

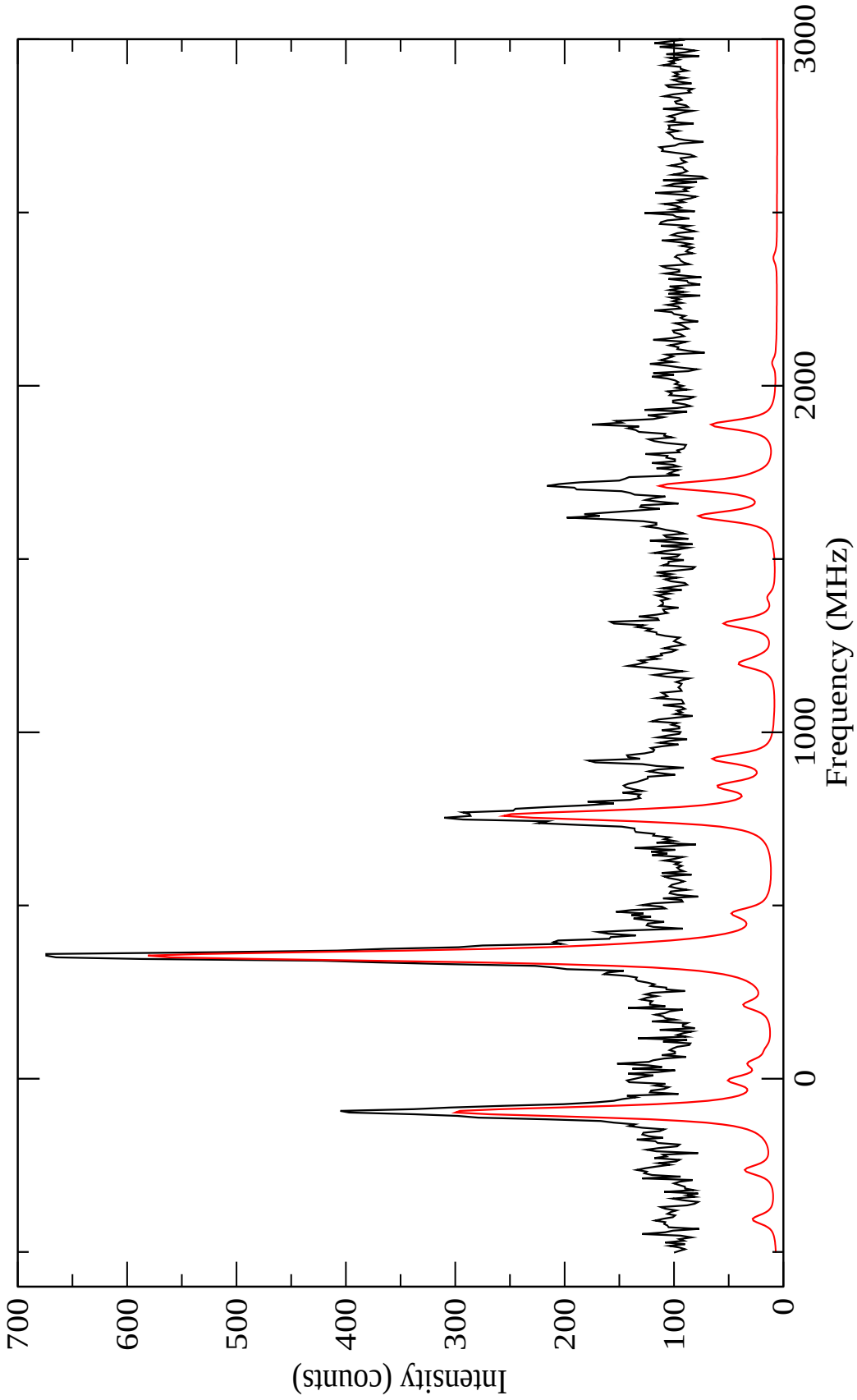

Figure C.19: 343.6736nm transition: 1190.640 (J=4) $\rightarrow$ 30279.680cm^{-1} (J=5).

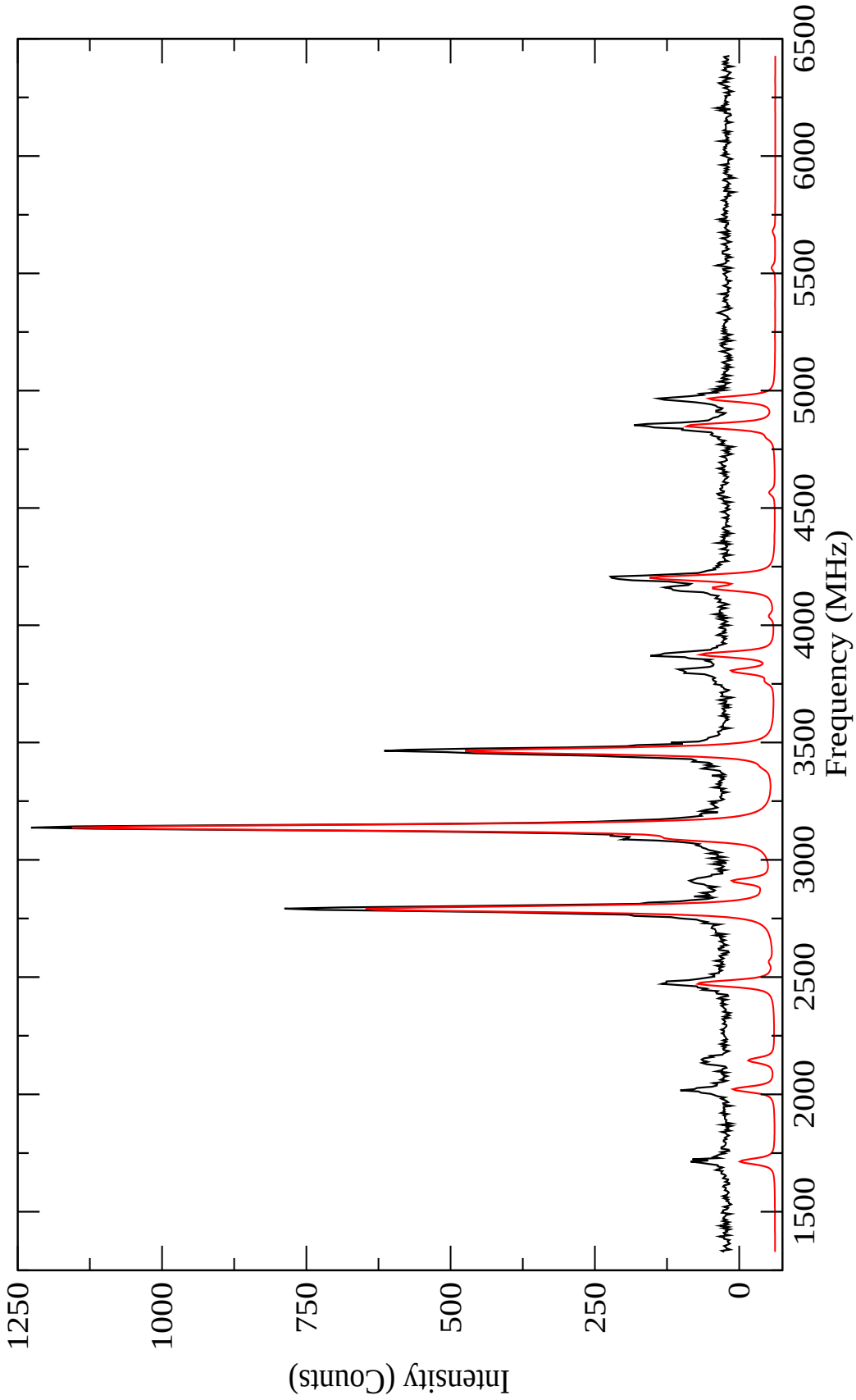

Figure C.20: 349.8942nm transition: 0.000 (J=5) $\rightarrow$ 28571.890cm^{-1} (J=6).

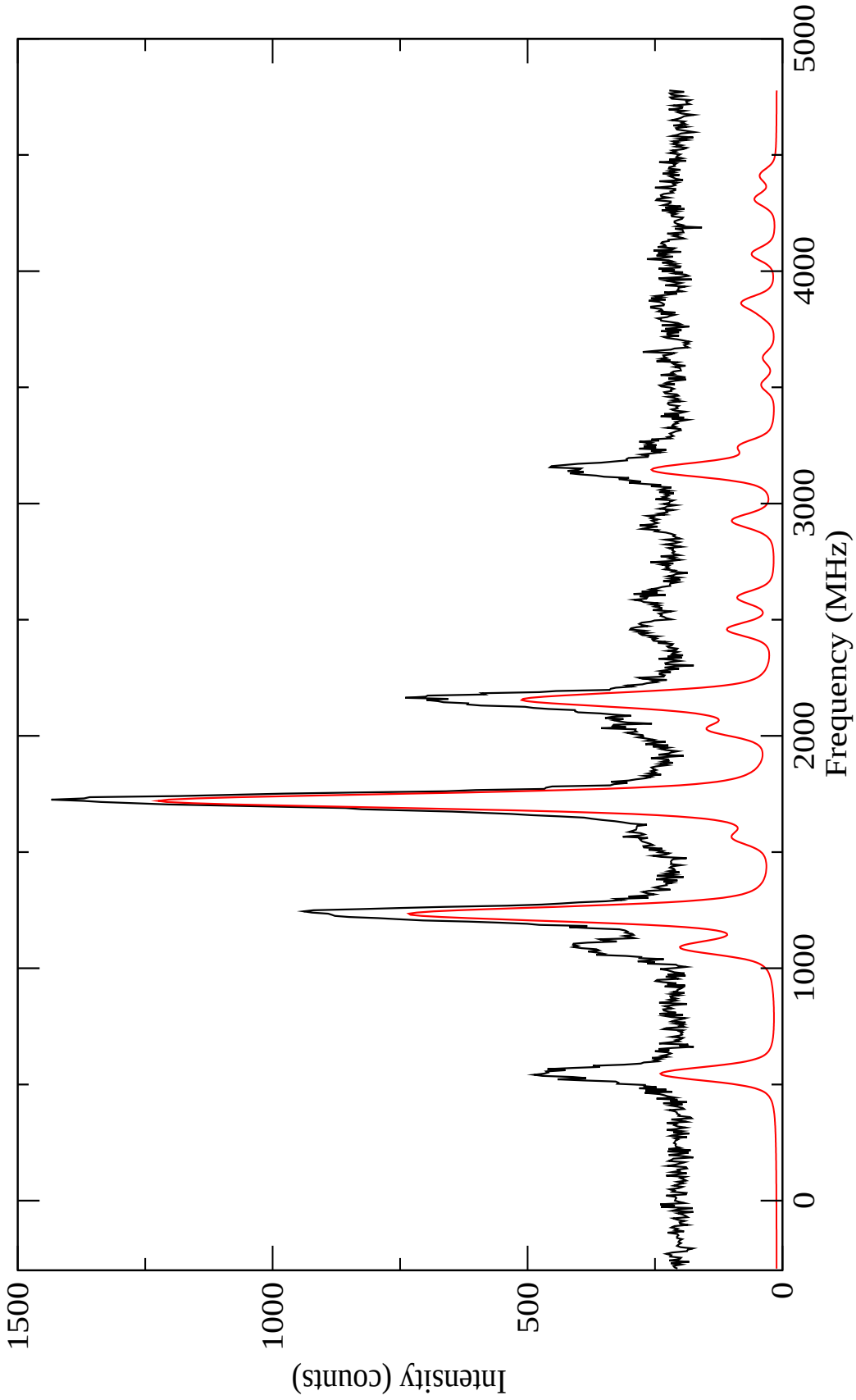

Figure C.21: 358.9213nm transition: 3105.490 (J=1) $\rightarrow$ 30958.800cm^{-1} (J=2).

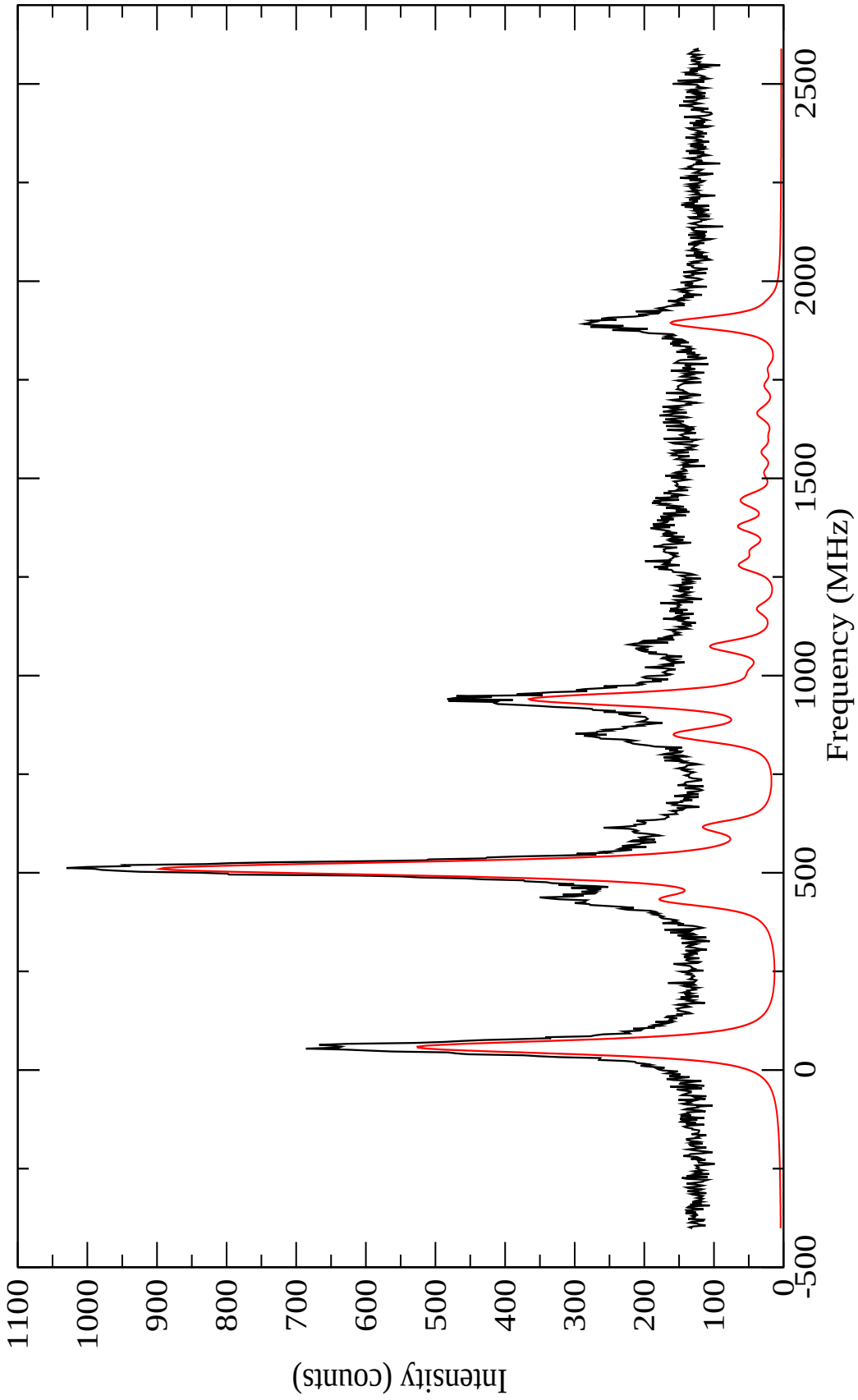

Figure C.22: 359.3018nm transition: 2713.240 (J=2) $\rightarrow$ 30537.060cm^{-1} (J=3).

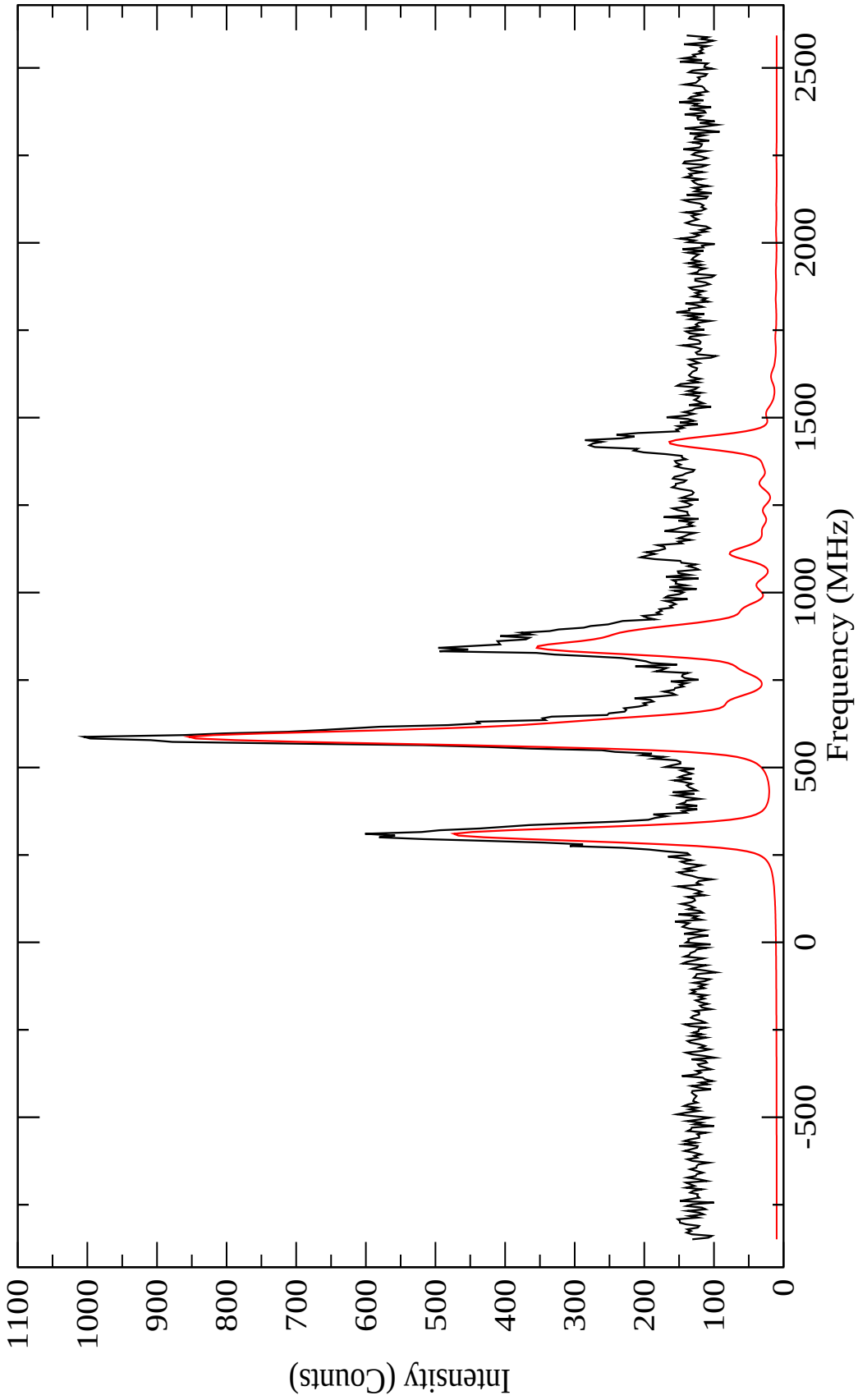

Figure C.23: 359.6178nm transition: 2091.540 (J=3) $\rightarrow$ 29890.910cm^{-1} (J=4).

References

[1] W. H. King, *'Isotope Shifts in Atomic Spectra'*, Plenum Press, New York, (1984).

[2] G. Fricke *et al.*, *At. Data and Nucl. Data Tables* **60**, 177 (1995).

[3] M. Keim *et al.*, *Nucl. Phys. A* **586**, 219 (1995).

[4] C. Thibault *et al.*, *Phys. Rev. C* **23**, 2720 (1981).

[5] F. Burchinger *et al.*, *Phys. Rev. C* **41**, 2883 (1990).

[6] B. Cheal *et al.*, *Phys. Lett. B* **645**, 133 (2007).

[7] H. Thayer *et al.*, *J. Phys. G* **29**, 2247 (2003).

[8] B. Cheal *et al.*, *Phys. Rev. Lett.* **102**, 222501 (2009).

[9] F. C. Charlwood *et al.*, *Phys. Lett. B* **674**, 23 (2009).

[10] W. H. King, *Proc. Roy. Soc. London* **280**, 430 (1964).

[11] J. H. Broadhurst *et al.*, *J. Phys. B: Atom. Molec. Phys.* **7**, L513 (1974).

[12] G. K. Woodgate, *'Elementary Atomic Structure'*, second edition ed., Claredon Press Oxford, (1989).

[13] E. K. Broch, *Arch. Math. Naturvidenskab B* **48**, 25 (1945).

[14] A. R. Bodmer, *Proc. Phys. Soc. A* **66**, 1041 (1953).

[15] E. C. Seltzer, *Phys. Rev.* **188**, 1916 (1969).

[16] K. Krane, *'Introductory Nuclear Physics'*, J Wiley and Sons, (1988).

[17] J. D. Jackson, *'Classical Electrodynamics'*, Wiley; New York, London, (1975).

[18] H. Casimir, *'On the Interaction between Atomic Nuclei and Electrons'*, Freeman, London, (1963).

[19] J. Billowes and P. Campbell, *J. Phys. G: Nucl. Part. Phys* **21**, 707 (1995).

[20] D. H. Forest, Ph.D. Thesis, The University of Birmingham, 1999.

[21] H. Thayer, Ph.D. Thesis, The University of Birmingham, 2003.

[22] E. W. Otten, *'Treatise on Heavy-Ion Science. Nuclei Far From Stability'*, Plenum Press, New York and London, (1988), Vol. 8.

[23] S. Svanberg, *'Atomic and Molecular Spectroscopy'*, third edition ed., Springer, (2001).

[24] W. Demtröder, *'Laser Spectroscopy: Basic Concepts and Instrumentation'*, second edition ed., Springer, (1998).

[25] S. L. Kaufman, *Opt. Commun.* **17**, 309 (1976).

[26] W. H. Wing *et al.*, *Phys. Rev. Lett.* **36**, 1488 (1976).

[27] M. D. Gardener, Ph.D. Thesis, The University of Birmingham, 2006.

[28] U. Brackmann, Lambdachrome Laser Dyes, Data Sheets (1986), lambda Physik GmbH.

[29] E. Cochrane, Ph.D. Thesis, The University of Birmingham, 1996.

[30] S. Gerstenkorn and P. Luc, *'Atlas du Spectre D'Absorption de la Molecule d'Iode'*, Laboratoire Aime-Cotton, Orsay, France, (1980).

[31] A. Corney, *'Atomic and Laser Spectroscopy'*, Claredon Press Oxford, (1977).

[32] Atomic Line Spectral Database, R. L. Kurucz, Univesity of Hannover, http://www.pmp.uni-hannover.de/cgi-bin/ssi/test/kurucz/sekur.html, 2012.

[33] WebElements Ruthenium Database, http://www.webelements.com/ruthenium, 2012.

[34] Xmgrace, http://plasma-gate.weizmann.ac.il/Grace/, 2012.

[35] National Nuclear Data Center (NNDC), Brookhaven National Laboratory, http://www.nndc.bnl.gov, 2012.

[36] S. Büttgenbach *et al.*, *Z. Phys* **269**, 189 (1974).

[37] A. R. Edmonds, *'Angular Momentum in Quantum Mechanics'*, Princeton University Press, (1974).

[38] G. Fricke and K. Heilig, *'Nuclear Charge Radii'*, Springer, (2004).

[39] S. A. Blundell *et al.*, *J. Phys. B: At. Mol. Phys.* **20**, 3663 (1987).

[40] J. H. Pollard, *'A Handbook of Numerical and Statistical Techniques'*, Cambridge University Press, (1977).

[41] J. Äystö, *Nucl. Phys. A* **693**, 477 (2001).

[42] P. Dendooven, *Nucl. Inst. and Meth. in Phys. Res. B* **126**, 182 (1997).

[43] ISOLDE Yield Database, https://oraweb.cern.ch/pls/isolde/query$_tgt, 2012$.

[44] D. H. Forest, *Private Communication*.

[45] K. T. Flanagan *et al.*, *Phys. Rev. Lett* **103**, 142501 (2009).

[46] B. Cheal *et al.*, *Phys. Rev. Lett* **104**, 252502 (2010).

[47] NIST Atomic Spectra Database, http://www.nist.gov/pml/data/asd.cfm, 2012.

[48] F. C. Charlwood *et al.*, *Phys. Lett. B* **690**, 346 (2010).

[49] K. A. Baczynska, Ph.D. Thesis, The University of Birmingham, 2009.

[50] N. J. Stone, *'Table of Nuclear Magnetic Dipole and Electric Quadrupole Moments'*, second edition ed., Claredon Press Oxford, (1998).

[51] R. L. Kurucz, *Phys. Scrip.* 110 (1993).

[52] V. Fivet *et al.*, *Mon. Not. R. Astron. Soc.* **396**, 2124 (2009).